doi.org/10.26434/chemrxiv.12644126.v1

Rapid High Resolution Visible Light 3D Printing

Dowon Ahn, Lynn Stevens, Kevin Zhou, Zachariah Page

Submitted date: 11/07/2020 • Posted date: 13/07/2020

Citation information: Ahn, Dowon; Stevens, Lynn; Zhou, Kevin; Page, Zachariah (2020): Rapid High Resolution Visible Light 3D Printing. ChemRxiv. Preprint. https://doi.org/10.26434/chemrxiv.12644126.v1

Light-driven 3D printing to convert liquid resins into solid objects (i.e., photocuring) has traditionally been dominated by engineering disciplines, yielding the fastest build speeds and highest resolution of any additive manufacturing process. However, the reliance on high energy UV/violet light derived from decades of photolithography research, limits the materials scope due to degradation and attenuation (e.g., absorption and/or scattering). Chemical innovation to shift the spectrum into more mild and tunable visible wavelengths promises to improve compatibility and expand the repertoire of accessible objects, including those containing biological compounds and multi-material structures. Photochemistry at these longer wavelengths currently suffers from slow reaction times precluding its utility. Herein, novel panchromatic photopolymer resins were developed and applied for the first time to realize rapid high resolution visible light 3D printing. The combination of electron deficient iodonium and rich borate co-initiators were critical to overcoming the speed-limited photocuring with visible light. Furthermore, azo-dyes were identified as vital resin components to confine curing to irradiation zones, improving spatial resolution. A unique screening method was used to streamline optimization (e.g., exposure time and azo-dye loading) and correlate resin composition to resolution, cure rate, and mechanical performance. Ultimately, a versatile and general visible light-based printing method was shown to afford 1) stiff and soft objects with feature sizes < 100 µm, 2) build speeds up to 45 mm/h, and 3) mechanical isotropy, rivaling modern UV-based 3D printing technology and providing a foundation from which bio- and composite-printing can emerge.

Rapid High Resolution Visible Light 3D Printing

Dowon Ahn, Lynn M. Stevens, Kevin Zhou, and Zachariah A. Page*

Department of Chemistry, The University of Texas at Austin, 105 East 24th Street, Stop A5300, Austin, Texas 78712, United States.

*email: zpage@utexas.edu

Abstract

Light-driven 3D printing to convert liquid resins into solid objects (i.e., photocuring) has traditionally been dominated by engineering disciplines, yielding the fastest build speeds and highest resolution of any additive manufacturing process. However, the reliance on high energy UV/violet light derived from decades of photolithography research, limits the materials scope due to degradation and attenuation (e.g., absorption and/or scattering). Chemical innovation to shift the spectrum into more mild and tunable visible wavelengths promises to improve compatibility and expand the repertoire of accessible objects, including those containing biological compounds and multi-material structures. Photochemistry at these longer wavelengths currently suffers from slow reaction times precluding its utility. Herein, novel panchromatic photopolymer resins were developed and applied for the first time to realize rapid high resolution visible light 3D printing. The combination of electron deficient iodonium and rich borate co-initiators were critical to overcoming the speed-limited photocuring with visible light. Furthermore, azo-dyes were identified as vital resin components to confine curing to irradiation zones, improving spatial resolution. A unique screening method was used to streamline optimization (e.g., exposure time and azo-dye loading) and correlate resin composition to resolution, cure rate, and mechanical performance. Ultimately, a versatile and general visible light-based printing method was shown to afford 1) stiff and soft objects with feature sizes < 100 μm, 2) build speeds up to 45 mm/h, and 3) mechanical isotropy, rivaling modern UV-based 3D printing technology and providing a foundation from which bio- and composite-printing can emerge.

Introduction

3D printing has revolutionized the way the world creates, influencing nearly every aspect of modern society – from the consumer market to aerospace and medical technologies.[1–4] With the help of computer-aided design, digital objects with customized form factors are realized through successive layering of material (i.e., additive manufacturing). The technology has gained traction in-part by overcoming efficiency issues and intermediary processes, such as milling, carving, and machining, affiliated with conventional manufacturing. To date, engineering feats have dominated the arena of 3D printing, providing a number of elegant methods via extrusion, powder bed fusion, jetting, and light induced polymerization (e.g., stereolithography, SLA, and digital light processing, DLP).[1–4] Among them, SLA and DLP utilize light to transform matter from liquid resins to solid objects (i.e., photocuring).[5–12] DLP in particular has drawn wide attention owing to several attractive features, namely some of the fastest build rates (> 100 mm/h or < 5 s/layer), highest feature resolution (< 100 μm features), wide ink viscosity tolerance (up to ~5,000 cP), small footprint (fits on a standard benchtop), and low cost (starting at ~$300).[2,5,7] However, the demand for faster printing, milder operating conditions, better resolution, and a wider materials scope continues to drive research efforts and provides an opportunity for chemical innovation.

Contemporary photocuring processes in 3D printing are initiated by high energy ultraviolet (UV) light, which provides rapid polymerization and correspondingly short build times (~seconds). As an alternative, visible light offers numerous benefits, including reduced cost and energy of irradiation from readily available and modular light emitting diodes (LEDs), improved biocompatibility and functional group tolerance, greater depth of penetration, and reduced scattering (**Figure 1**).[10,12–16] As such, visible light photocuring has the potential to enable next generation designer material fabrication, including, hydrogels containing live cells,[17] opaque composites,[16] and wavelength-selective multi-material structures[18–23] that promise to advance a range of applications, from structural plastics to tissue engineering and soft robotics.

Nonetheless, the utility of low energy visible LEDs (>420 nm), to the best of our knowledge, has never been demonstrated for SLA- or DLP-based 3D printing. In-part this is due to a lack of commercially available 3D printers with monochromatic visible LEDs, but the grand challenge is to achieve efficient photocuring at these wavelengths to facilitate rapid builds (> 10 mm/h or < 50 s/layer) with high resolution (<

100 μm features) and compete with contemporary UV/violet light based additive manufacturing. To improve visible light photocuring efficiency requires a chemical understanding of how reactive curing agents (e.g., radicals or ions) are generated.

Following absorption of light by a chromophore, photocuring can occur by one of two mechanisms: (i) direct photolysis of a photoinitiator (PI) or (ii) electron/energy transfer from a photosensitizer (PS) to a co-initiator followed by bond scission to generate radicals or ions.[24–28] Although PI compounds often provide rapid photocuring, they rely on a "forbidden" $n \rightarrow \pi^*$ transition, which generally corresponds to weak absorption that is restricted to short wavelengths of light (< 420 nm, violet) – exceptions being titanocenes[10] and acylgermanes[29] that absorb up to ~500 nm (blue/green). In contrast, the use of a PS enables excitation via a $\pi \rightarrow \pi^*$ transition, providing strong absorption that can extend to longer wavelengths (> 500 nm, green to NIR). Leaders in materials photochemistry have demonstrated visible-NIR photocuring of a variety of resins, primarily comprising acrylic and epoxy monomers and crosslinkers.[10,30,31] However, due to the multi-step reaction mechanism (e.g., energy/electron transfer) the cure times are typically slow (> 60 s) and require relatively high irradiation intensities (> 20 mW/cm^2), making them impractical for standard DLP technology.

Herein, rapid visible light driven chemistry using a novel three component system is developed, characterized, and systematically implemented in high resolution 3D printing. Resin optimization was facilitated by real time Fourier transform infrared (RT-FTIR) spectroscopy and photorheology, and printing was

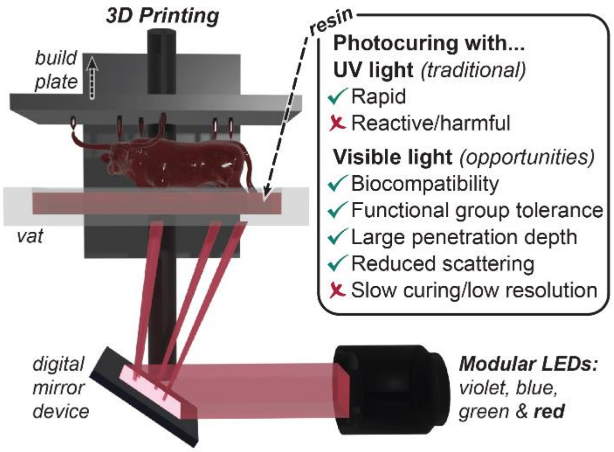

Figure 1. Presented method and opportunities offered by rapid visible light photocuring for 3D printing. Illustration shows the general mechanism for digital light processing (DLP), with exchangeable light emitting diodes (LEDs).

enabled by a DLP system housing visible LEDs (**Figure 1**). Comprehensive studies on photocuring rate, feature resolution, and mechanical properties were conducted to inform future development and utility of the present chemistry in materials synthesis for 3D printing and other emerging areas.

Results and Discussion

To replicate traditional UV-based rapid high resolution DLP 3D printing with low energy visible LEDs necessitated the development of reactive panchromatic resins. These light sensitive polymer resins incorporated monomer, crosslinker, and a PI or PS + co-initiators (i.e., donor, **D**, and/or acceptor, **A**). The monomer, crosslinker, and PI were held constant, while various PS and co-initiator compounds were rationally combined to obtain a mixture that enables photocuring on the order of seconds. Specifically, three component systems (PS + two co-initiators) were examined to both promote PS regeneration and potentially double the concentration of radicals produced per photon absorbed (**Figure 2a**).

Resins comprised dimethyl acrylamide and trimethylolpropane triacrylate as monomer and crosslinker in a 4:1 ratio, respectively. This resin mixture was selected for its good solubilizing characteristics for PS and co-initiator compounds in addition to fast photocuring rate, as demonstrated with a potent PI, bisacylphosphine oxide (BAPO), used here as a violet light (405 nm) control. For reference, BAPO comprised 0.12 mol% (= 0.5 wt% rel. to monomer+crosslinker) of the resin (contents provided as mol% for quantitative analysis and wt% for direct comparison with prior formulation literature)[11].

Rapid photocuring with blue (~460 nm), green (~525 nm), or red (~615 nm) light was accomplished by replacing the violet absorbing PI with a visible absorbing PS and a donor (**D**) and acceptor (**A**) co-initiator. In the present study all resins contain the same electron deficient radical co-initiator (**A**), [4-(octyloxy)phenyl](phenyl)iodonium hexafluoroantimonate diphenyliodonium (0.3 mol% = 2 wt%). To find the optimal partner for **A**, different electron rich co-initiators (**D**) (e.g., amine, silane, and organoborate derivatives) were screened together with various PSs (e.g., camphorquinone, xanthene, cyanine, and porphyrin derivatives). Initial qualitative assessments of visible light curing (e.g., blue, green, or red) were accomplished by irradiating 100 µm thick, argon degassed resins between glass microscope slides using a low intensity light (~5 mW/cm^2) until film formation was noted; for comparison this light source is ~2-20× less intense than an unfocused commercial laser pointer (≈10-100 mW/cm^2). Subsequently, RT-FTIR spectroscopy was used to more closely analyze a subset of samples that showed solidification in $\lesssim$ 60 s (**Table S5** in the SI). The organoborate derivative, 2-(butyryloxy)-*N*,*N*,*N*-trimethylethan-1-aminium butyltriphenylborate[32,33], consistently resulted in the fastest curing rates and was thus used in all subsequent resin formulations (0.04 mol% = 0.2 wt%) (**Figure 2b**). In combination with PS compounds (optimized concentration), H-Nu470 (0.02 mol% = 0.1 wt%), Rose Bengal (0.01 mol% = 0.1 wt%), and zinc tetraphenylporphyrin (ZnTPP, 0.05 mol% = 0.3 wt%), solidification in < 10 s was demonstrated upon exposure to blue, green, and red light irradiation, respectively. For comparison, curing in < 10s was observed for the violet resin, but with 2-10× the concentration of PI (BAPO, 0.12 mol% = 0.5 wt%) relative to each PS (**Figure 2a** inset images). These components serve as the "active" ingredients in all subsequent resins for photocuring.

An additional component often present in lithographic resins is an opaquing agent (OA), which serves as a "passive" absorber (i.e., does not elicit a chemical reaction) to control the optical path length of incident light and, in-turn, improve resolution and homogeneity of curing (particularly in the z-dimension).[34] Ideally OAs (e.g., dyes and pigments) operate by absorbing light in the same wavelength range as the PI or PS within the emission profile of the incident light source. Rapid excited state relaxation is desirable for OAs to preclude electron/energy transfer. Effective OAs in 3D printing reduce the penetration depth of light to mitigate cure through (i.e., curing unwanted regions within previous layers of an object). A series of azo-dyes were selected as OAs given that *cis*/*trans* isomerization and intramolecular proton transfer (when phenol functionality is present *ortho* to the azo group) provide the desired rapid relaxation.[35] Specifically, Sudan I, IV, and black (**Figure 2c**) were chosen for their good absorption overlap with both PI/PS absorption and LED emission profiles (**Figure 2d**).

To correlate the effect of optical attenuation on photocuring parameters, the number of photons absorbed by PI and PS relative to the corresponding OA was determined. This was accomplished by measuring the extinction coefficients for each component using UV-vis absorption spectroscopy (**Figures S5-S11** in the SI) and integrating that with respect to the emission profile for the different LEDs at a particular intensity (see section *'calculating photons absorbed'* in the SI for details). Quantitative LED absorption by PI and PS compounds at their optimized concentrations (*vide supra*) was calculated and compared to

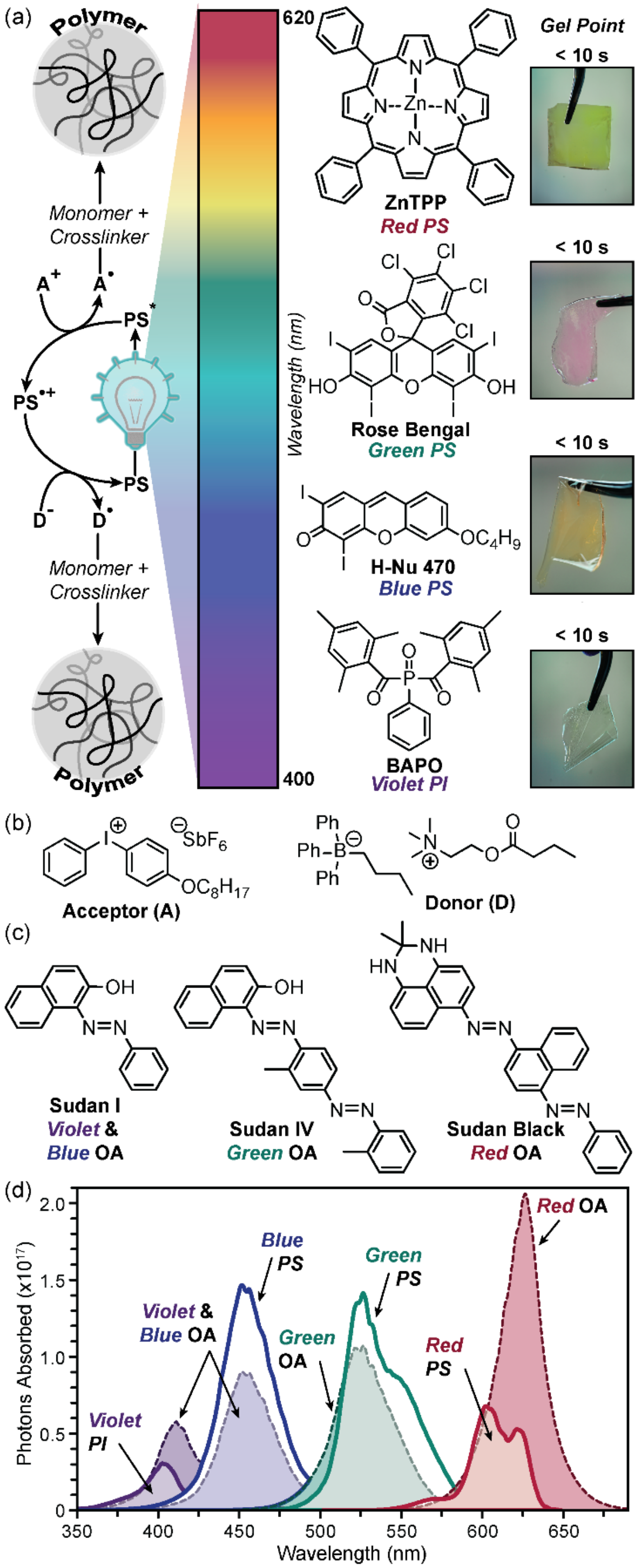

Figure 2. Visible light curing. (a) General mechanism (oxidative quenching) for a three component system (left). Chemical structures of photoinitiator (PI) and photosensitizers (PS), and corresponding pictures of photocured films with qualitative gel times (right). (b) Chemical structures of iodonium acceptor (A) and borate donor (D) co-initiators. (c) Chemical structures of opaquing agents (OAs). (d) Photons absorbed vs wavelength for PI and PS compounds at optimal photocuring concentration, and 0.5 mM (red) and 1 mM (rest) OA. Light exposure is from calibrated violet (405 nm), blue (460 nm), green (525 nm), and red (615 nm) LEDs at the DLP 3D printer image plane.

that for OAs at 0.5 mM (Sudan Black) and 1 mM (rest) (for reference 1mM = 0.01 mol% in the prescribed resin). This analysis revealed the following percent absorption of each LED: (violet) 8% PI and 19% OA, (blue) 53% PS and 33% OA, (green) 57% PS and 43% OA, and (red) 17% PS and 50% OA (see **Table S3** in the SI). Overall, the three OAs and the blue and green PS compounds absorbed significantly more than the violet PI and red PS. The red light absorbing OA was particularly potent, as can be seen in **Figure 2d** where it is the tallest peak at half the concentration relative to the other OAs. Another important note is that the green light absorbing OA had reduced overlap with the corresponding PS at longer LED wavelengths (~570+ nm) (**Figure 2d**), which may result in unwanted cure through. Based on these values, we hypothesized that the resin activated by blue light would need the least amount of OA to prevent cure through and that the red light sensitive resin would be greatly influenced by small fluctuations in [OA]. Notably, while the red PS (ZnTPP) absorbed a fraction of the photons (~3× fewer) relative to the other PS compounds at different wavelengths, it maintained rapid photocuring (< 10s) at low light intensity (~5 mW/cm^2), making it an excellent candidate for 3D printing.

To demonstrate the utility of these novel resins in 3D printing, a custom DLP (**Figure S1** in the SI) with modular visible LEDs (peak emission ≈ 405, 460, 525, 615 nm) was constructed. The minimum volume element (voxel) on the printer has lateral dimensions of 20×20 μm^2 and a vertical dimension of 25 μm (i.e., layer thickness). To examine resolution and mechanical properties of prints in conjunction with curing rates necessitated the use of a 100 μm layer thickness, since RT-FTIR and photorheology monitoring required sample thickness ≥100 μm for adequate signal. Beneficially, the thicker layers facilitate faster builds (*vide infra*). A novel printing method, referred to here as “resolution print”, was developed to efficiently optimize resolution and build speed. Critically, the method provides control over exposure time within different locations of a single layer, which facilitated rapid screening (**Figure 3a**). This printing method was used to correlate exposure time/layer and OA concentration, [OA], to lateral (x,y) and vertical (z) resolution. In this assessment, each resolution print contained a set of squares that were simultaneously printed, varying exposure time/layer. In the bottom half of each square was an array of smaller patterns that were 1 to 16 pixels wide, used to characterize resolution. As shown in **Figure 3b**, a 12 square array was printed (4×4 mm^2 each square) with 4×100 μm layers, and exposure times from 1 to

12 s/layer (time in seconds engraved in each square). For ease of handling, the square array was printed on a rectangular base (12 layers at 12 s/layer). Thus, a single print contained resolution information about 12 exposure times at a particular [OA], streamlining optimization.

Resolution prints were accomplished using violet, blue, green, and red resins with varying amount of the corresponding OA to identify optimal resin composition and exposure time/layer (**Figure 2c**). As the [OA] was increased the first square pattern to appear occurred at longer exposure times, indicating an inverse relationship between build speed and [OA]. This suggests that the OA is effectively competing for photons with that of the PI or PS present (i.e., passive absorption). Even with OA present, patterns were observed within 2 s for all resin formulations, demonstrating the ability to perform rapid visible light curing (**Figure 3b**). Of note, for green and red light sensitive samples a blanket of inert gas (e.g., nitrogen or argon) during the print was necessary to achieve these speeds, while violet and blue light printing was less affected. Under ambient conditions polymerizations are delayed for varying lengths of time (i.e., inhibition period). The delay is attributed to quenching of triplet excited states by oxygen, supported by longer inhibition periods observed for the red light PS (ZnTPP[36]) known to provide high triplet yields.

Concomitant with reduced cure rates upon increasing [OA], was an improved z-resolution as a result of diminished cure through. The z-resolution was characterized by measuring the thickness and angle between the top surface and connecting vertical wall (i.e., sidewall angle, SWA) for each time point on a print using 3D imaging (optical profilometry) (**Figure 3c**). A representative topographical profile for an 11 s/layer square on an optimized red light resolution print (with OA) is shown in **Figure 3a**. Heights and SWA values were determined from an average of 10 positions, using a line measurement tool as depicted in **Figure3c(i)**. Ideal values for the resolution prints reflect the imported digital images, which equated to a height of 400 μm (4 layers at 100 μm/layer) and a SWA of 90°. Without OA the maximum thickness and SWA did not always occur at the same exposure time/layer (**Figures S14-18** in the SI). For example, the red resin without OA had a maximum thickness of 384 μm at 5 s/layer and a SWA of 78° at 4 s/layer (**Figure 3c**, bottom). Additionally, at shorter and longer exposure times both thickness and SWA rapidly decrease, providing a narrow processing window, hindering reproducibility. This is exemplified by setting a tolerance of ±5% for thickness (400 ± 20 μm) and ±17% for SWA (90 ± 15°), which results in a processing window of ~1 s without OA present (exposure time/layer ~5 s). This short processing window was attributed to incomplete curing and cure through prior to- and post-5 s, respectively. Increasing [OA] resulted in a convergence in exposure time for both optimal thickness and SWA, along with a much wider and more well defined processing window (≥ 6s). Consistent with our hypothesis, blue resins did not require any OA to mitigate cure through, which was attributed to the strong absorption by the blue PS.

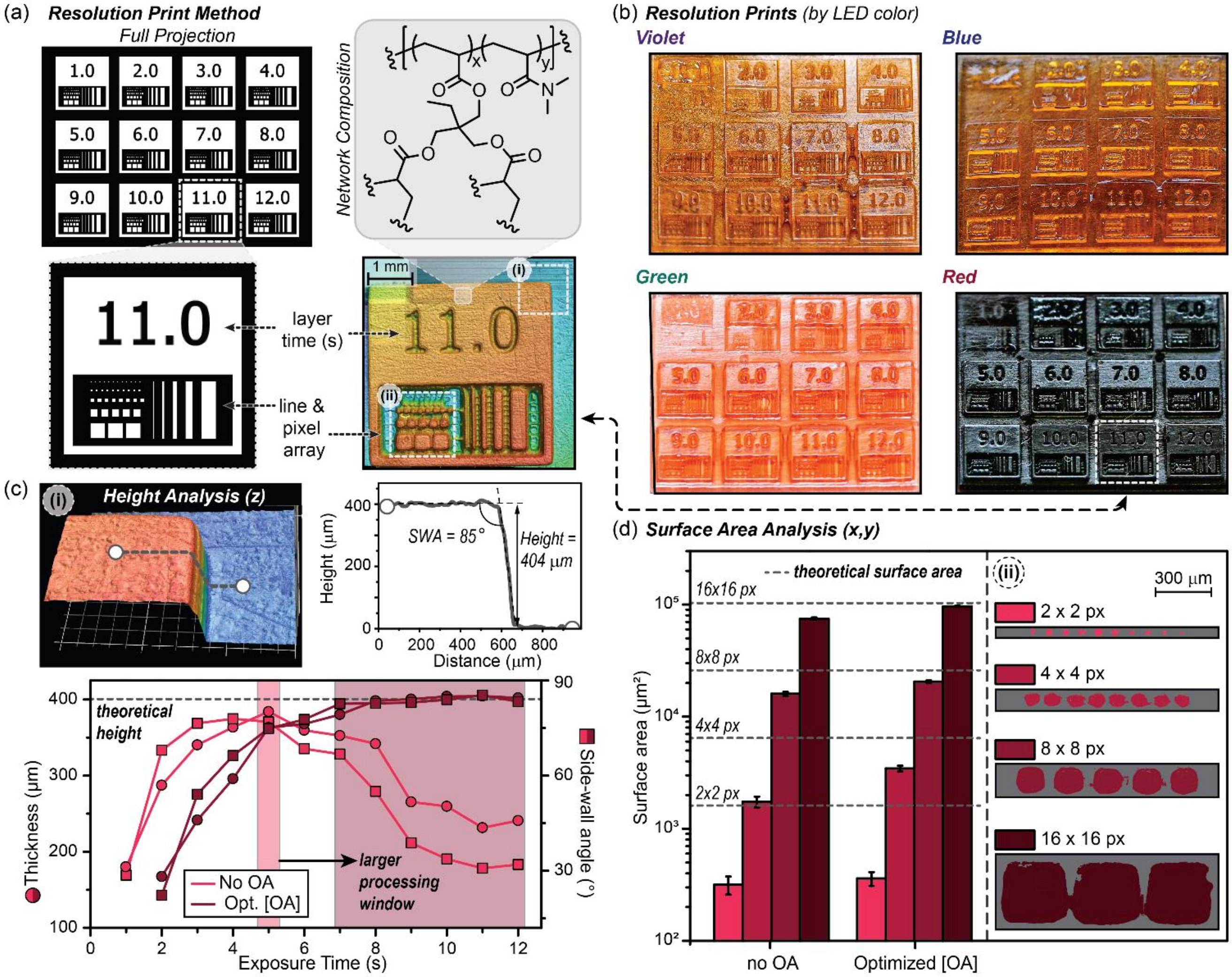

Figure 3. 3D print optimization protocol using the "resolution print" method. (a) Digital projection layer at one second when all squares are illuminated simultaneously (white regions correspond to exposure) (top left). Expanded square for 11 s exposure/layer showing the line and pixel array for the projection (bottom left) and red light resolution print taken with optical profilometry (bottom right). Chemical composition for photocured stiff resin comprising dimethyl acrylamide and trimethylolpropane triacrylate (top right). (b) Optical images of prints from the four resins by exposure color (100 μm layers, 4 layers for each numbered square on top of 12 base layers). (c) z-resolution analysis: 3D image of a corner of the 11 s square outlined as box (i) in the profilometry image above. Height and sidewall angle (SWA) were determined using an average of 10 line traces per corner (with one shown for reference). Graph of thickness and SWA vs exposure time for the red resin printed with and without OA (bottom). Shows how OA improves z-resolution and increases the processing window (theoretical height = 400 μm). (d) x,y-resolution analysis: Plot of surface areas measured for 16, 8, 4, and 2 pixel wide squares using optical profilometry. Dashed lines represent theoretical surface areas, and error bars represent ± 1 standard deviation, showing how OA enhances print fidelity and reproducibility of features below 100 μm in length.

Also in-line with our prior observations was the small amount of OA necessary to mitigate cure through for prints with the green resin (0.003 mol% OA) and, to a greater effect, the red resin (0.0005 mol% OA) (**Table S1** in the SI). At the optimal [OA] for the red resin an average thickness of 405 µm and SWA of 85° was observed across a wide exposure window from 7-12 s/layer (**Figure 3c**). Complete thickness, SWA, and processing window data for all resins are provided in the supporting information (**Figures S14-18**). Optimal exposure times/layer fell between 8 and 11 s for all resins, which corresponds to a build rate of 45 – 33 mm/h (not including the recoating process). Visible light printing was shown to offer wide processing windows to facilitate reproducibility, while providing objects with z-resolution and build speeds that rival contemporary UV-based DLP 3D printers[2].

To assess x,y-resolution, surface areas for the pixel arrays were characterized from the topographical images, as shown in **Figure 3d(ii)**. Specifically, 16, 8, 4, and 2 pixel wide pixel arrays were analyzed by imaging the surfaces for both red (**Figure 3d**) and violet (**Figure S19** in the SI) resolution prints. Samples with and without OA were characterized and compared at optimal exposure times (8 and 4 s/layer for violet with and without OA, and 11 and 5 s/layer for red with and without OA, respectively). Surface area analysis revealed that the presence of OA results in a better match to theoretical, corresponding with larger SWAs (dashed lines in **Figure 3d**). The improved x,y-resolution is hypothesized to result from attenuating light outside of predefined irradiation zones (e.g., scattered light). Additionally, it was noted that deviation of surface area from theoretical values increased as feature size decreased. For red prints with optimized [OA] at an 11 s exposure time/layer the surface area for decreasing features (320×320 to 40×40 µm^2) deviated from theoretical values by 6%, 20%, 46%, and 78%, respectively. The diminished fidelity for smaller features is attributed to incomplete curing. As these polymerizations are exothermic, small features do not generate as much heat as larger features, which can autoaccelerate curing. Irrespective of the feature size, reproducibility was excellent, as evidenced by the small standard deviations in surface area values between same size squares. The present study clearly illustrates that high resolution features (< 100 µm) can be accomplished reproducibly using visible light 3D printing.

The photopolymerization rates and times to gelation were determined to inform future resin development for low energy visible light 3D printing, among other photocuring applications in imaging, lithography, coatings, and adhesives.[9] To this end, RT-FTIR spectroscopy and photorheology were accom plished, carefully matching 3D printing conditions (e.g., thickness, atmosphere, and light intensity) (**Figure 4a**). Specifically, the samples were 100 µm thick, under an inert environment (e.g., degassed with N_2 or argon), and LED exposure intensities matched those of the 3D printer at the resin vat: 3.3, 3.4, 1.8, and 2.1 mW/cm^2 for violet, blue, green, and red, respectively. As a control, data was collected for 10 s in the dark, showing no polymerization prior to light exposure, which demonstrates the efficient temporal nature of these photosystems. The near IR (NIR) absorption region (8,000-4,000 cm^{-1}) was monitored using RT-FTIR to determine monomer/crosslinker conversion by measuring the disappearance of C=C vinylic stretches found at ~6,160 cm^{-1}.[37] The inherently weak absorption signals in the NIR (e.g., overtones of mid IR signals) required that samples were ~100 µm thick, but enabled the utility of disposable glass slides for facile preparation and measurement (note: glass is NIR transparent, but mid IR opaque).

Under the optimized printing conditions each resin rapidly polymerized, reaching a maximum monomer conversion within 20 s of turning the light on (**Figure 4b**). Notably, the C=C conversion peaks at ~80%, which is likely due to a reduction in molecular motion post-gelation. Moreover, under ambient conditions a distinct induction period was observed after turning the light on, consistent with the slower printing speed noted previously. Specifically, inhibition times of 2, 5, 8, and 83 s was observed for violet, blue, green, and red respectively (**Table S6** and **Figures S22** in the SI), confirming the distinct sensitivity of the red PS (ZnTPP) to oxygen. However, a similar maximum polymerization rate is reached once oxygen is consumed. The similar rate is attributed to either efficient regeneration of the PS in the tricomponent photosystem (**Figure 2a**) and/or a rate limiting step other than electron/energy transfer, such that removing a fraction of PS upon reaction with oxygen does not alter the apparent rate. These findings reinforces that oxygen removal as an effective strategy to increase photocuring rate and accordingly print speeds.

In addition to increasing photopolymerization rate by oxygen removal, the effect of light intensity was examined as a complementary route to further improve curing rate and associated build speeds. At the optimized printing conditions the maximum apparent polymerization rates were 1.33 ± 0.05 M/s, 1.16 ± 0.05 M/s, 1.09 ± 0.09 M/s, and 1.9 ± 0.3 M/s, for violet, blue, green, and red respectively. Increasing the light intensity to 10 mW/cm^2 resulted in a ~1.6-2× polymerization rate enhancement relative to those obtained at the printer intensities (**Table S7** and **Figures S26-S33** in the SI).

Photorheology was used to determine gel times and corresponding double bond conversion at the gel point to inform future resin development. Gelation was identified as the crossover between storage and loss modulus, which occurred within 2 to 4 seconds of light exposure. This short gel time is consistent with the first appearance of features on the resolution prints (**Figure 3b**). Specifically, gel points were 1.8 ± 0.2 s, 1.9 ± 0.1 s, 3.4 ± 0.2 s, and 4.2 ± 0.2 s for violet, blue, green, and red respectively (**Figures S34-S37** and **Table S8** in the SI). The measured double conversions at the gel points fell within a similar range for all resins (~5-8 %), which is expected given the constant monomer and cross-linker composition in each resin (**Figure 4b**, semi-transparent grey bar). The C=C conversion for each resin at the optimized 3D printing exposure time/layer (~8-11 s) occurred at ~50-70%, which falls below the maximum conversion (~80%). Therefore, polymerizable vinylic residues should be present at the interface of each layer

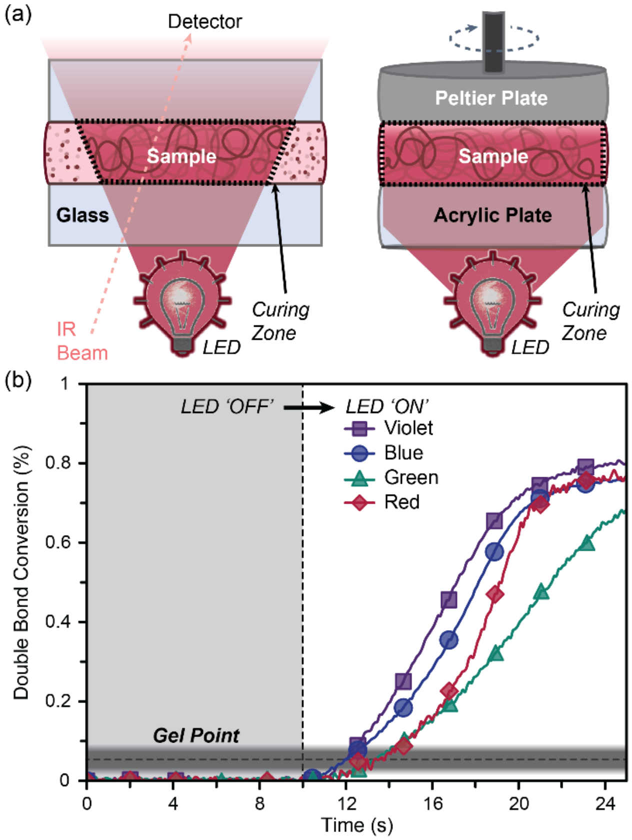

Figure 4. Photopolymerization rate and gel point characterization. (a) Schematic representations of the RT-FTIR and photorheology setups. (b) Plot of double bond conversion vs time for violet, blue, green, and red photopolymerizations. Experiments were performed under an inert atmosphere at an exposure intensity matching the 3D printer. Light exposure began at 10 s, highlighting the rapid temporal response. The gradient bar represents the gel point range found for all four samples (~5-8% conversion), which was determined using a combination of photorheology and RT-FTIR.

during the 3D printing process, which can facilitate covalent bonding and increase mechanical strength.

To push the boundaries of additive manufacturing from traditional hobbyist printing and models to applications that require both precision and structural integrity necessitated a thorough understanding of mechanical performance. To this end, dogbones (ASTM D638) from each resin formulation were 3D printed under optimized conditions and subjected to tensile testing (**Figure 5**). Mechanical properties of interest included stiffness ($\boldsymbol{E}$, Young's modulus), yield strength ($\boldsymbol{\sigma_y}$), and strain at fracture ($\boldsymbol{\varepsilon_f}$). Following standard protocols, all objects were post-cured with UV light prior to tensile testing (20 min., centered at ~370 nm). As a control, post-curing red light printed dogbones with red light in place of UV light provided nearly identical mechanical performance (**Figure S38** in the SI). Excitingly, $\boldsymbol{E}$, $\boldsymbol{\sigma_y}$, $\boldsymbol{\varepsilon_f}$ were consistent for all resins, suggesting that the presence of a tricomponent photoactive system does not alter mechanical performance: $\boldsymbol{E}$ = 997 ± 62 MPa (violet), 1022 ± 63 MPa (blue), 986 ± 102 MPa (green), and 1043 ± 94 MPa (red) (**Figure 5a** and **Table S9**).

Mechanical uniformity of visible light printed objects was examined, as layered production is often challenged with an undesirable anisotropic mechanical response with weakness at the boundaries between adjacent layers.[39–41] To this end, dogbones from the optimized red resin were printed at three different edge-on angles – horizontal (0°), vertical (90°), and diagonal (45°) (**Figure 5b**). Optical profilometry images of the dogbones printed at different angles clearly show the layers and demonstrates excellent thickness accuracy (102 ± 1 μm/layer, 100 ± 2 μm/layer, 99 ± 2 μm/layer for horizonal, vertical, and diagonal angles, respectively) (**Figure 5b** inset). Compellingly, $\boldsymbol{E}$ values were unperturbed by changing print angle (average $\boldsymbol{E}$ = 1083 ± 47 MPa), and only small fluctuations in $\boldsymbol{\sigma_y}$ and $\boldsymbol{\varepsilon_f}$ were observed: $\boldsymbol{\sigma_y}$ = 31 ± 2 MPa, 31 ± 2 MPa, and 29 ± 2 MPa for horizontal, diagonal, and vertical angles, respectively (**Figure 5b** and **Table S10** in the SI). These minor differences are in accord with other objects printed via UV-based vat photopolymerization.[39–41]

To demonstrate the versatility of visible light 3D printing, mechanically and chemically disparate objects were prepared (e.g., stiff vs soft and hydrophobic vs hydrophilic). The previous resin provided a stiff and brittle object, which was attributed to the high glass transition temperature for poly(dimethyl acrylamide) ($T_g \approx 90$ °C) in conjugation with a large amount of crosslinker (i.e., 20 wt% triacrylate rel. to monomer).

3D printing soft and extensible objects remains an active area of research due to the challenges that arise from their natural tendency to deform during prints.[42–44] A resin comprising 2-hydroxyethyl acrylate monomer with a correspondingly low polymer T_g (≈ -15 °C) and a small amount of crosslinker, tetra(ethylene glycol) diacrylate (0.1 wt% rel. to monomer), was formulated to provide a softer and more extensible

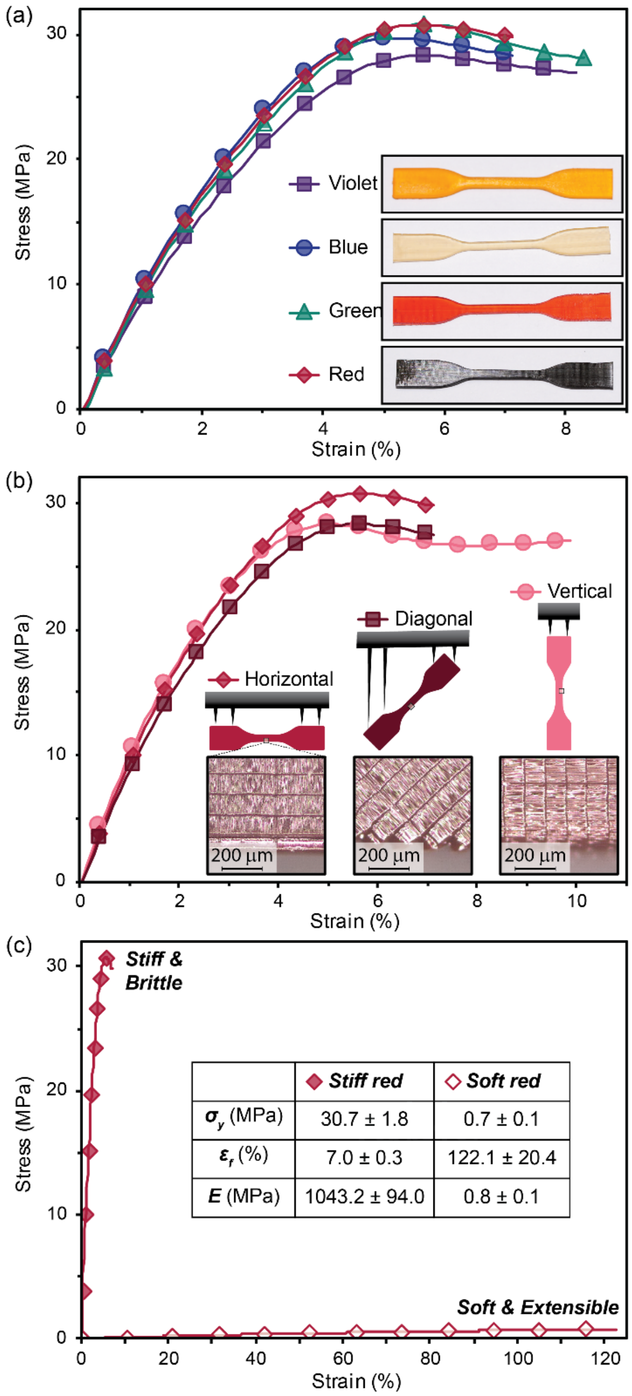

	◆ Stiff red	◇ Soft red
σ_y (MPa)	30.7 ± 1.8	0.7 ± 0.1
ε_r (%)	7.0 ± 0.3	122.1 ± 20.4
E (MPa)	1043.2 ± 94.0	0.8 ± 0.1

Figure 5. Mechanical testing of 3D printed dogbones (a) Stress-strain curves of violet, blue, green, and red dogbones (b) Red dogbones printed at three different edge-on angles (horizontal, diagonal, and vertical). Insets show a drawing of each dogbone orientation, with supports to the build platform shown, and close up images to visualize each layer angle. (c) Stress-strain curves of stiff and elastic red resin. Inset shows a table highlighting the disparate mechanical properties.

material. With the optimized red light photosystem, dogbones were 3D printed with the new soft resin formulation. Tensile testing revealed a ***E*** = 0.8 ± 0.1 MPa, which is three orders of magnitude lower than those from the stiff resin (**Figure 5c**). Moreover, swelling tests in water for six cubes printed with either stiff or soft resin qualitatively highlight the difference in chemical makeup (**Figure S40**). The soft cubes had a much larger water uptake (177 ± 1% increase in weight) compared to the stiff resin (54 ± 2% increase in weight), which is attributed to a combination of lower crosslink density and increased hydrophilicity of the alcohol-laden soft network (**Table S13** in the SI). The contrasting mechanical and chemical properties of objects printed with the same visible light photosystem demonstrates the versatility of the present method, which will provide access to a myriad of materials without the need for harmful UV light.

As a final demonstration, an octet truss was printed to show how visible light additive manufacturing can be used to rapidly provide high resolution complex (e.g., hierarchical) 3D objects that are challenging or impossible to produce using traditional manufacturing processes. The octet truss was printed with the original stiff red resin using both 100 μm (**Figure S41**) and 25 μm layer thickness (**Figure 6**). Decreasing the layer thickness facilitated reduced exposure times/layer, from 11 s at 100 μm layers to 8 s at 25 μm layers, correlating to a build rate of ~7 mm/h. Scanning electron microscopy (SEM) images shows the high printing fidelity along with individual layers at a pitch of 25.1 ± 0.6 μm. Interestingly, the final object was also red emissive under a handheld 365 nm UV light (**Figure S42** in the SI), which demonstrates

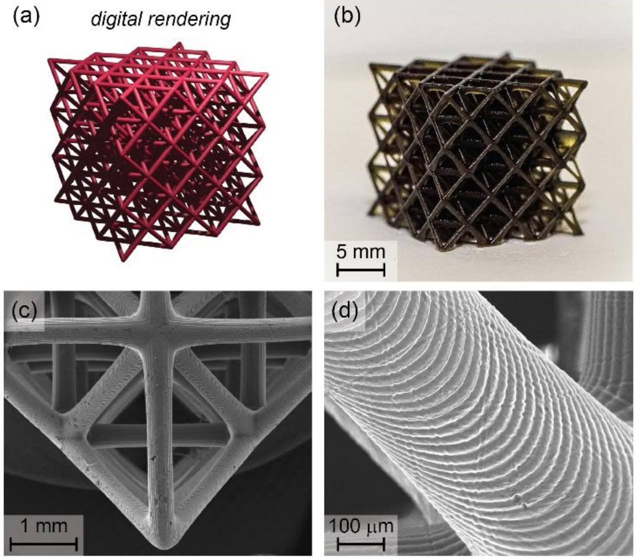

Figure 6. Hierarchical octet truss as a complex 3D print demonstration. (a) Digital rendering. (b) Photograph of the printed object using the stiff red resin composition and red light exposure (~2.1 mW/cm2) for 8 s/25 μm layer. (c,d) Scanning electron microscope images at different magnification showing the structural hierarchy.

that a certain amount of embedded PS (ZnTPP) remains intact, providing an avenue towards functional 3D prints (i.e., “smart” plastics). Additional 3D prints can be found in the supporting information file (**Figure S43** in the SI). These sophisticated structures with custom form factors emphasize the utility of visible light 3D printing to seamlessly reproduce complex digital inputs with excellent feature fidelity.

Concluding Remarks

Novel photopolymer resins that rapidly react upon irradiation with visible light across the spectrum were described and systematically examined for use in high resolution DLP 3D printing. Key discoveries and developments include rapid photocuring from combined iodonium (donor) and borate (acceptor) co-initiators, resolution enhancements from visible light absorbing azo-dyes (OA), and efficient optimization using a custom “resolution print” method. A DLP 3D printer with exchangeable LEDs provided rapid build speeds from 33 to 45 mm/h for low intensity violet, blue, green, and red light exposure (~2-3 mW/cm^2). RT-FTIR and photorheology were used to judiciously correlate chemical composition of resins to photocuring rate, x,y,z-resolution, build speed, and mechanical properties. Inclusion of OA compounds into the resin formulation was shown to enhance resolution, with features < 100 μm in the lateral dimension and 25 μm layer thickness, while simultaneously enhancing reproducibility by widening the processing window prior to cure through from ~1 to ≥ 6 s. Mechanical properties were shown to be nearly independent of curing wavelength and the print orientation, demonstrating the production of relatively isotropic parts. Versatility was highlighted by rapidly producing both stiff and soft objects with stiffness ranging from ~1480 to 0.8 MPa. Finally, objects with intricate form factors were printed as a testament to the 3D capabilities offered by the present technique. As a future endeavor, increasing light intensity (up to ~10 mW/cm^2) provides an avenue towards even faster visible light based 3D printing (~1.5-2×). The foundational studies provided herein will serve as a roadmap for further development of visible and NIR photocuring with excellent spatial control, material compatibility, and utility that extends beyond 3D printing (e.g., coatings, adhesives, imaging, and lithography). As a result, we envision numerous exciting and transformative interdisciplinary research opportunities in academic, industrial, and medical sectors, including hierarchical multimaterial fabrication, fiber reinforced composites, and cell-laden hydrogels.

Conflicts of interest

There are no conflicts to declare.

Acknowledgements

We thank the ARO STIR program of the Department of Defense (W911NF1910310) and Robert A. Welch Foundation (F-2007) for financial support. The authors acknowledge the use of shared research facilities supported in part by the Texas Materials Institute, the Center for Dynamics and Control of Materials: an NSF MRSEC (DMR-1720595), and the NSF National Nanotechnology Coordinated Infrastructure (ECCS-1542159). We thank Dr. Yun-Ho Jang at MonoPrinter for the custom DLP 3D printer and software design.

Abbreviations

SLA, Stereolithography; DLP, Digital light processing; UV, ultraviolet; LED, light emitting diode; PI, photoinitiator; PS, photosensitizer; RT-FTIR, real time Fourier transform infrared; OA, opaquing agent; ASTM, American Society for Testing and Materials

References

(1) Narupai, B.; Nelson, A. 100th Anniversary of Macromolecular Science Viewpoint: Macromolecular Materials for Additive Manufacturing. *ACS Macro Lett.* **2020**, 627–638.

(2) Wallin, T. J.; Pikul, J.; Shepherd, R. F. 3D Printing of Soft Robotic Systems. *Nat. Rev. Mater.* **2018**, *3* (6), 84–100.

(3) Ligon, S. C.; Liska, R.; Stampfl, J.; Gurr, M.; Mülhaupt, R. Polymers for 3D Printing and Customized Additive Manufacturing. *Chem. Rev.* **2017**, *117* (15), 10212–10290.

(4) Truby, R. L.; Lewis, J. A. Printing Soft Matter in Three Dimensions. *Nature* **2016**, *540* (7633), 371–378.

(5) Tumbleston, J. R.; Shirvanyants, D.; Ermoshkin, N.; Janusziewicz, R.; Johnson, A. R.; Kelly, D.; Chen, K.; Pinschmidt, R.; Rolland, J. P.; Ermoshkin, A.; et al. Continuous Liquid Interface Production of 3D Objects. *Science.* **2015**, *347* (6228), 1349–1352.

(6) Kelly, B. E.; Bhattacharya, I.; Heidari, H.; Shusteff, M.; Spadaccini, C. M.; Taylor, H. K. Volumetric Additive Manufacturing via Tomographic Reconstruction. *Science.* **2019**, *363* (6431), 1075–1079.

(7) Walker, D. A.; Hedrick, J. L.; Mirkin, C. A. Rapid, Large-Volume, Thermally Controlled 3D Printing Using a Mobile Liquid Interface. *Science.* **2019**, *366* (6463), 360–364.

(8) Jung, K.; Corrigan, N.; Ciftci, M.; Xu, J.; Seo, S. E.; Hawker, C. J.; Boyer, C. Designing with Light: Advanced 2D, 3D, and 4D Materials. *Adv. Mater.* **2019**, 1903850.

(9) del Barrio, J.; Sánchez-Somolinos, C. Light to Shape the Future: From Photolithography to 4D Printing. *Adv. Opt. Mater.* **2019**, *7* (16), 1900598.

(10) Bagheri, A.; Jin, J. Photopolymerization in 3D Printing. *ACS Appl. Polym. Mater.* **2019**, *1* (4), 593–611.

(11) Zhang, J.; Xiao, P. 3D Printing of Photopolymers. *Polym. Chem.* **2018**, *9* (13), 1530–1540.

(12) Chatani, S.; Kloxin, C. J.; Bowman, C. N. The Power of Light in Polymer Science: Photochemical Processes to Manipulate Polymer Formation, Structure, and Properties. *Polym. Chem.* **2014**, *5* (7), 2187–2201.

(13) Xiao, P.; Zhang, J.; Dumur, F.; Tehfe, M. A.; Morlet-Savary, F.; Graff, B.; Gigmes, D.; Fouassier, J. P.; Lalevée, J. Visible Light Sensitive Photoinitiating Systems: Recent Progress in Cationic and Radical Photopolymerization Reactions under Soft Conditions. *Prog. Polym. Sci.* **2015**, *41* (C), 32–66.

(14) Bagheri, A.; Bainbridge, C.; Jin, J. Visible Light-Induced Transformation of Polymer Networks. *ACS Appl. Polym. Mater.* **2019**, *1* (7), 1896–1904.

(15) Dumur, F. Recent Advances on Visible Light Metal-Based Photocatalysts for Polymerization under Low Light Intensity. *Catalysts* **2019**, *9* (9), 736.

(16) Strehmel, B.; Schmitz, C.; Cremanns, K.; Göttert, J. Photochemistry with Cyanines in the Near Infrared: A Step to Chemistry 4.0 Technologies. *Chem. - A Eur. J.* **2019**, *25* (56), 12855–12864.

(17) Lim, K. S.; Galarraga, J. H.; Cui, X.; Lindberg, G. C. J.; Burdick, J. A.; Woodfield, T. B. F. Fundamentals and Applications of Photo-Cross-Linking in Bioprinting. *Chem. Rev.* **2020**, acs.chemrev.9b00812.

(18) Schwartz, J. J.; Boydston, A. J. Multimaterial Actinic Spatial Control 3D and 4D Printing. *Nat. Commun.* **2019**, *10* (1), 791.

(19) Bialas, S.; Michalek, L.; Marschner, D. E.; Krappitz, T.; Wegener, M.; Blinco, J.; Blasco, E.; Frisch, H.; Barner-Kowollik, C. Access to Disparate Soft Matter Materials by Curing with Two Colors of Light. *Adv. Mater.* **2019**, *31* (8), 1807288.

(20) Dolinski, N. D.; Page, Z. A.; Callaway, E. B.; Eisenreich, F.; Garcia, R. V.; Chavez, R.; Bothman, D. P.; Hecht, S.; Zok, F. W.; Hawker, C. J. Solution Mask Liquid Lithography (SMaLL) for One-Step, Multimaterial 3D Printing. *Adv. Mater.* **2018**, *30* (31), 1800364.

(21) Zhang, X.; Xi, W.; Huang, S.; Long, K.; Bowman, C. N. Wavelength-Selective Sequential Polymer Network Formation Controlled with a Two-Color Responsive Initiation System. *Macromolecules* **2017**, *50* (15), 5652–5660.

(22) Kottisch, V.; Michaudel, Q.; Fors, B. P. Photocontrolled Interconversion of Cationic and Radical Polymerizations. *J. Am. Chem. Soc.* **2017**, *139* (31), 10665–10668.

(23) Peterson, B. M.; Kottisch, V.; Supej, M. J.; Fors, B. P. On Demand Switching of Polymerization Mechanism and Monomer Selectivity with Orthogonal Stimuli. *ACS Cent. Sci.* **2018**, *4* (9), 1228–1234.

(24) Garra, P.; Dietlin, C.; Morlet-Savary, F.; Dumur, F.; Gigmes, D.; Fouassier, J. P.; Lalevée, J. Redox Two-Component Initiated Free Radical and Cationic Polymerizations: Concepts, Reactions and Applications. *Prog. Polym. Sci.* **2019**, *94*, 33–56.

(25) Blasco, E.; Wegener, M.; Barner-Kowollik, C. Photochemically Driven Polymeric Network Formation: Synthesis and Applications. *Adv. Mater.* **2017**, *29* (15), 1604005.

(26) Matsui, J. K.; Lang, S. B.; Heitz, D. R.; Molander, G. A. Photoredox-Mediated Routes to Radicals: The Value of Catalytic Radical Generation in Synthetic Methods Development. *ACS Catal.* **2017**, *7* (4), 2563–2575.

(27) Dadashi-Silab, S.; Doran, S.; Yagci, Y. Photoinduced Electron Transfer Reactions for Macromolecular Syntheses. *Chem. Rev.* **2016**, *116* (17), 10212–10275.

(28) Chen, M.; Zhong, M.; Johnson, J. A. Light-Controlled Radical Polymerization: Mechanisms, Methods, and Applications. *Chem. Rev.* **2016**, *116* (17), 10167–10211.

(29) Haas, M.; Radebner, J.; Eibel, A.; Gescheidt, G.; Stueger, H. Recent Advances in Germanium-Based Photoinitiator Chemistry. *Chem. - A Eur. J.* **2018**, *24* (33), 8258–8267.

(30) Bagheri, A.; Bainbridge, C. W. A.; Engel, K. E.; Qiao, G. G.; Xu, J.; Boyer, C.; Jin, J. Oxygen Tolerant PET-RAFT Facilitated 3D Printing of Polymeric Materials under Visible LEDs. *ACS Appl. Polym. Mater.* **2020**, *2* (2), 782–790.

(31) Zhang, Z.; Corrigan, N.; Bagheri, A.; Jin, J.; Boyer, C. A Versatile 3D and 4D Printing System through Photocontrolled RAFT Polymerization. *Angew. Chemie - Int. Ed.* **2019**, *58* (50), 17954–17963.

(32) Polykarpov, A. Y.; Neckers, D. C. Tetramethylammonium Phenyltrialkylborates in the Photoinduced Electron Transfer Reaction with Benzophenone. Generation of Alkyl Radicals and Their Addition to Activated Alkenes. *Tetrahedron Lett.* **1995**, *36* (31), 5483–5486.

(33) Kabatc, J.; Jędrzejewska, B.; Pączkowski, J. Hemicyanine N-Butyltriphenylborate Salts as Effective Initiators of Free-Radical Polymerization Photoinitiated via Photoinduced Electron-Transfer Process. *J. Polym. Sci. Part A Polym. Chem.* **2003**, *41* (19), 3017–3026.

(34) Pritchard, Z. D.; Beer, M. P.; Whelan, R. J.; Scott, T. F.; Burns, M. A. Modeling and Correcting Cure-Through in Continuous Stereolithographic 3D Printing. *Adv. Mater. Technol.* **2019**, 1900700.

(35) Cui, G.; Guan, P. J.; Fang, W. H. Photoinduced Proton Transfer and Isomerization in a Hydrogen-Bonded Aromatic Azo Compound: A CASPT2//CASSCF Study. *J. Phys. Chem. A* **2014**, *118* (26), 4732–4739.

(36) Shanmugam, S.; Xu, J.; Boyer, C. Exploiting Metalloporphyrins for Selective Living Radical Polymerization Tunable over Visible Wavelengths. *J. Am. Chem. Soc.* **2015**, *137* (28), 9174–9185.

(37) Park, H. Y.; Kloxin, C. J.; Fordney, M. F.; Bowman, C. N. Stress Relaxation of Trithiocarbonate-Dimethacrylate-Based Dental Composites. *Dent. Mater.* **2012**, *28* (8), 888–893.

(38) Ligon, S. C.; Husár, B.; Wutzel, H.; Holman, R.; Liska, R. Strategies to Reduce Oxygen Inhibition in Photoinduced Polymerization. *Chem. Rev.* **2014**, *114* (1), 577–589.

(39) Monzón, M.; Ortega, Z.; Hernández, A.; Paz, R.; Ortega, F. Anisotropy of Photopolymer Parts Made by Digital Light Processing. *Materials (Basel).* **2017**, *10* (1), 64.

(40) Dizon, J. R. C.; Espera, A. H.; Chen, Q.; Advincula, R. C. Mechanical Characterization of 3D-Printed Polymers. *Addit. Manuf.* **2018**, *20*, 44–67.

(41) Anastasio, R.; Peerbooms, W.; Cardinaels, R.; Van Breemen, L. C. A. Characterization of Ultraviolet-Cured Methacrylate Networks: From Photopolymerization to Ultimate Mechanical Properties. *Macromolecules* **2019**, *52* (23), 9220–9231.

(42) Patel, D. K.; Sakhaei, A. H.; Layani, M.; Zhang, B.; Ge, Q.; Magdassi, S. Highly Stretchable and UV Curable Elastomers for Digital Light Processing Based 3D Printing. *Adv. Mater.* **2017**, *29* (15).

(43) Herzberger, J.; Sirrine, J. M.; Williams, C. B.; Long, T. E. Polymer Design for 3D Printing Elastomers: Recent Advances in Structure, Properties, and Printing. *Prog. Polym. Sci.* **2019**, *97*.

(44) Thrasher, C. J.; Schwartz, J. J.; Boydston, A. J. Modular Elastomer Photoresins for Digital Light Processing Additive Manufacturing. *ACS Appl. Mater. Interfaces* **2017**, *9* (45), 39708–39716.

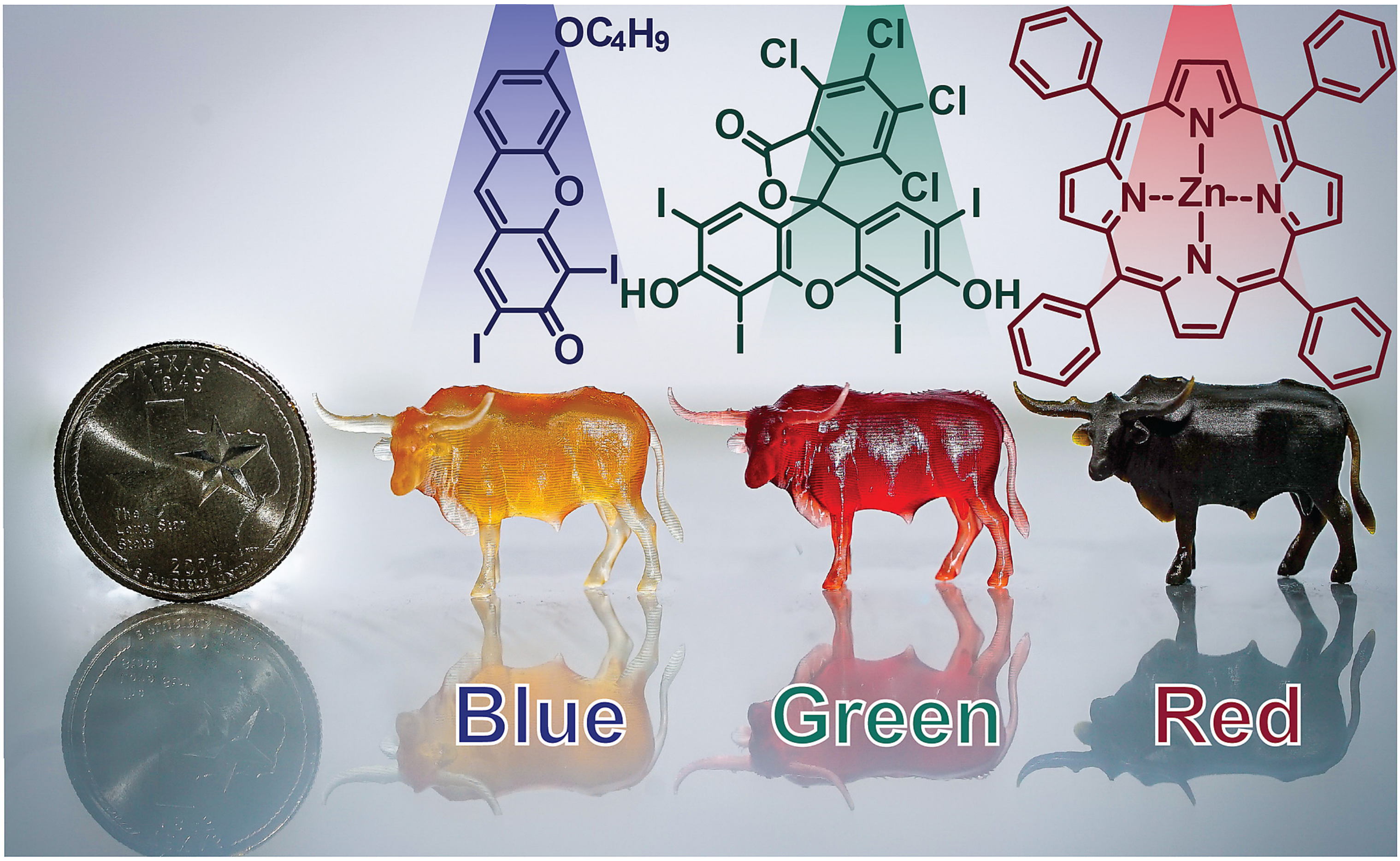
OC4H9
O
I
O
I
Cl
Cl
Cl
Cl
O
O
I
I
HO
O
OH
I
I
N
N--Zn--N
N
Blue
Green
Red

Supporting Information for

Rapid High Resolution Visible Light 3D Printing

Dowon Ahn, Lynn M. Stevens, Kevin Zhou, and Zachariah A. Page*

Department of Chemistry, The University of Texas at Austin, 105 East 24th Street, Stop A5300, Austin, Texas 78712, United States.

***Corresponding author:** zpage@utexas.edu

Table of Contents

EXPERIMENTAL DETAILS

Materials

Chemicals. All chemicals were used as received unless otherwise noted. Phenylbis(2,4,6-trimethylbenzoyl)phosphine oxide (BAPO), Rose Bengal lactone (RB), Eosin Y, 4-(diphenylphosphino)benzoic acid (4-dppba), tris(trimethylsilyl)silane (TTMSS), 2-phenylglycine, 5-methyl-1,3,4-thiadiazole-2-thiol, naphthofluorescein, and Sudan I were purchased from Sigma-Aldrich. Camphorquinone (CQ), Sudan IV, and Sudan black B were purchased from Chem-Impex. H-Nu 470, H-Nu 640, H-Nu 640MP, and 2-(butyryloxy)-*N*,*N*,*N*-trimethylethan-1-aminium butyltriphenylborate (Borate V), and [4-(octyloxy)phenyl](phenyl)iodonium hexafluoroantimonate diphenyliodonium (H-Nu254) were purchased from Spectra Group Limited. Zinc tetraphenylporphyrin (ZnTPP) and ethyl 4-(dimethylamino)benzoate (EDMAB) were purchased from TCI-America. Triethanolamine (TEOA) was purchased from Alfa Aesar. *N*,*N*-Dimethylacrylamide (DMA, Sigma-Aldrich), trimethylolpropane triacrylate (TMPTA, Alfa Aesar), 2-hydroxyethyl acrylate (HEA, TCI-America), and tetraethylene glycol diacrylate (TEGDA, TCI-America) were used as monomers/crosslinkers, and inhibitor was removed prior to use by running through a plug of aluminum oxide activated (basic, Brockmann I).

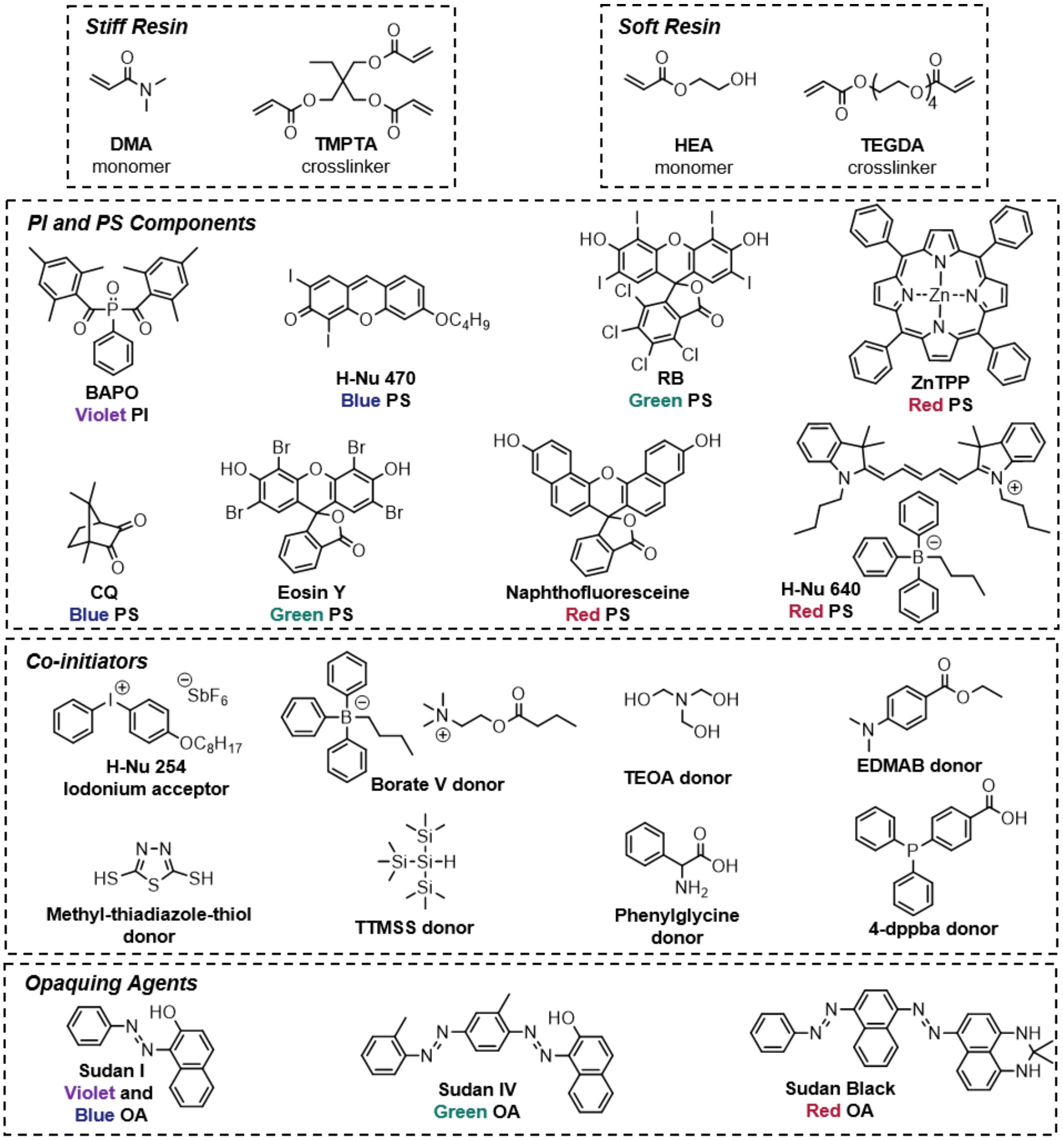

Figure S1. Chemical for different photopolymer resin components tested in the present study

Sample preparation

Resin formulation. Resin formulations are summarized in **Table S1**. Samples were formulated in the dark to avoid unnecessary onset of polymerization and sparged with nitrogen gas to remove dissolved oxygen in the resin prior to use. Resins could be stored for months without apparent loss in performance by storing in the dark at -20 °C.

Table S1. Resin formulations used in this study.

Formulation	PI/PS (wt%)[a]	Donor (wt%)[a]	Acceptor (wt%)[a]	OA (wt%)[a]	Resin (wt%)	X-linker (wt%)
Stiff violet	BAPO (0.5)	N/A	N/A	Sudan I (0.04)	DMA (80)	TMPTA (20)
Stiff blue	H-Nu470 (0.1)	Borate (0.2)	H-Nu254 (2)	N/A		
Stiff blue (CQ)	CQ (1)			Sudan I (0.01)		
Stiff green	RB (0.1)			Sudan IV (0.01)		
Stiff red	ZnTPP (0.3)			Sudan black (0.002)		
Soft violet	BAPO (0.5)	N/A	N/A	Sudan I (0.04)	HEA (99.9)	TEGDA (0.1)
Soft blue	H-Nu470 (0.1)	Borate V (0.2)	H-Nu254 (2)	Sudan I (0.01)		
Soft green	RB (0.1)			Sudan IV (0.01)		
Soft red	ZnTPP (0.3)			Sudan black (0.002)		

[a] Percent by weight of total monomer + crosslinker

Light sources

For FTIR spectroscopy and photorheology experiments, violet, blue, green, and red light was provided by collimated LEDs (LCS series, Mightex Systems) with an emission centered at 405, 460, 525, and 615 nm. These LEDs were used in combination with a current-adjustable driver (SLC-MA02-U, Mightex Systems) for intensity control, such that all intensities between experiments (printing, FTIR, and photorheology) could be matched. Light was delivered via a liquid light guide. Irradiation intensities were measured with a Thorlabs PM100D photometer equipped with silicon-based photodiode power sensor (S120VC, Thorlabs). Emission profiles were recorded with a QE pro spectrometer, in which the LED was connected to the fiber optic system using a 3 mm liquid lightguide from Mightex Systems (serial #: LLG-03-59-340-0800-1), as shown in **Figure S2**.

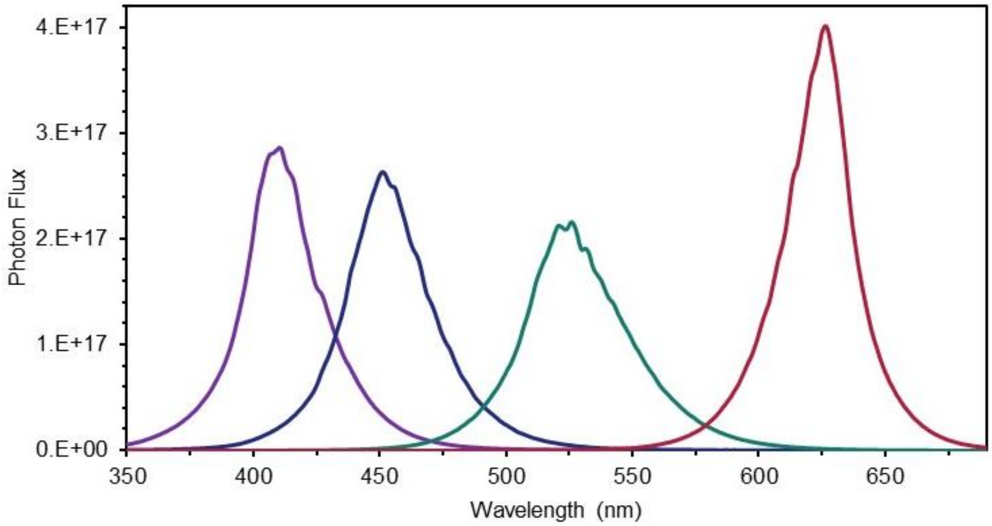

Figure S2. LED emission profiles centered at 405 nm (violet), 460 nm (blue), 525 nm (green), and 615 nm (red).

3D printing

Visible LEDs. 3D printing was performed using a custom-made, DLP-based 3D printer (Monoprinter, MA, USA), as depicted in **Figure S3**. The printer is compatible with four different exchangeable visible LEDs centered at 405 nm (violet, Luminus CBT-120-UV), 460 nm (blue, Luminus PT-120-B), 525 nm (green, Luminus PT-120-G), and 615 nm (red, Luminus PT-120-RA). Each LED contains a 12 mm^2 emission surface area and a maximum current up to 30 A. The full width at half maximum (FWHM) of each LED is 16, 20, 34, 19 for violet, blue, green, and red light, respectively.

Specification. The projector resolution was 1920 × 1080 pixels, with each pixel being 20 µm × 20 µm at the image plane. The minimum achievable layer thickness is 25 µm; however, most prints were performed at 100 µm/layer to provide consistent experimental parameters with RT-FTIR and photorheology, which required a minimum sample thickness of 100 µm to provide good signal-to-noise. The maximum build plane for the printer in its current configuration is 38.4 mm × 21.6 mm, and a vat with the dimensions of 56 mm × 35 mm × 25 mm (length × width × height) was used. A transparent fluorinated polymer film (Teflon FEP film, DuPont, 127 µm thick) was used as the base of the resin tank to provide a non-stick and somewhat flexible surface. Custom software (MonoWare) was used to import STL design files and digitally slice them into a sequence of 2D image files for projection. Detailed experimental parameter for 3D printing of visible light curable resin formulations are summarized in **Table S2**.

Samples were rinsed with ethyl acetate after each print, air dried, and post-cured with UV light centered at 370 nm (XICHEN Professional 36 Watt UV Beauty Salon Nail Dryer) for 20 min. unless otherwise noted.

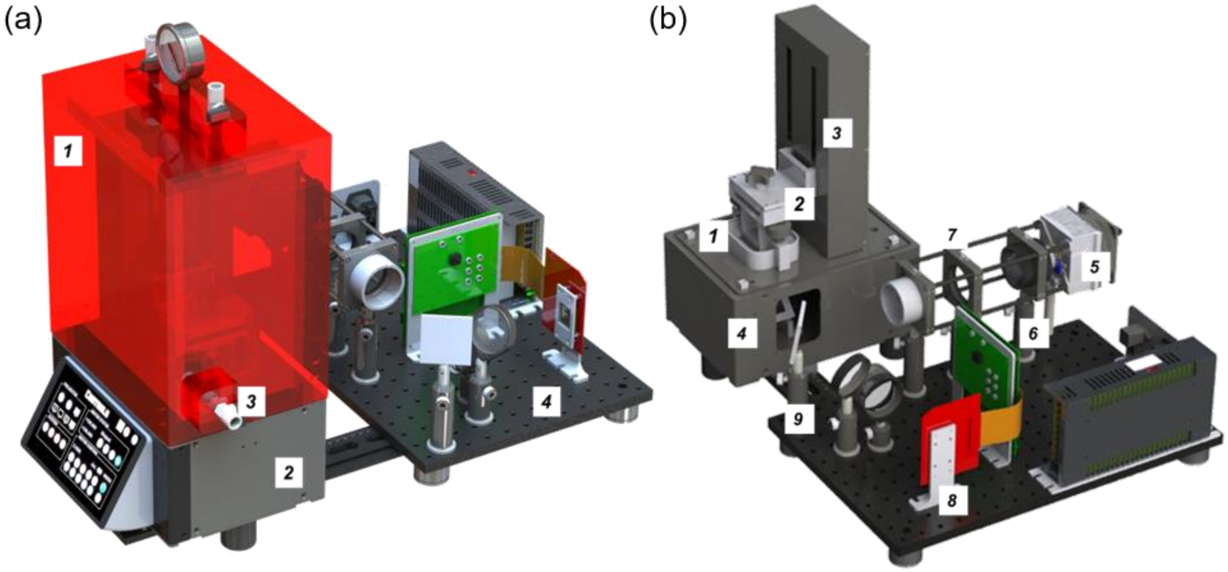

Figure S3. 3D rendering of custom DLP-based visible light 3D printer. (a) 3D printer with acrylic housing for inert gas purging. Components: (1) N_2 chamber, (2) DLP 3D printer, (3) N_2 inlet, and (4) visible LEDs projector. (b) 3D printer without acrylic housing. Mechanical components: (1) resin vat, (2) build platform, (3) Arduino stage. Optical components: (4) mirror, (5) LED with heat sink, (6) collimation lens, (7) diffuser, (8) digital mirror device (DMD), and (9) mirror.

Table S2. Experimental parameters for 3D printing of visible light curable resin formulations.

Formulation	Light intensities at vat surface (mW/cm^2)	Slice exposure time (sec)		Maximum rate of polymerization at the printer intensity (M/sec)	Build rate (mm/hr)	
		Base layer	Normal layer		Including re-positioning & re-coating process	Without re-positioning & re-coating process
Stiff violet	3.3	12	8	1.33 ± 0.05	29.5	45.0
Stiff blue	3.4	12	8	1.16 ± 0.05	29.5	45.0
Stiff green	1.8	12	8	1.09 ± 0.10	29.5	45.0
Stiff red	2.1	12	11	1.96 ± 0.31	23.7	32.7

Resolution Print. For rapid formulation optimization, a new printing method, referred here as "resolution print", was developed. A single layer of the printing process is illustrated in **Scheme S1**.

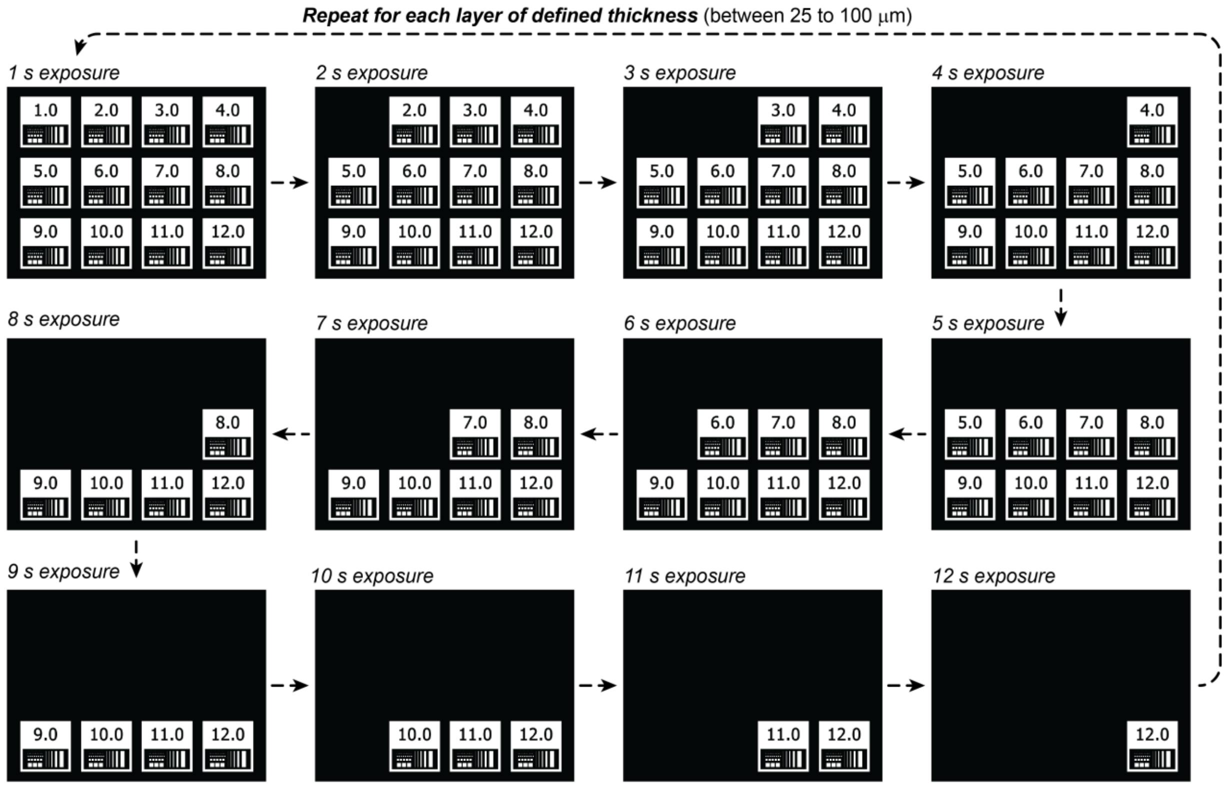

Scheme S1. Exposure sequence for a single layer using the "resolution print" method. The example shown has 12 squares and iterates exposure at 1 s increments from 1 to 12 s/layer.

CHARACTERIZATION

UV-visible spectroscopy

Thin resin samples. Light attenuation was measured using UV-visible absorption spectroscopy for stiff resin formulations (**Table S1**) without OA and with optimized [OA] between two glass slides separated by 100 µm thick spacer (**for Figure S4**) and spacers with various thicknesses (from 76 µm to 1270 µm for **Figure S5-S11**). Each sample was placed on a horizontal transmission accessory (Stage RTL-T, Ocean Optics) connected to a spectrometer (QE PRO-ABS, Ocean Optics) through optical fibers. A deuterium-tungsten halogen light sources (DH-2000-BAL) was used as the probe light. Spectra were collected from 200 to 800 nm. Extinction coefficients for PI and PS were calculated using Beers Law.

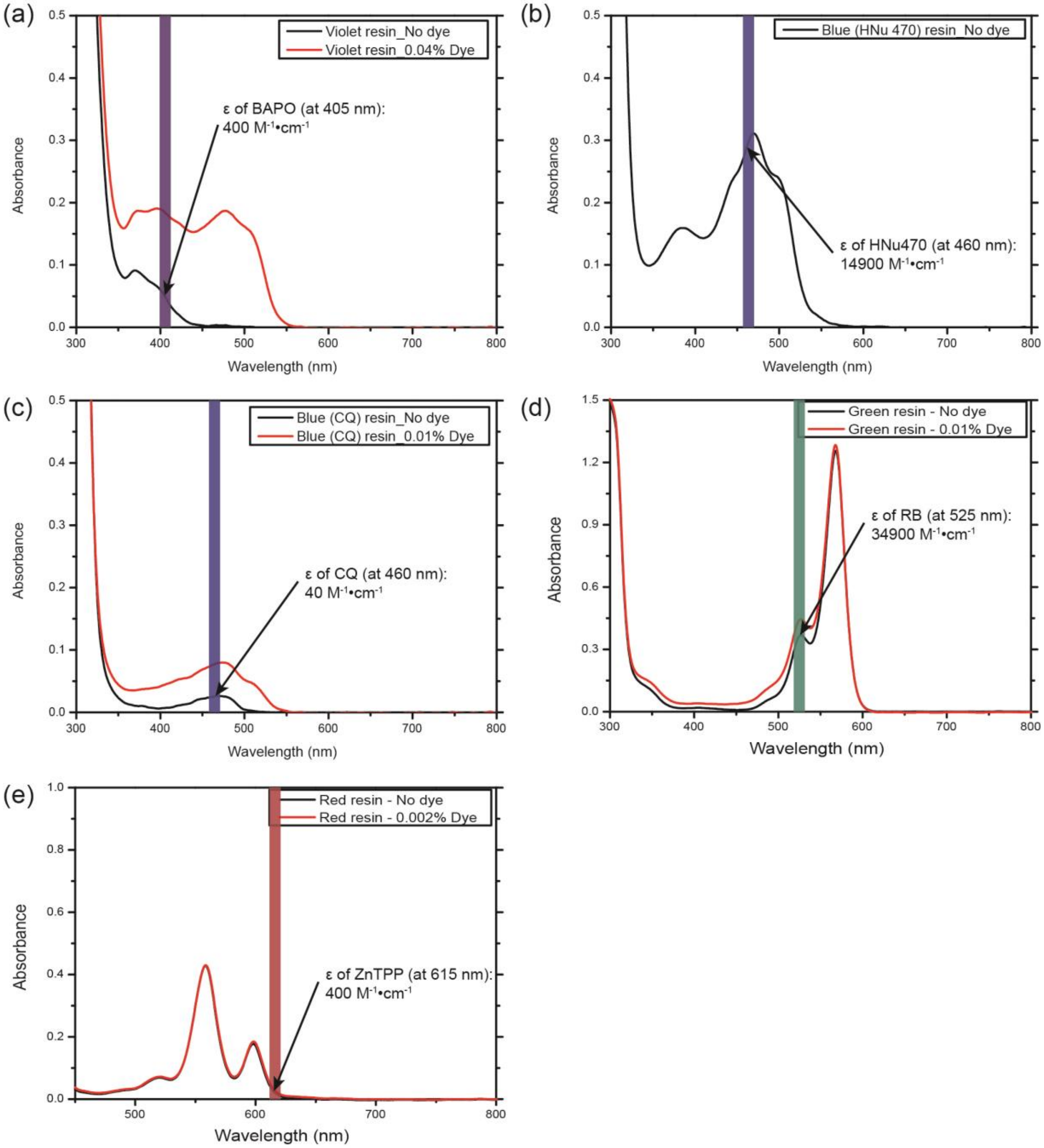

Figure S4. UV-vis absorption spectra for the PI and PS without OA and with optimized [OA]. Molar absorptivity for PI and PS at the peak emission of the corresponding LED is indicated as a colourful band. (a) Violet resin, (b) blue resin (w/ H-Nu470), (c) blue resin (w/ CQ), (d) green resin, and (e) red resin.

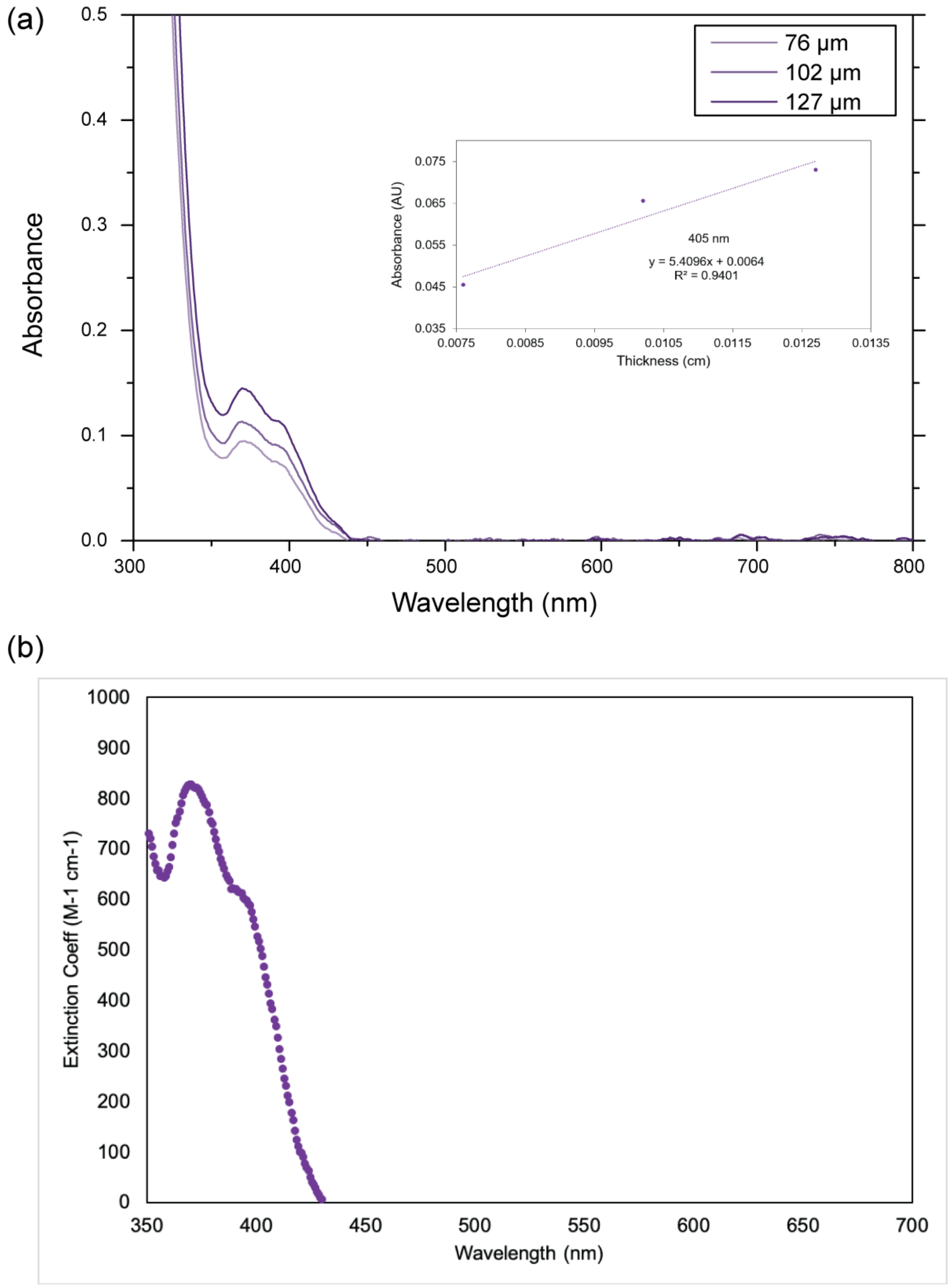

Figure S5. UV-vis absorption spectra for violet photoinitiator (BAPO) in DMA:TMPTA (4:1) at the optimized resin concentration. (a) Absorption vs thickness plot with Beer's Law plot as an inset. (b) Extinction vs wavelength plot.

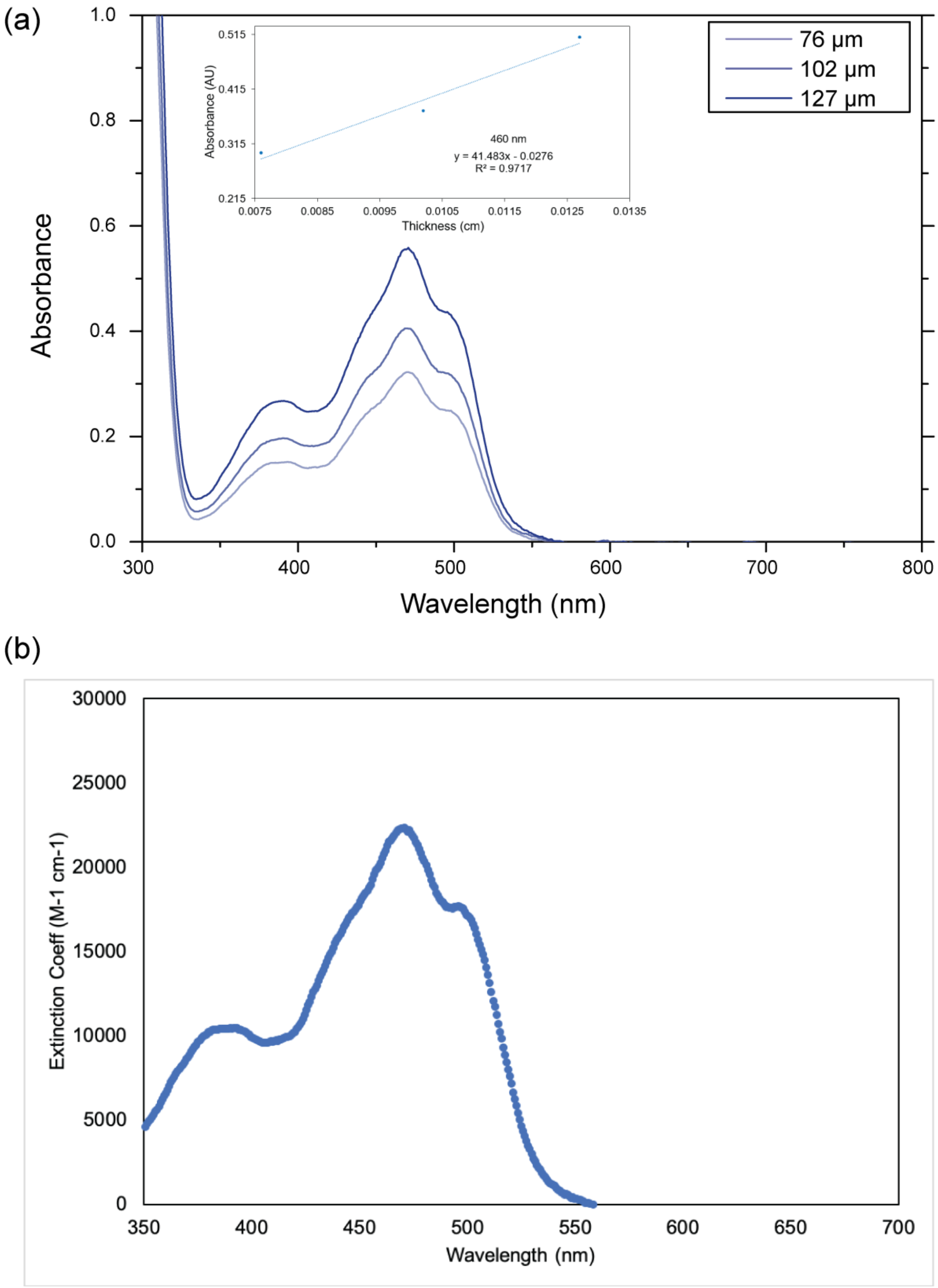

Figure S6. UV-vis absorption spectra for blue photosensitizer (H-Nu 470) in DMA:TMPTA (4:1) at the optimized resin concentration. (a) Absorption vs thickness plot with Beer's Law plot as an inset. (b) Extinction vs wavelength plot.

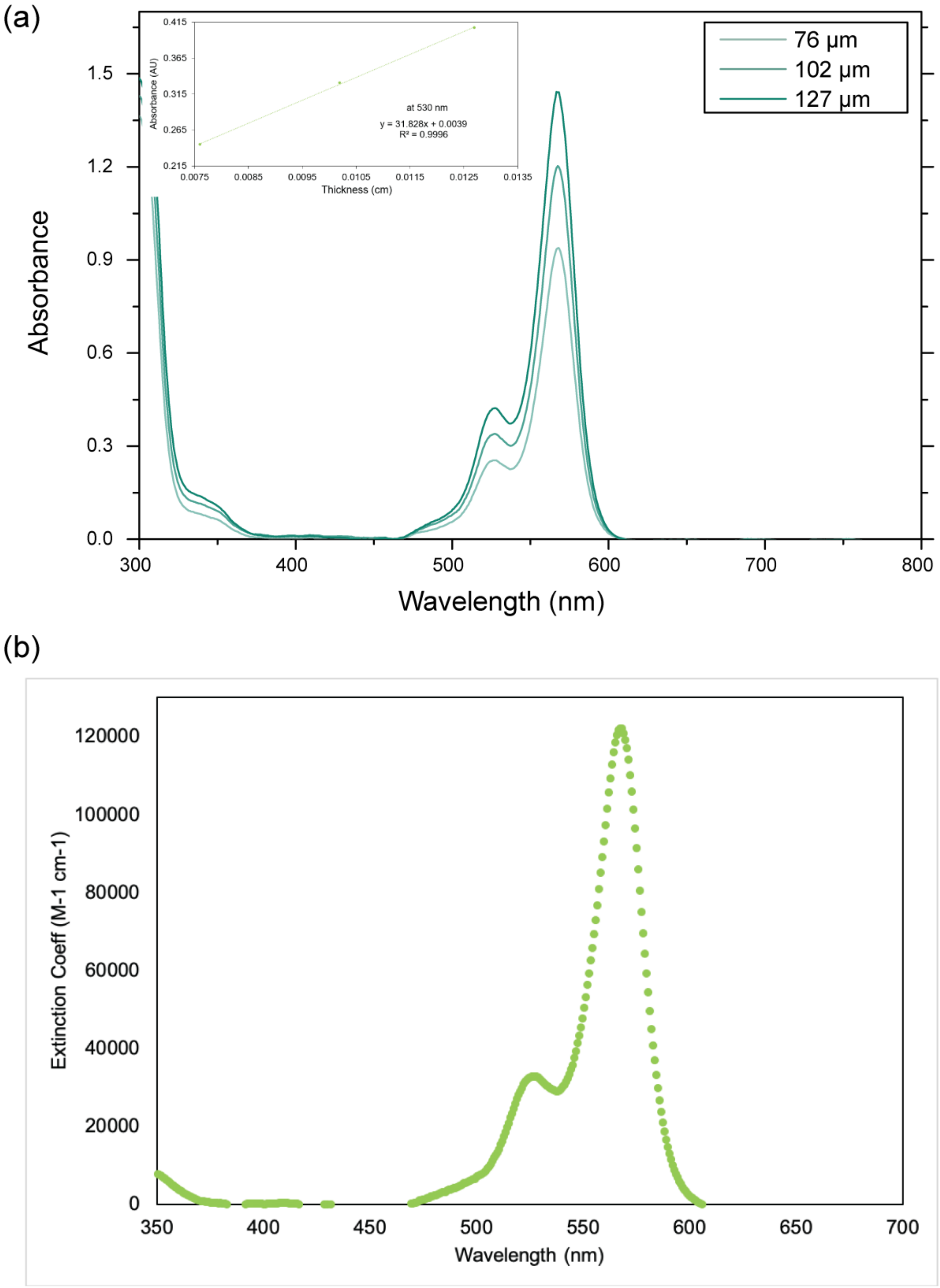

Figure S7. UV-vis absorption spectra for green photosensitizer (RB) in DMA:TMPTA (4:1) at the optimized resin concentration. (a) Absorption vs thickness plot with Beer's Law plot as an inset. (b) Extinction vs wavelength plot.

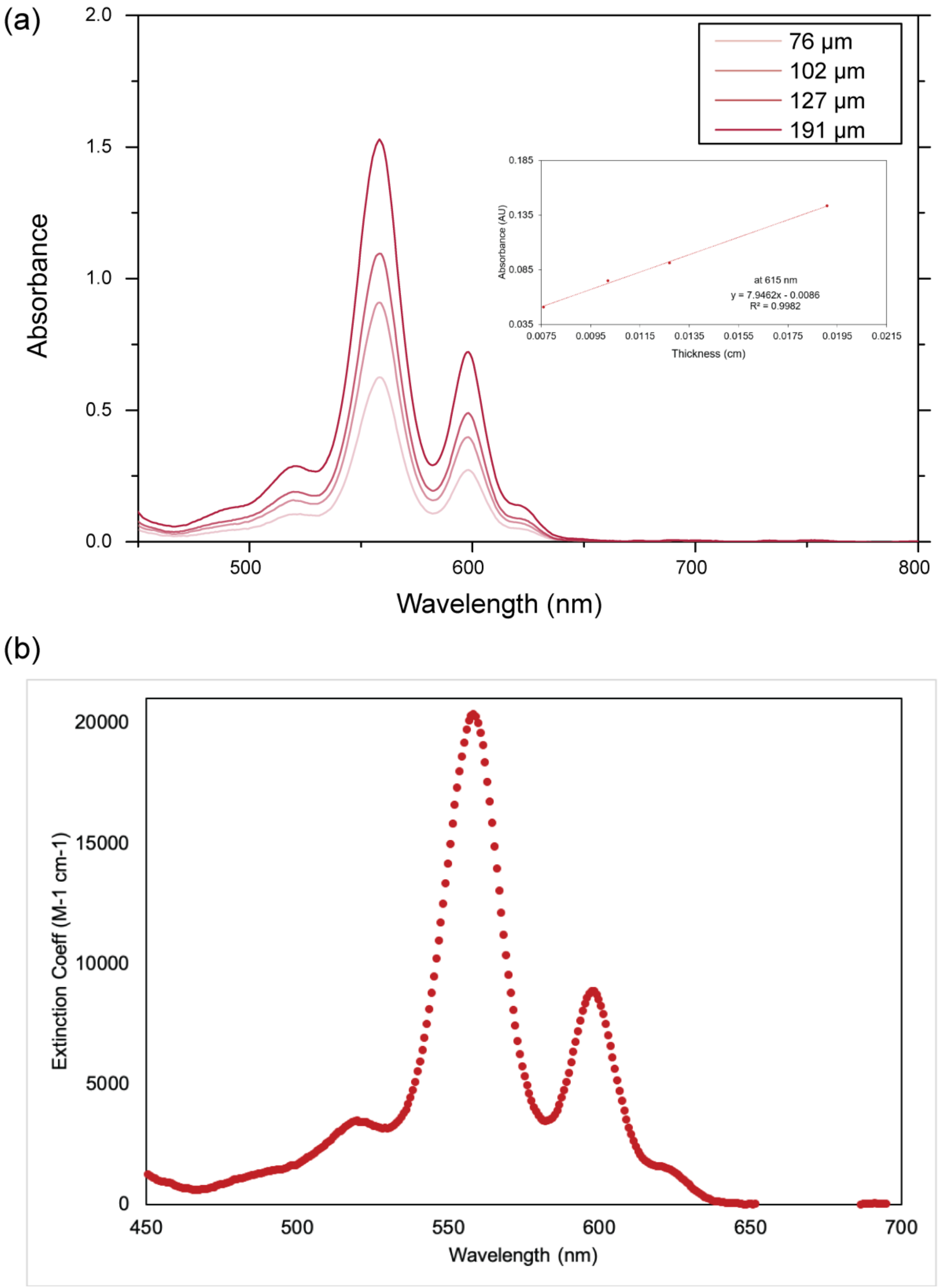

Figure S8. UV-vis absorption spectra for red photosensitizer (ZnTPP) in DMA:TMPTA (4:1) at the optimized resin concentration. (a) Absorption vs thickness plot with Beer's Law plot as an inset. (b) Extinction vs wavelength plot.

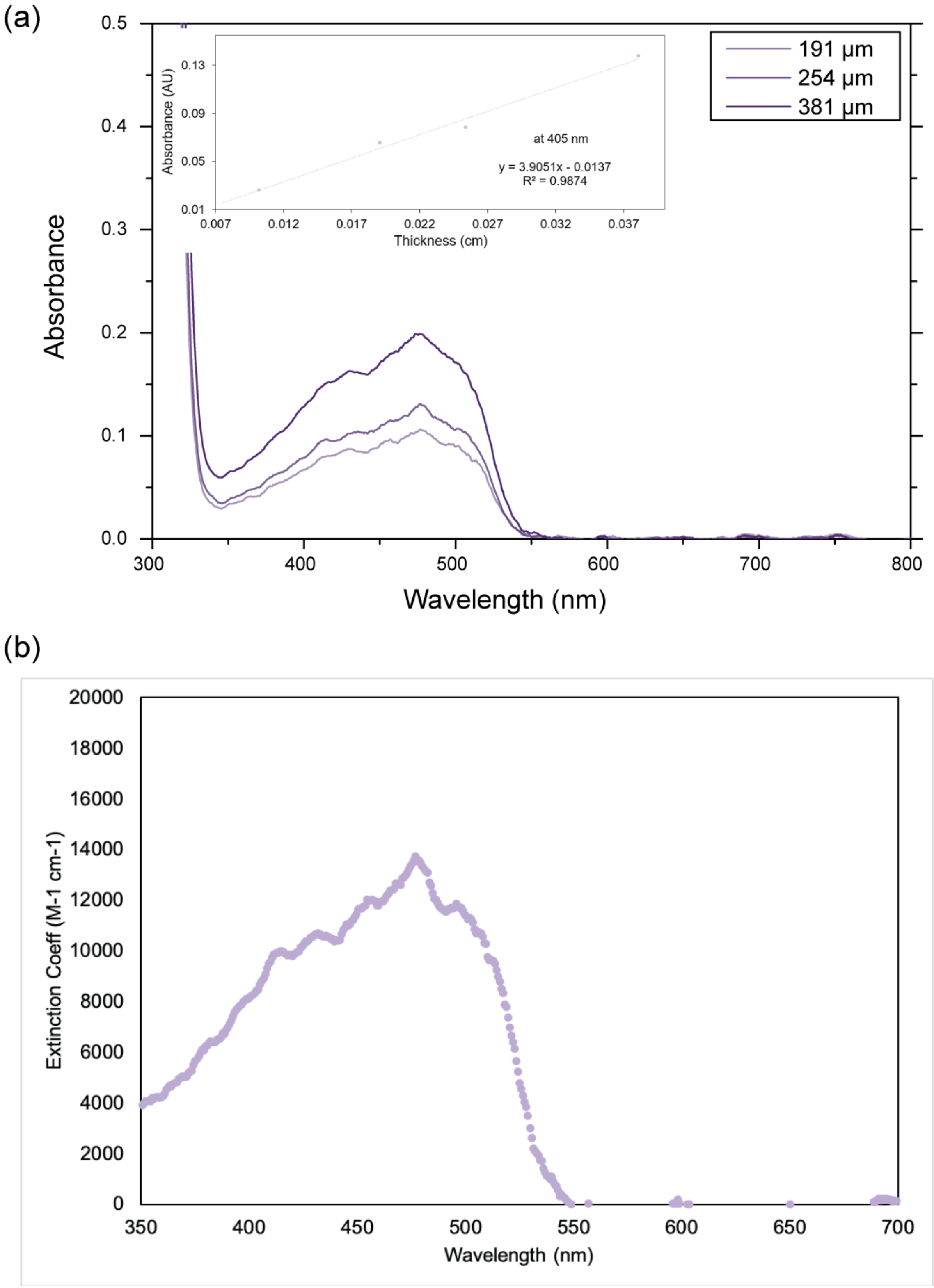

Figure S9. UV-vis absorption spectra for violet and blue opaquing agent (Sudan I) in DMA:TMPTA (4:1) at 0.01 wt%. (a) Absorption vs thickness plot with Beer's Law plot as an inset. (b) Extinction vs wavelength plot.

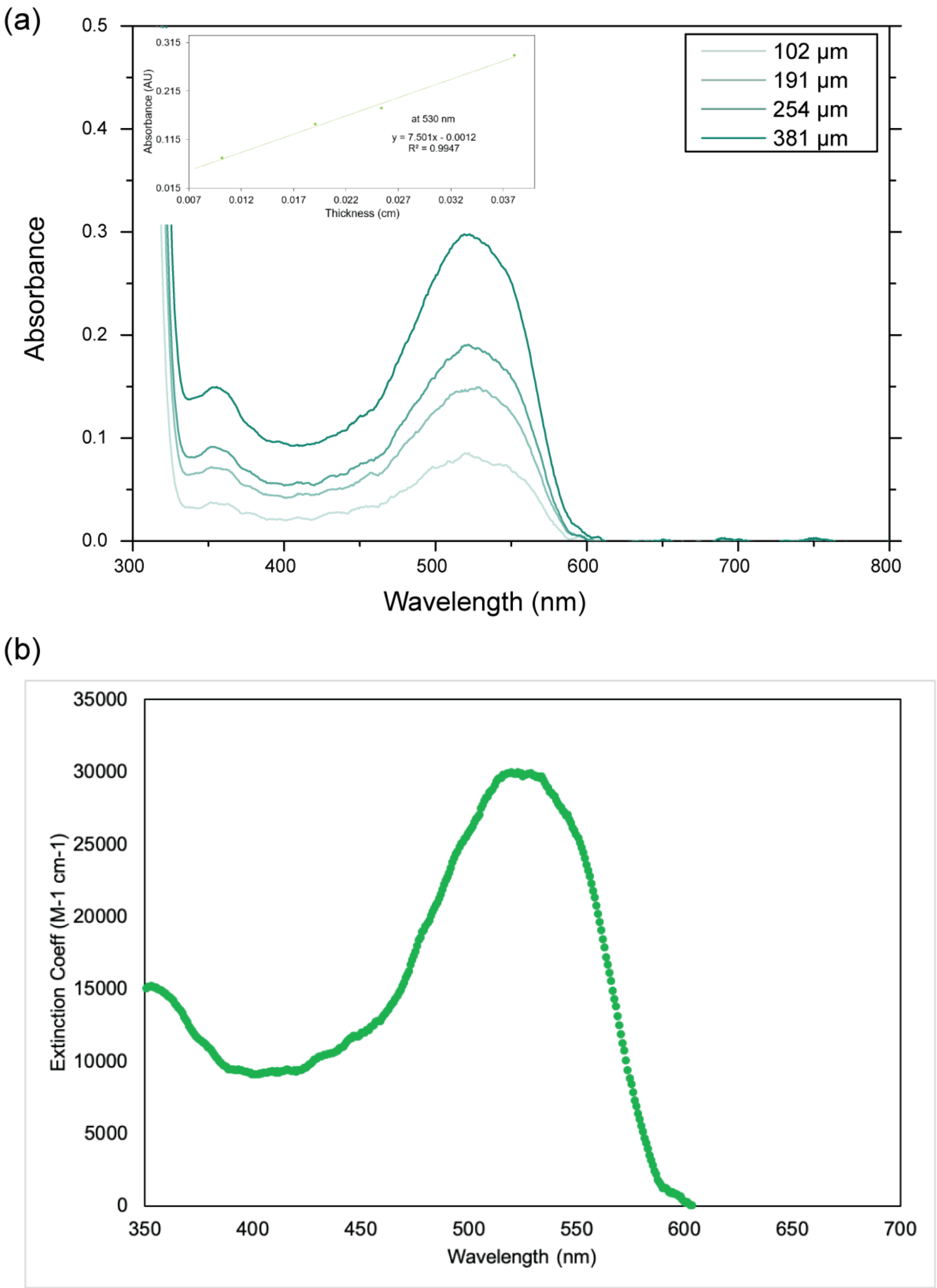

Figure S10. UV-vis absorption spectra for green opaquing agent (Sudan IV) in DMA:TMPTA (4:1) at 0.01 wt%. (a) Absorption vs thickness plot with Beer's Law plot as an inset. (b) Extinction vs wavelength plot.

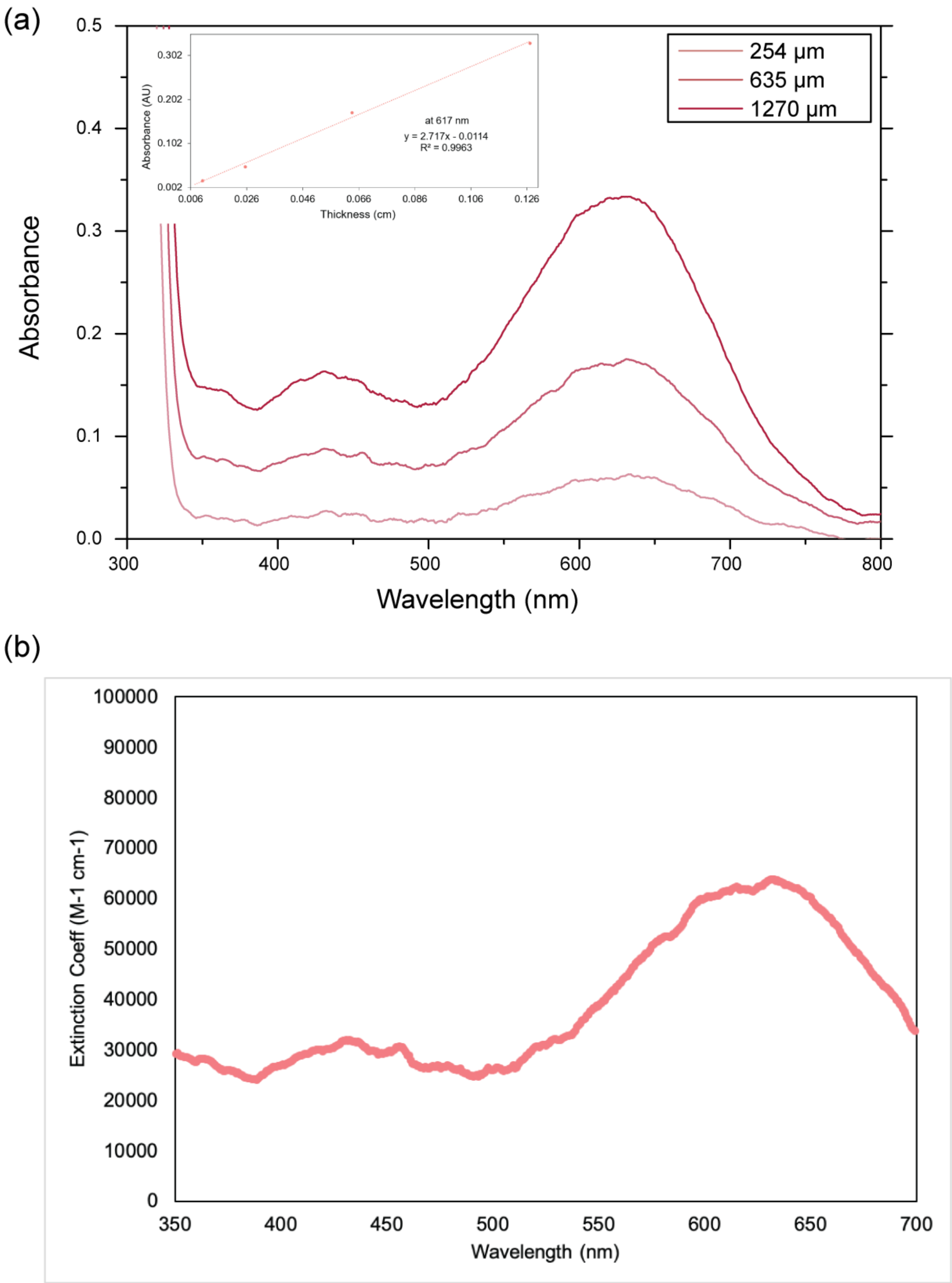

Figure S11. UV-vis absorption spectra for red opaquing agent (Sudan Black) in DMA:TMPTA (4:1) at 0.002 wt%. (a) Absorption vs thickness plot with Beer's Law plot as an inset. (b) Extinction vs wavelength plot.

Calculating photons absorbed. The photon flux was calculated based on the following supplemental equations:

$$E = hc/\lambda \qquad \textbf{\textit{(SE1)}}$$

where E = energy (mW), h = Plank's constant ($=6.626\times10^{-34}$J s), c = speed of light (3×10^{8} m/s)

$$W = n \times \left(\frac{E}{s}\right) \qquad \textbf{\textit{(SE2)}}$$

where W = watt , n = number of photons, E = energy of photons, and s = seconds

$$-logT = A = \varepsilon cl \qquad \textbf{\textit{(SE3)}}$$

where T = transmission, A = absorption (AU), ε = extinction coefficient (M^{-1} cm^{-1}), c = concentration (M), and l = path length (cm)

Equation ***SE1*** and ***SE2*** are used to convert the intensity output of the LED from (mW/cm^2 nm) into (# of photons/cm^2 s nm). T was calculated from equation ***SE3***, followed by the portion of photons absorbed as (1-T). Multiplying the light intensity by (1-T) provides the photon flux for each wavelength that's being absorbed by the sample. Finally, integrating each curve provided the total photon flux (or number of photons absorbed) for each sample (**Figure 2d**, **Figure S12**, and **Table S4**).

Table S3. LED output at the 3D printer intensity and corresponding photons absorbed by optimized PI and PS, and an [OA] of 1 mM*. Corresponds to Figure 2d in the main text.

	Violet	**Blue**	**Green**	**Red**
LED (# photons)	1.48E+19	1.48E+19	1.43E+19	1.87E+19
Photons absorbed by **PI** or **PS** (%)	8	53	57	17
Photons absorbed by **OA** (%)	19	33	43	50*

*Red [OA] = 0.5mm

Table S4. LED output at the 3D printer intensity and corresponding photons absorbed by optimized photosystem components. Corresponds to Figure S12 below.

	Violet	**Blue**	**Green**	**Red**
LED (# photons)	1.48E+19	1.48E+19	1.43E+19	1.87E+19
Photons absorbed by **PI** or **PS** (%)	8	53	57	17
Photons absorbed by **OA** (%)	29	n/a	14	6

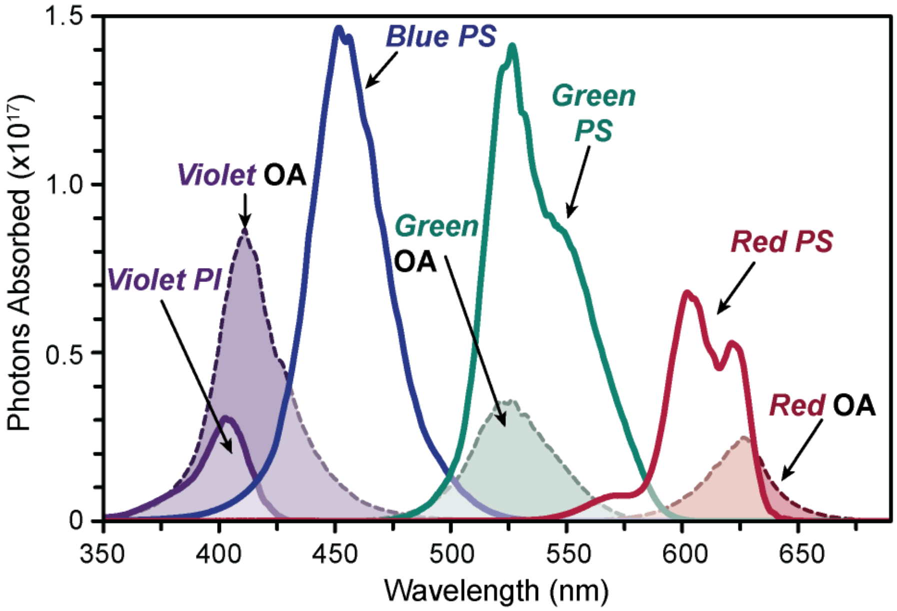

Figure S12. Plot of photons absorbed by each component in the photosystem under optimized printing conditions (corresponding to **Table S4** above). No OA was used in the optimized blue resin. Graph shows that more OA was used for the violet resin than the longer wavelengths.

Effect of oxygen on resolution prints

To examine the influence of oxygen on 3D printing, various stiff resin solutions without OA (unless otherwise noted) were printed under ambient conditions and compared to the same print under a weak flow of argon. The 'resolution print' method at a layer thickness of 100 μm was used with the corresponding red, green, blue, or violet LED.

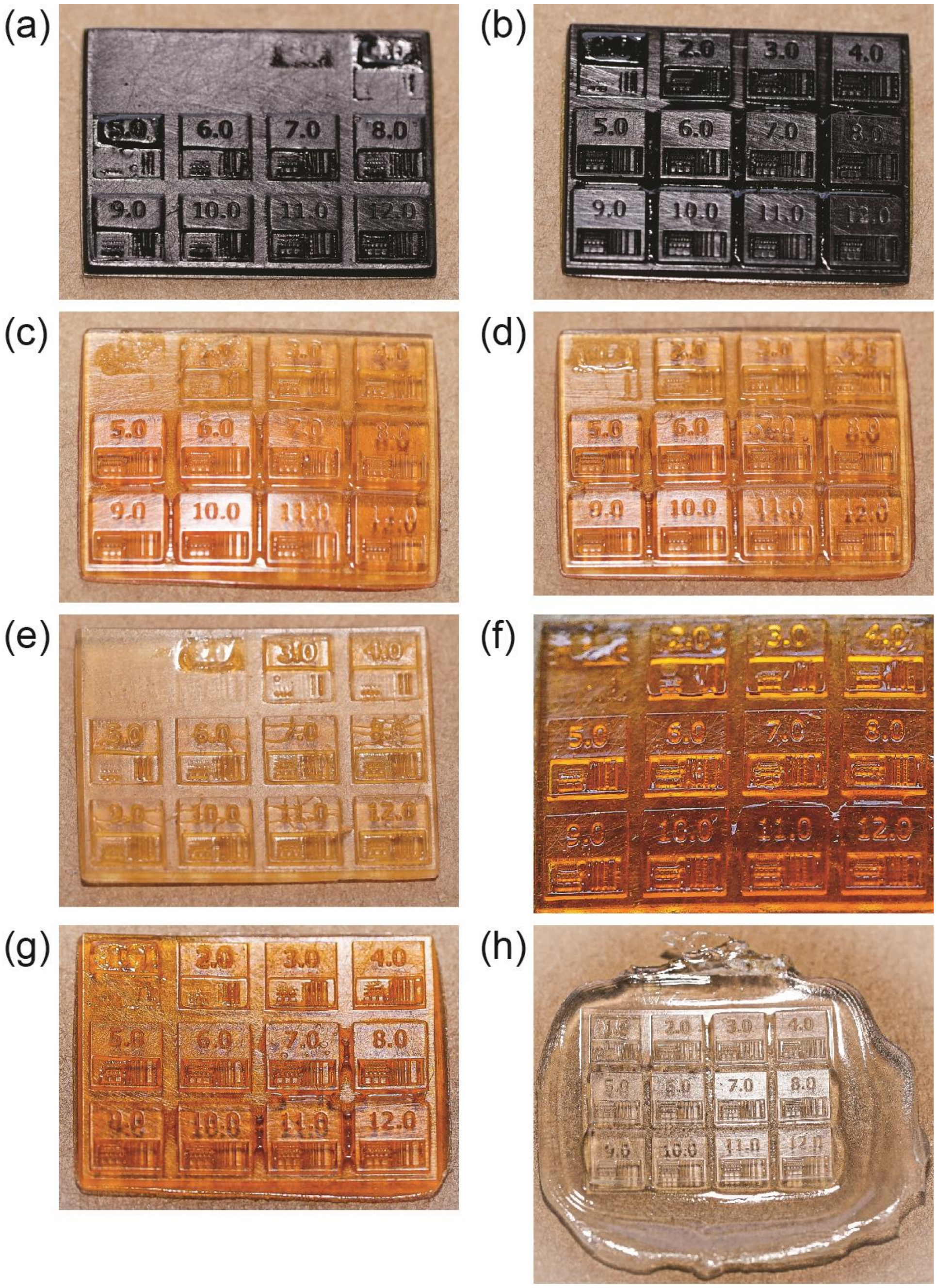

Figure S13. Optical images of resolution prints obtained from four different resins without OA. Red resin printed (a) under ambient condition and (b) under argon flow. Green resin printed (c) under ambient condition, and (d) under argon flow. Blue resin printed (e) under ambient condition, and (f) under argon flow. Violet resin printed (g) with optimized [OA] and (h) no OA.

Height analysis

Optical profilometer. A laser scanning optical 3D microscope (VK-X1100, Keyence) was used to map the topography of each square in the resolution prints (**Figure 3c** and **3d**). Both thickness and side-wall angle (SWA) were measured and Multifile analyzer software (Keyence) was used to determine the dimensions of observed objects. Heights and SWA values were determined from an average of 10 lines with 2 µm intervals. Both tight constraints (thickness >380 µm and SWA > 80°) and loose constraints (thickness > 370 µm and SWA > 70°) were highlighted in following figures as light vs dark bands, respectively.

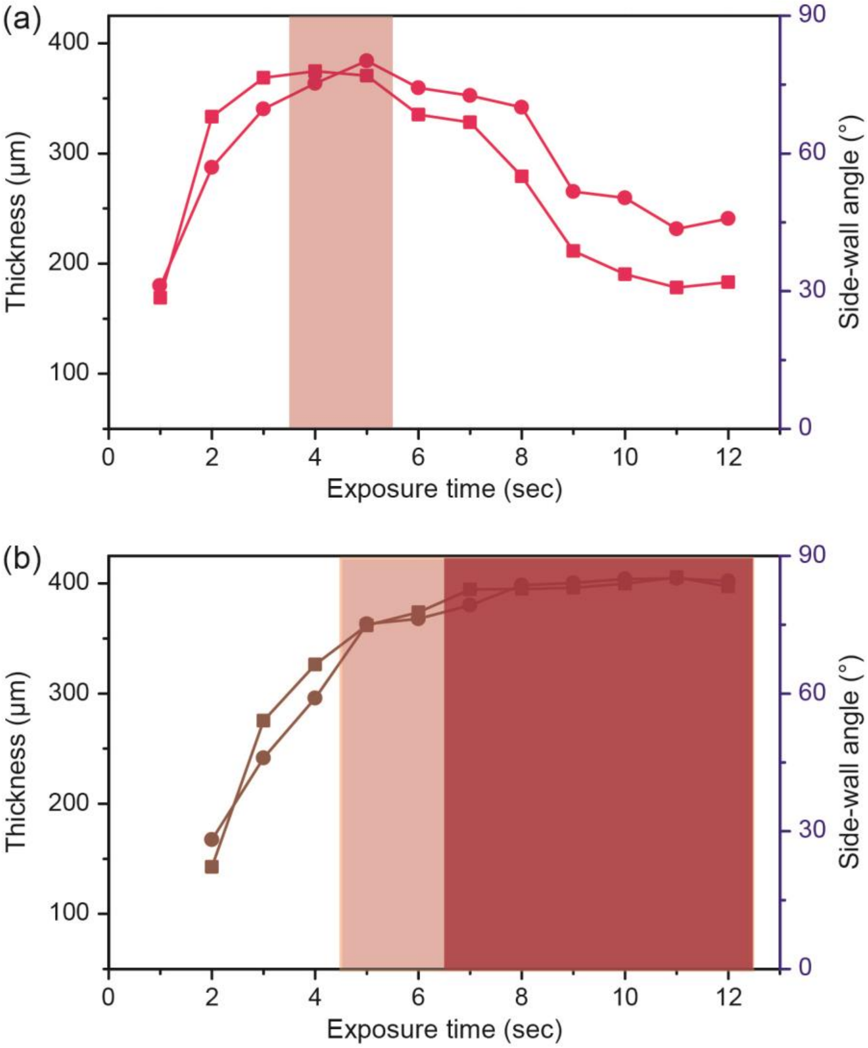

Figure S14. Plot of thickness and SWA as a function of exposure time/layer for red resins containing (a) no OA and (b) optimized OA (0.04wt%).

Digital microscope. A digital microscope (VHX-5000, Keyence) was used to create 3D map of the corners on each square, which was placed in the top half of each resolution print. Both thickness and side-wall angle (SWA) were measured. The digital microscope was elevated along the z-axis at a vertical pitch of 5 µm while continuously capturing 2D images, which were subsequently combined to construct a 3D image. To indicate the processing window, two different parameters for both thickness and SWA were applied. Both tight constraints (thickness >380 µm and SWA > 80°) and loose constraints (thickness > 370 µm and SWA > 70°) were highlighted in following figures as light vs dark orange bands, respectively.

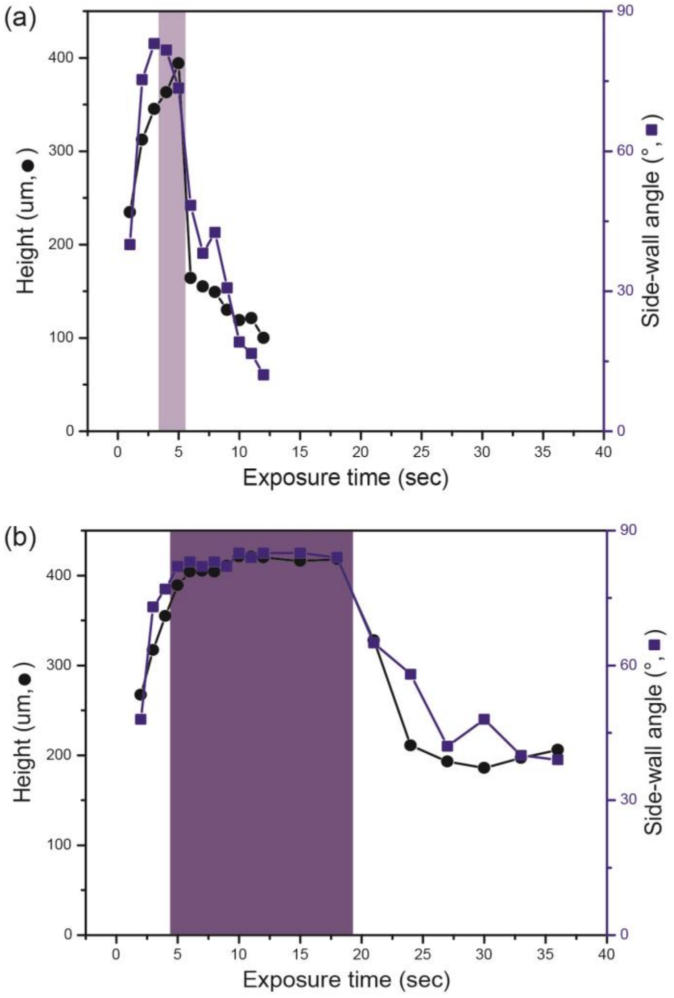

Figure S15. Plot of thickness and SWA as a function of exposure time/layer for violet resins containing (a) no OA and (b) optimized OA (0.04wt%).

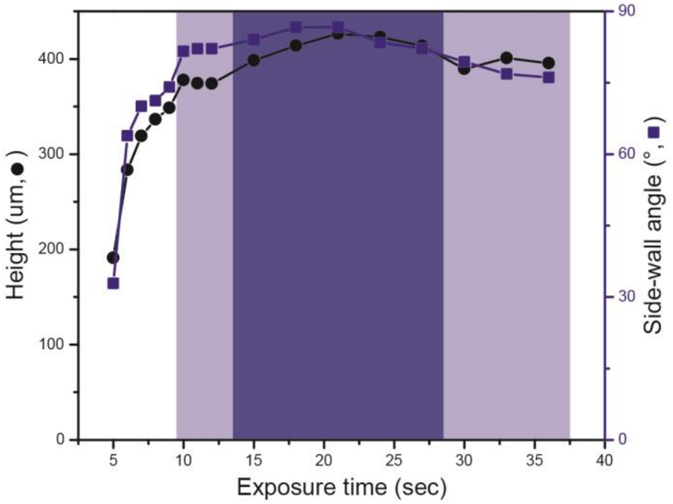

Figure S16. Plot of thickness and SWA as a function of exposure time/layer for blue resins (H-Nu 470) without OA.

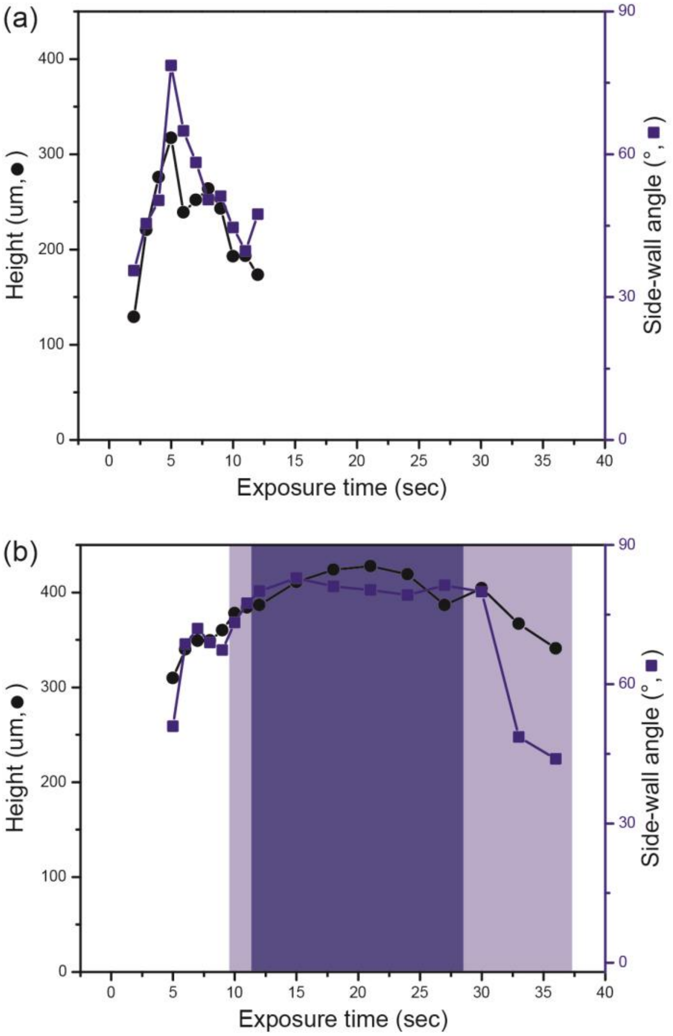

Figure S17. Plot of thickness and SWA as a function of exposure time/layer for blue resins (CQ) containing (a) no OA and (b) optimized OA (0.01wt%). Without incorporation of OA, CQ-containing blue resins result in substantial cure through, likely due to the low molar absorptivity of CQ at the blue LED.

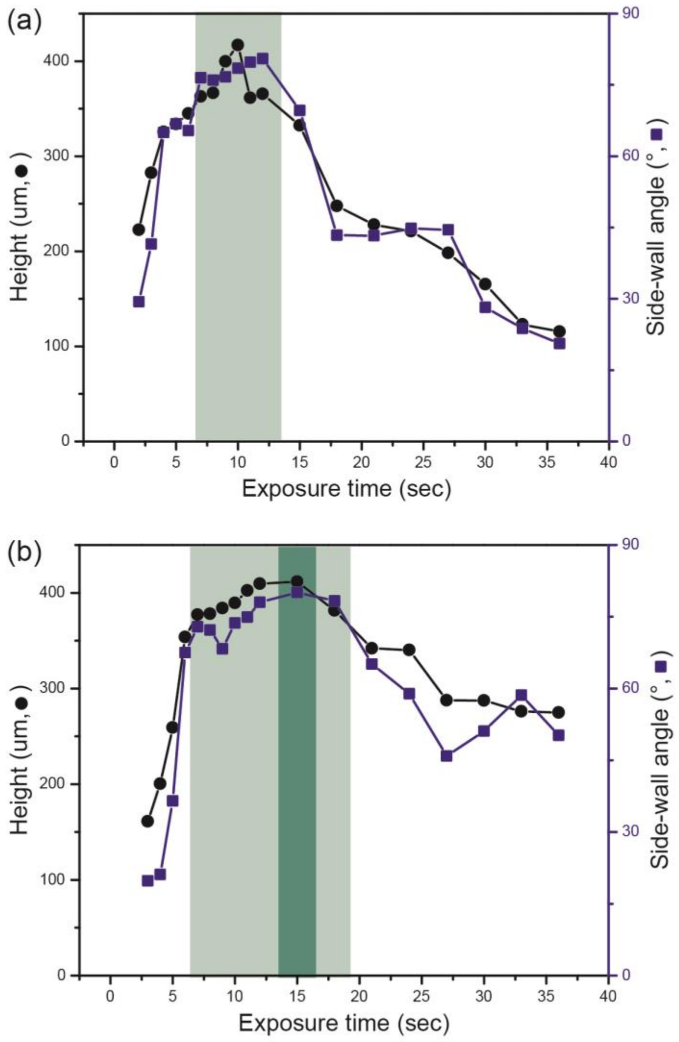

Figure S18. Plot of thickness and SWA as a function of exposure time/layer for green resins containing (a) no OA and (b) optimized OA (0.01wt%).

Surface area analysis

Optical profilometer. Top surface area of 1, 2, 4, 8, 16 pixel-wide patterns (bottom half of each square on resolution print) was measured to determine the optimal OA concentrations and slice exposure times. Based on the height of the optical images collected from the optical profilometer, the areas of the top surface of the pillars were recorded for each resin with varying OA concentrations (**Figure 3d**). Multifile analyzer software (Keyence) was used to calculate the surface area directly from the images obtained using the optical profilometer. For clarity, images were post-processed using Adobe Illustrator. This post-processing directly takes pixels identified to be above a certain height threshold in the optical profilometry image and converts them to a monochromatic rendering, as shown in **Scheme S2**.

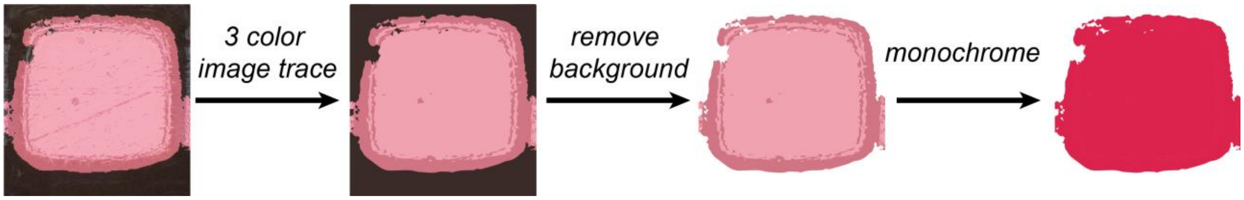

Scheme S2. Image processing for surface area analysis to improve clarity. Note that surface area determination from optical profilometry traces was determined prior to the above processing using the multifile analyzer software associated with the instrument.

Digital microscope. Top surface area of 8 and 16 pixel-wide patterns (bottom half of each square on resolution print) was measured to determine the optimal OA concentrations and exposure times/layer. Based on the brightness of the optical images collected from the digital microscope, the areas of the top surface of the pillars were recorded for each resin with varying OA concentrations (**Figure S19**).

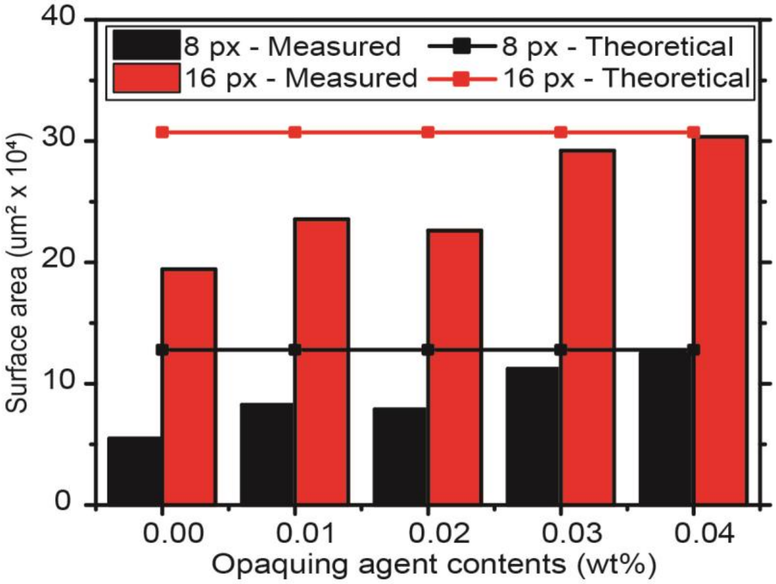

Figure S19. Plots of top surface areas for 8 and 16 pixel-wide pillars versus [OA] for violet resins. Sudan I (from 0wt% to 0.04 wt%) was added as OA. Theoretical values are displayed as dashed line.

Real time Fourier transform infrared spectroscopy

Sample preparation and measurement. Resin formulations were introduced between two glass slides separated by spacers (either 100 µm or 250 µm) to maintain a constant sample thickness over the course of photopolymerization. Each sample was placed in a horizontal transmission accessory (A043-N/Q, Bruker) equipped with the FTIR spectrometer (INVENIO-R, Bruker) controlled via OPUS spectroscopy software. Spectra were collected from 2000 to 7000 cm^{-1} at a rate of 1 scan every 0.36 seconds. To mitigate oxygen inhibition, argon was passed over the sample for the duration of the experiment (unless otherwise noted). The functional group conversion upon light exposure was determined by monitoring the disappearance of the peak area centered at 6161 cm^{-1} corresponding to the acrylate C=C stretch. **Figure S20** shows the FTIR setup with horizontal transmission accessory used for real time monitoring of photopolymerization.

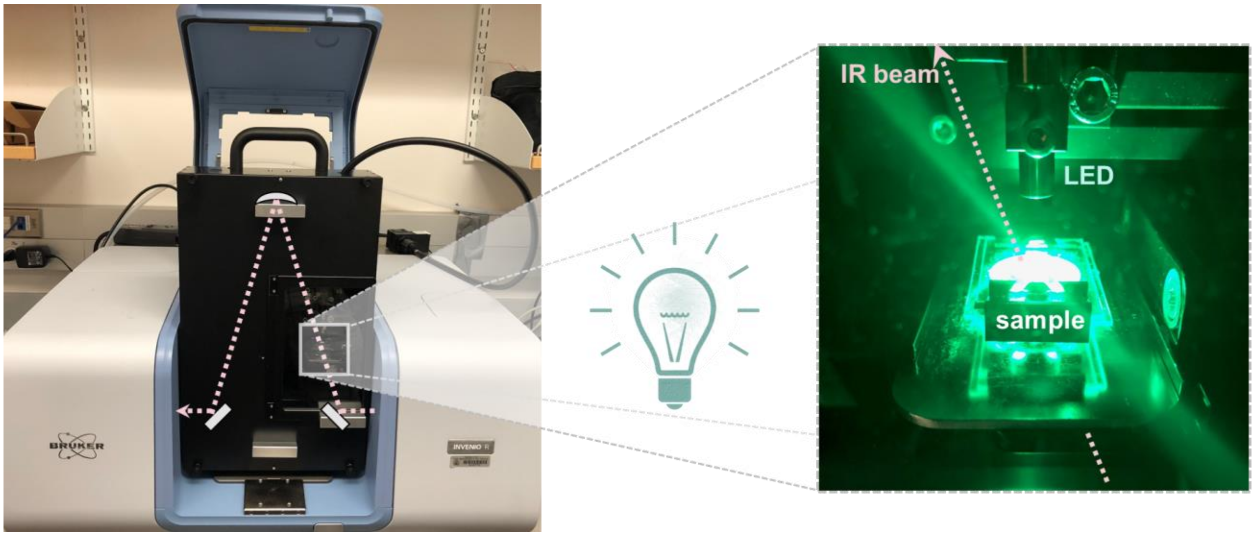

Figure S20. FTIR setup with horizontal transmission accessory for real time monitoring of photopolymerization.

Table S5. Resin formulation screening and experimental parameters for FTIR measurements. All samples were measured with a 250 µm thickness.

Wavelength (nm)	Light intensity (mW/cm^2)	PI/PS (wt%)	Co-initiator 1 (wt%)	Co-initiator 2 (wt%)	Photopolymerization rate (M/s)
530	10	(0.1) Eosin Y	(0.2) Borate V	(2) H-Nu254	0.97
617	10	(0.05) H-Nu640	(0.2) Borate V	(2) H-Nu254	0.09
		(0.1) H-Nu640	(0.2) Borate V	(2) H-Nu254	0.07
		(0.05) H-Nu640MP	(0.2) Borate V	(2) H-Nu254	0.10
		(0.1) H-Nu640MP	(1) Borate V	(2) H-Nu254	0.10
		(0.1) H-Nu640MP	(1) TEOA	(2) H-Nu254	0.03
		(0.1) H-Nu640MP	(1) EDMAB	(2) H-Nu254	0.03
		(0.1) H-Nu640MP	(1) 4-dppba	(2) H-Nu254	0.05
		(0.1) H-Nu640MP	(1) TTMSS	(2) H-Nu254	0.03
		(0.1) H-Nu640MP	(1) Phenylglycine	(2) H-Nu254	0.03
		(0.1) H-Nu640MP	(1) Methyl-thiadiazole-thiol	(2) H-Nu254	0.09
		(0.1) Rose Bengal	(0.2) Borate V	(2) H-Nu254	No rxn
		(0.1) Naphthofluorescein	(0.2) Borate V	(2) H-Nu254	No rxn
		(0.1) H-Nu640MP	(0.2) TEOA	(2) H-Nu254	No rxn
		(0.1) ZnTPP	(1) Borate V	(2) H-Nu254	1.90
		(0.1) ZnTPP	(0.2) Borate V	(2) H-Nu254	2.68
	5	(0.1) ZnTPP	(0.2) Borate V	(2) H-Nu254	2.33
	2	(0.1) ZnTPP	(0.2) Borate V	(2) H-Nu254	0.71
		(0.3) ZnTPP	(0.2) Borate V	(2) H-Nu254	1.74
		(0.5) ZnTPP	(0.2) Borate V	(2) H-Nu254	0.95
	1.85	(0.1) ZnTPP	(0.2) Borate V	(2) H-Nu254	0.43
		(0.2) ZnTPP	(0.2) Borate V	(2) H-Nu254	0.77
		(0.3) ZnTPP	(0.2) Borate V	(2) H-Nu254	1.11
		(0.4) ZnTPP	(0.2) Borate V	(2) H-Nu254	0.85
		(0.5) ZnTPP	(0.2) Borate V	(2) H-Nu254	1.02

Refer to ***Figure S1*** *for chemical structures*

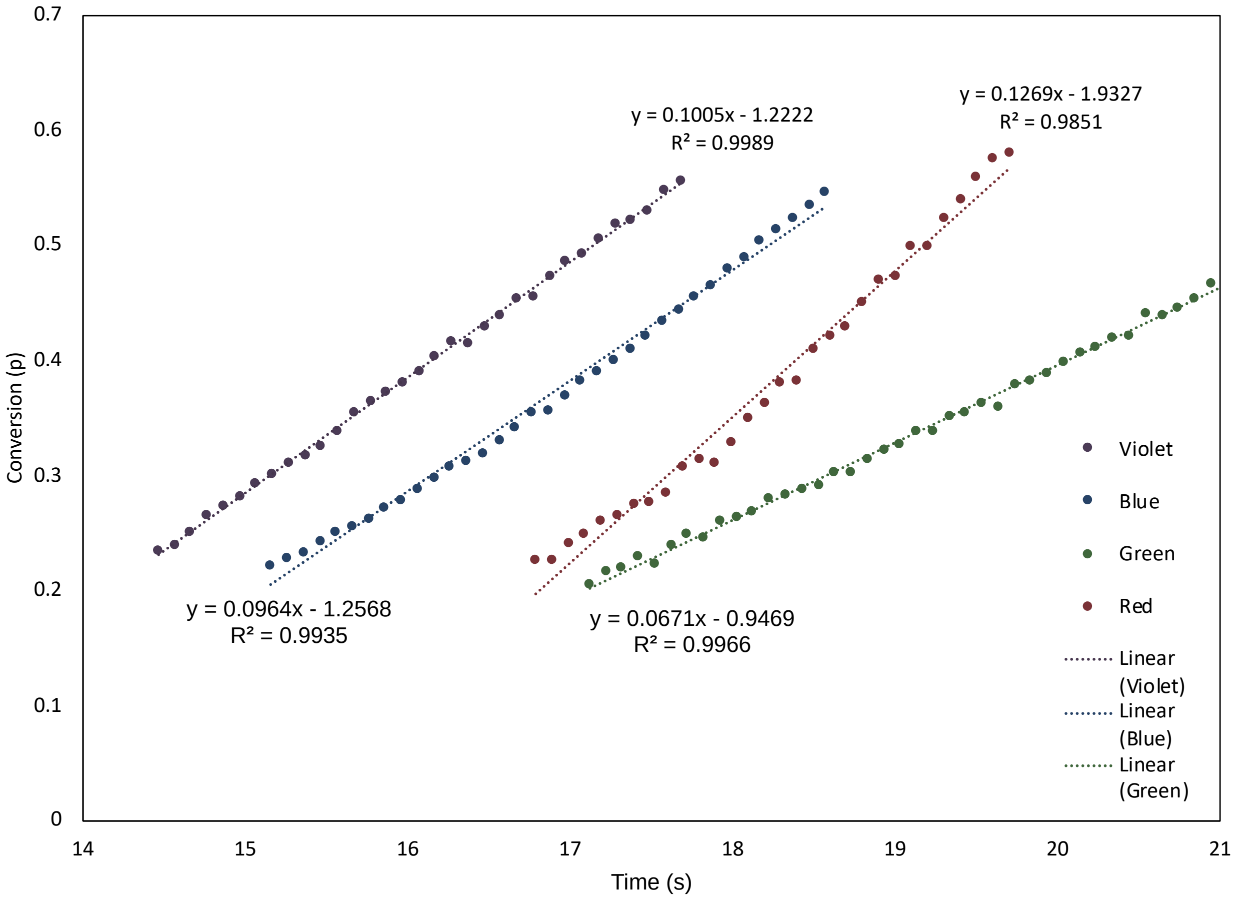

Figure S21. RT-FTIR rate analysis of resins at optimized OA concentration and printer light intensity (corresponding to **Figure 4b** in the main manuscript).

Effect of oxygen and OA on photopolymerization rate. Photopolymerizations were performed in triplicate with and without oxygen removal via degassing and with and without OA. The optimized stiff resin (**Table S1**), a sample thickness of 100 μm, and printer intensities (**Table S2**) were used. Maximum apparent polymerization rates were calculated from the steepest slopes post-LED exposure starting at 10 s. Traces provided are averages of all three runs.

Table S6. Summary of the effect of oxygen and OA on apparent photopolymerization rates for optimized resins. Fully optimized conditions are highlighted in grey.

Wavelength (nm)	Atmosphere	Opaquing Agent	Photopolymerization rate (%/s)	Photopolymerization rate (M/s)
405 (violet)	inert (argon)	Optimized OA	10.0	0.86
	ambient	Optimized OA	9.2	0.79
	inert (argon)	No OA	11.6	1.00
460 (blue)	inert (argon)	Optimized OA	9.6	0.83
	ambient	Optimized OA	8.9	0.77
525 (green)	inert (argon)	Optimized OA	6.7	0.58
	ambient	Optimized OA	6.2	0.54
	inert (argon)	No OA	10.6	0.91
615 (red)	inert (argon)	Optimized OA	12.7	1.10
	ambient	Optimized OA	3.2	0.28
	inert (argon)	No OA	7.8	0.67

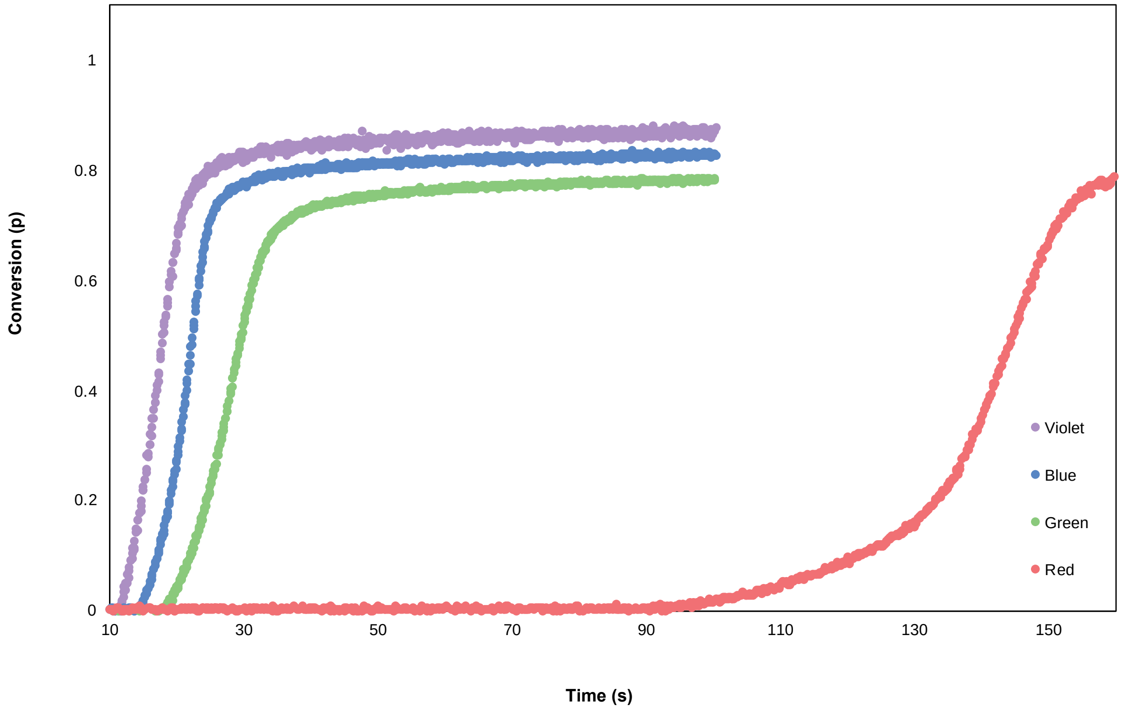

Figure S22. RT-FTIR studies of resins not degassed at optimized OA concentration & printer light intensity

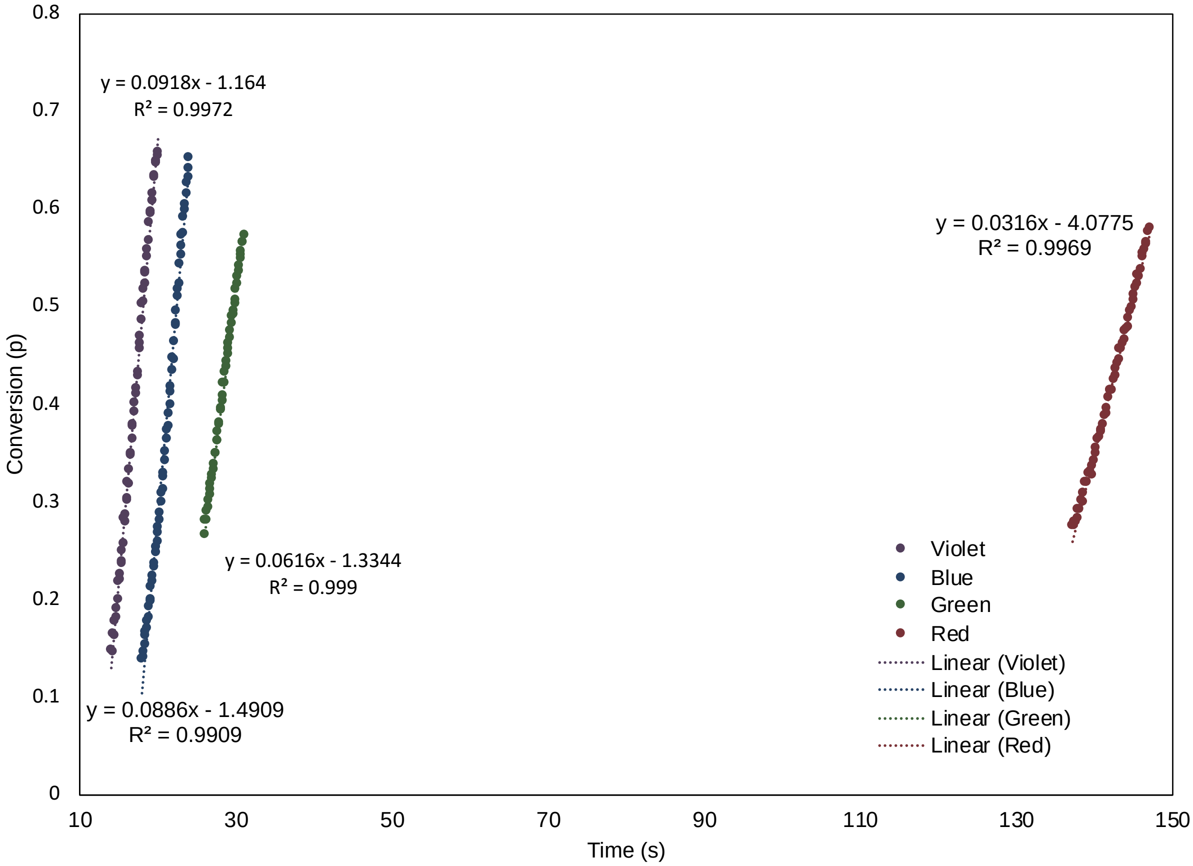

Figure S23. RT-FTIR rates of resins not degassed at optimized OA concentration & printer light intensity

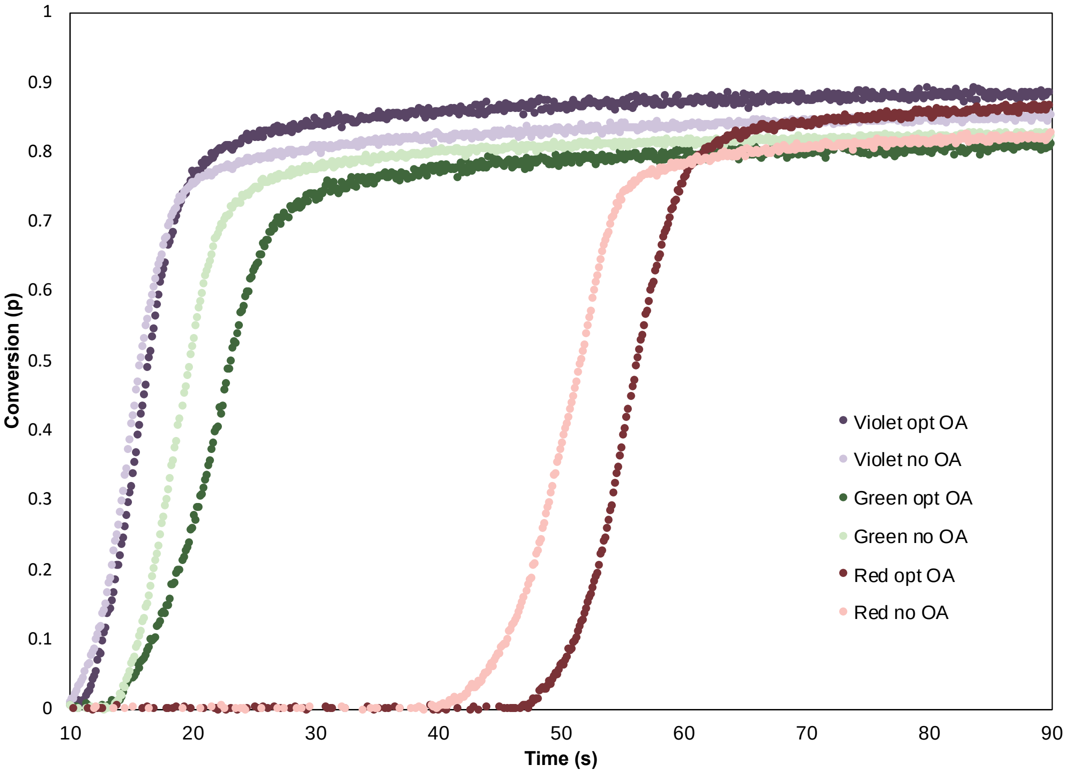

Figure S24. RT-FTIR studies of resins without OA and with optimized OA at the printer light intensity. Resins were degassed with N_2, but inert gas was not flowed over the sample during measurement, thus resulting in a notable inhibition period for the red resin.

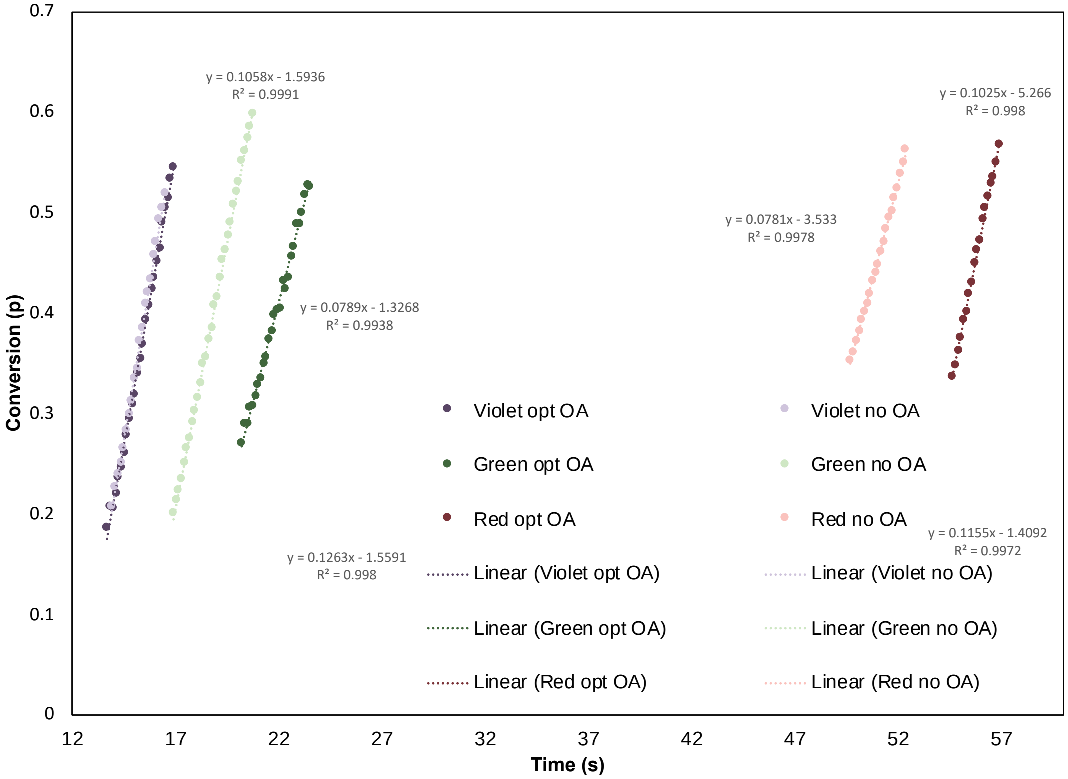

Figure S25. RT-FTIR rates of resins degassed at with no OA and optimized OA concentration at printer light intensity.

Photopolymerization at different LED intensities. Photopolymerizations were performed in triplicate at different LED intensities using the optimized stiff resin (**Table S1**) and a sample thickness of 100 µm. Maximum apparent polymerization rates were calculated from the steepest slopes post-LED exposure starting at 10 s. Traces provided are averages of all three runs.

Table S7. Summary of the effect of light intensity on apparent photopolymerization rates for optimized resins with OA. Results at the printer intensity are highlighted in grey.

Wavelength (nm)	Light Intensity (mW/cm^2)	Photopolymerization rate (%/s)	Photopolymerization rate (M/s)
405 (violet)	1	4.2	0.36
	3.3	9.7	0.84
	5	12.1	1.04
	10	18.3	1.58
460 (blue)	1	4.7	0.41
	3.4	10.4	0.90
	5	11.9	1.03
	10	17.0	1.47
525 (green)	1	5.3	0.46
	1.8	6.9	0.60
	5	11.5	0.99
	10	13.6	1.17
615 (red)	1	8.5	0.73
	2.1	14.3	1.23
	5	19.3	1.67
	10	22.9	1.98

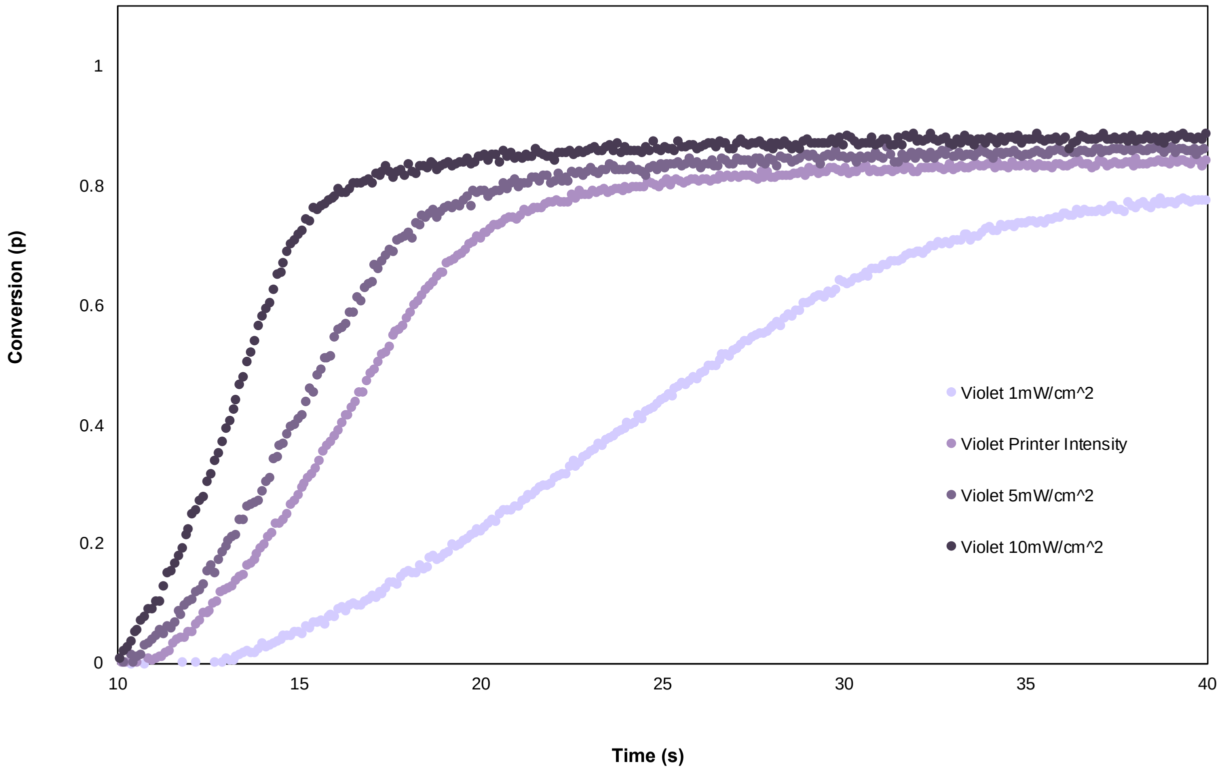

Figure S26. RT-FTIR study of violet resin at various light intensities

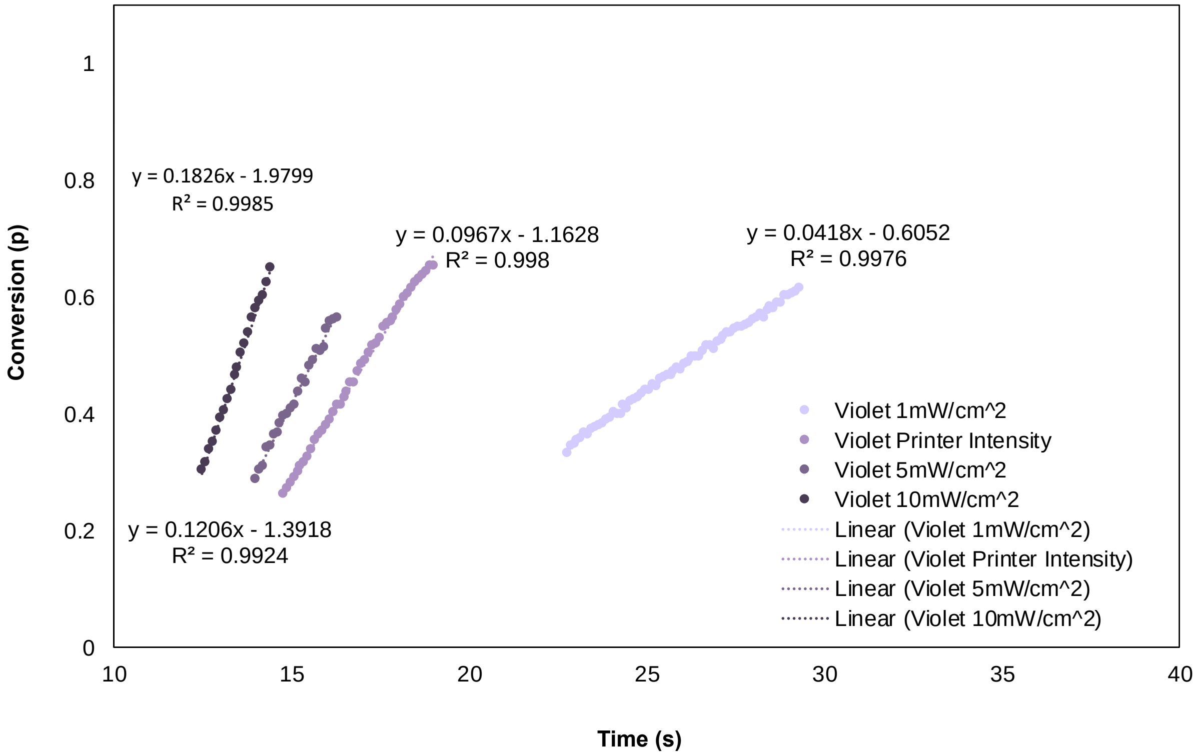

Figure S27. RT-FTIR rates of violet resin at various light intensities

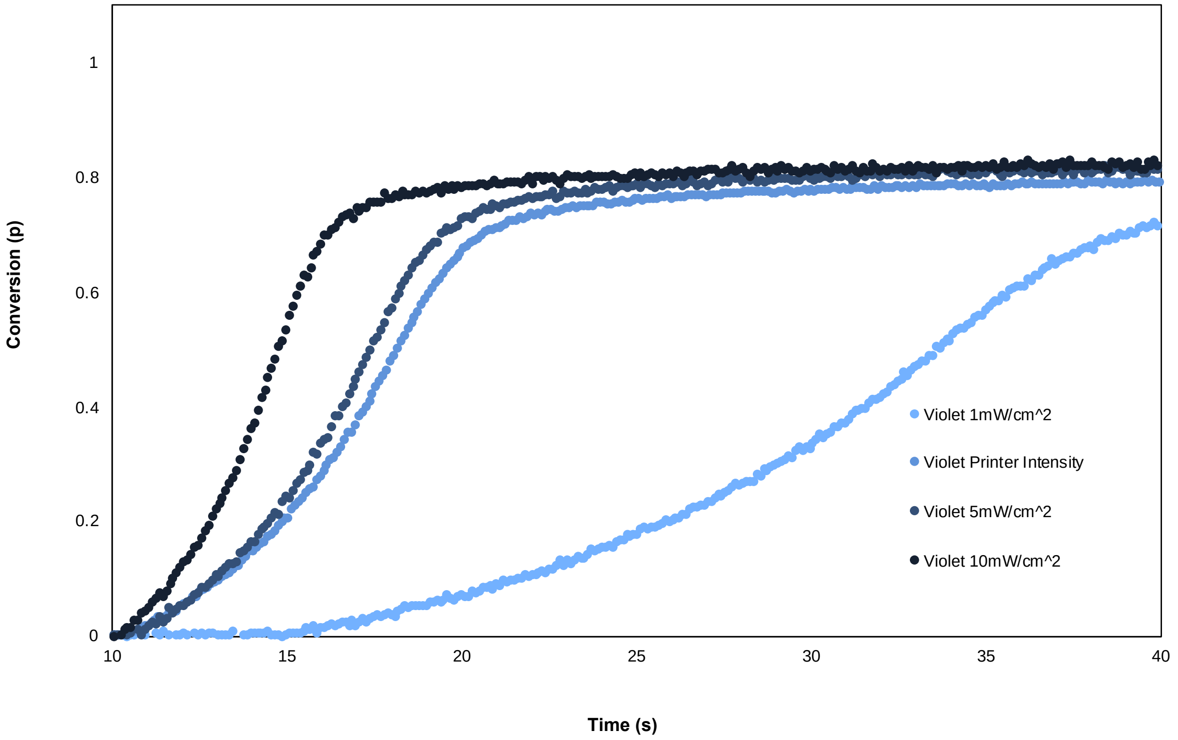

Figure S28. RT-FTIR study of blue resin at various light intensities

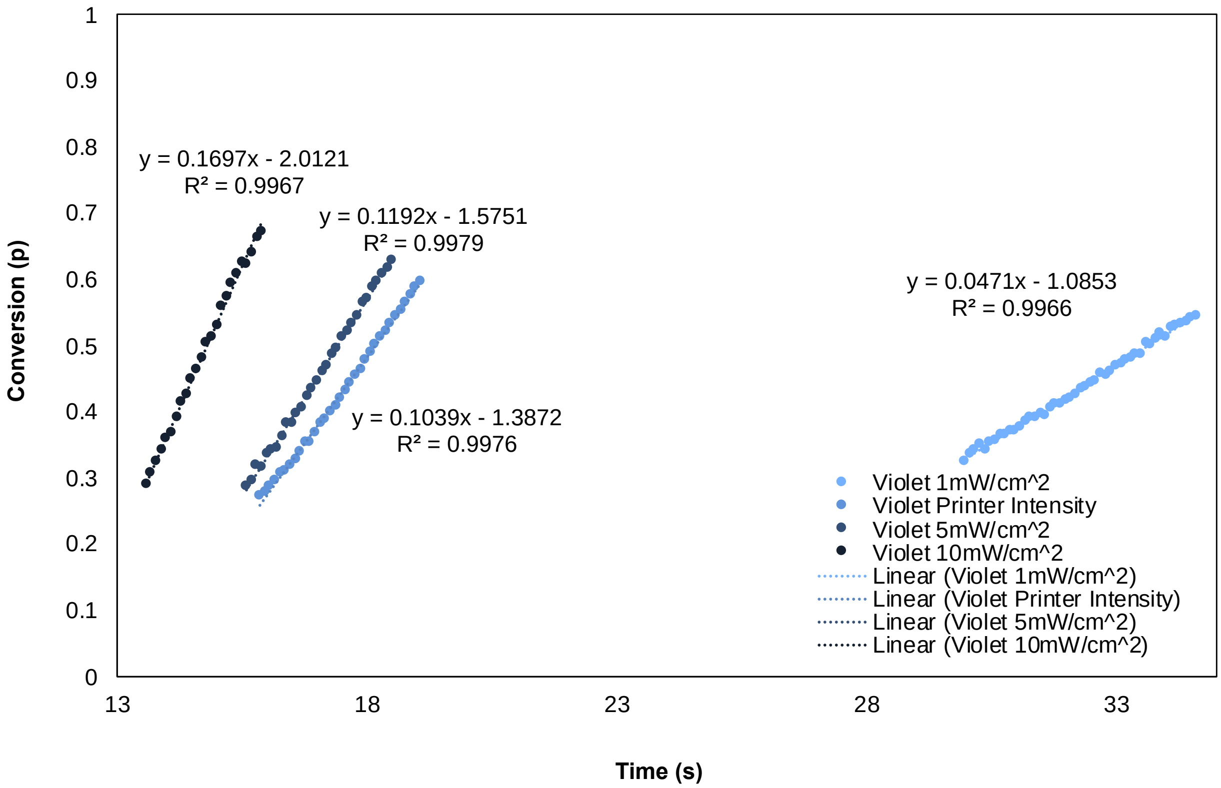

Figure S29. RT-FTIR rates of blue resin at various light intensities

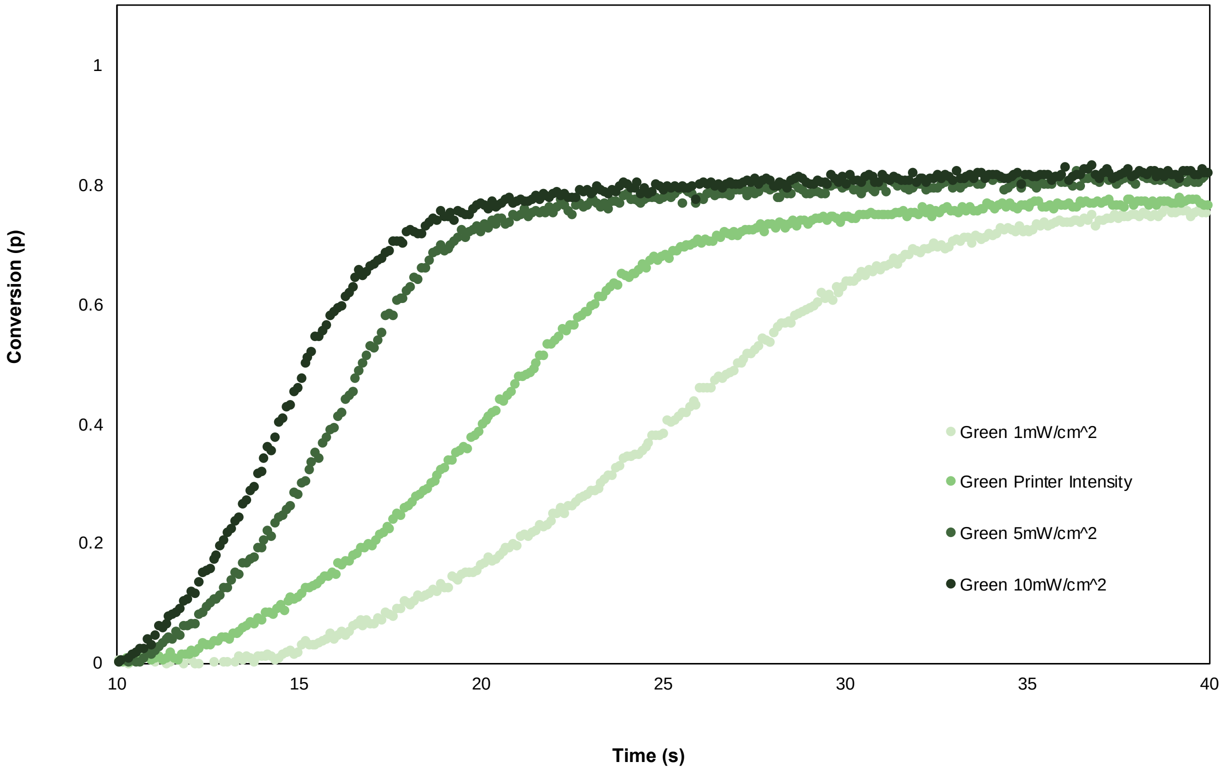

Figure S30. RT-FTIR study of green resin at various light intensities

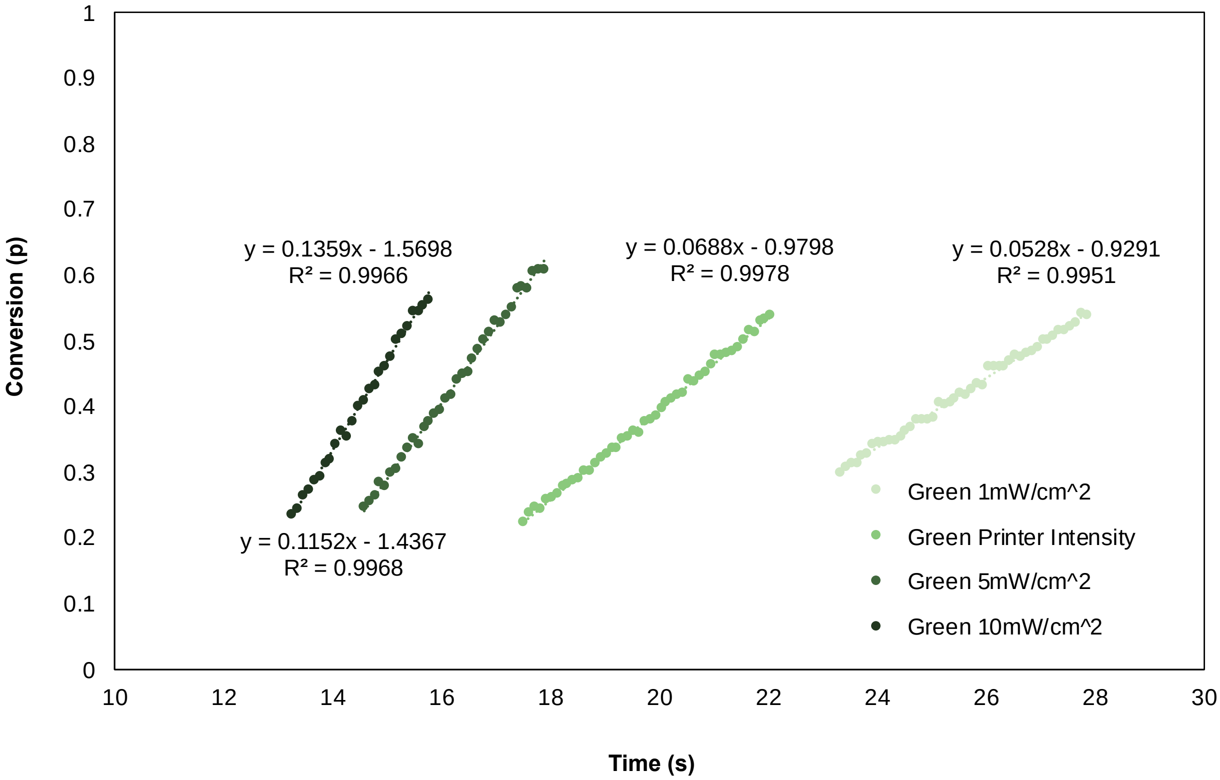

Figure S31. RT-FTIR rates of green resin at various light intensities

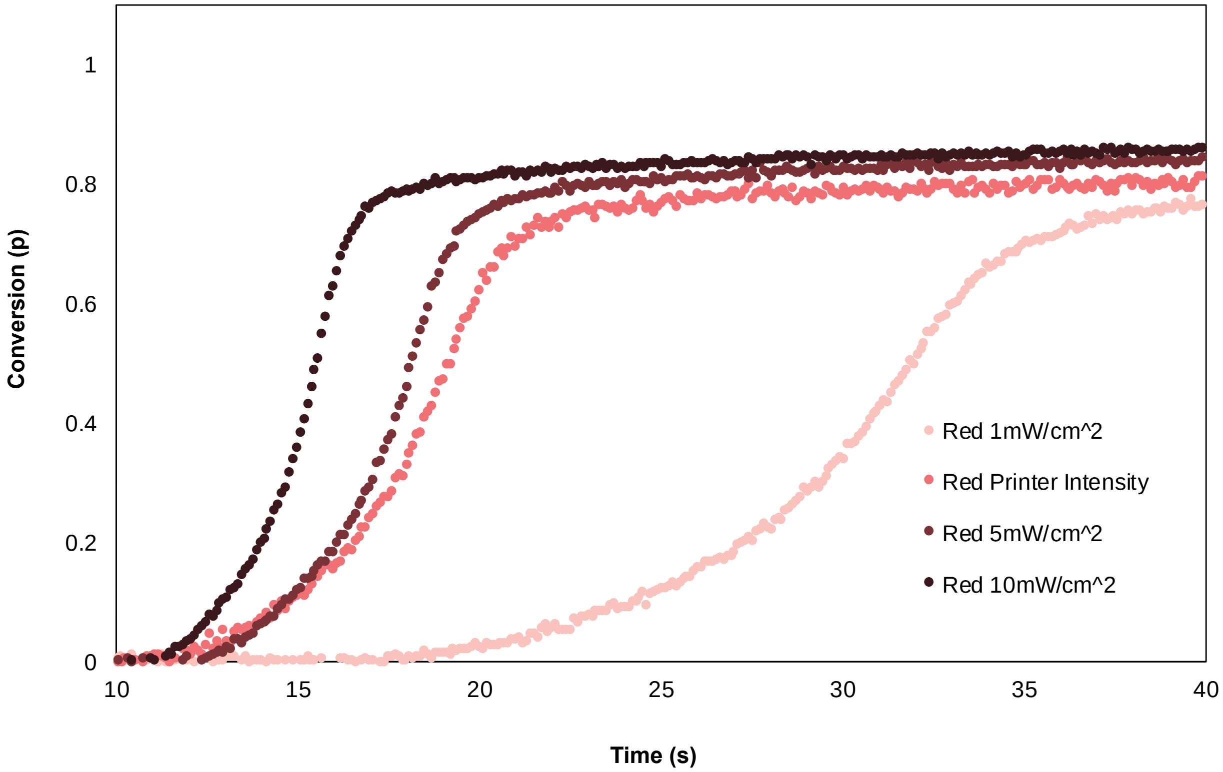

Figure S32. RT-FTIR study of red resin at various light intensities

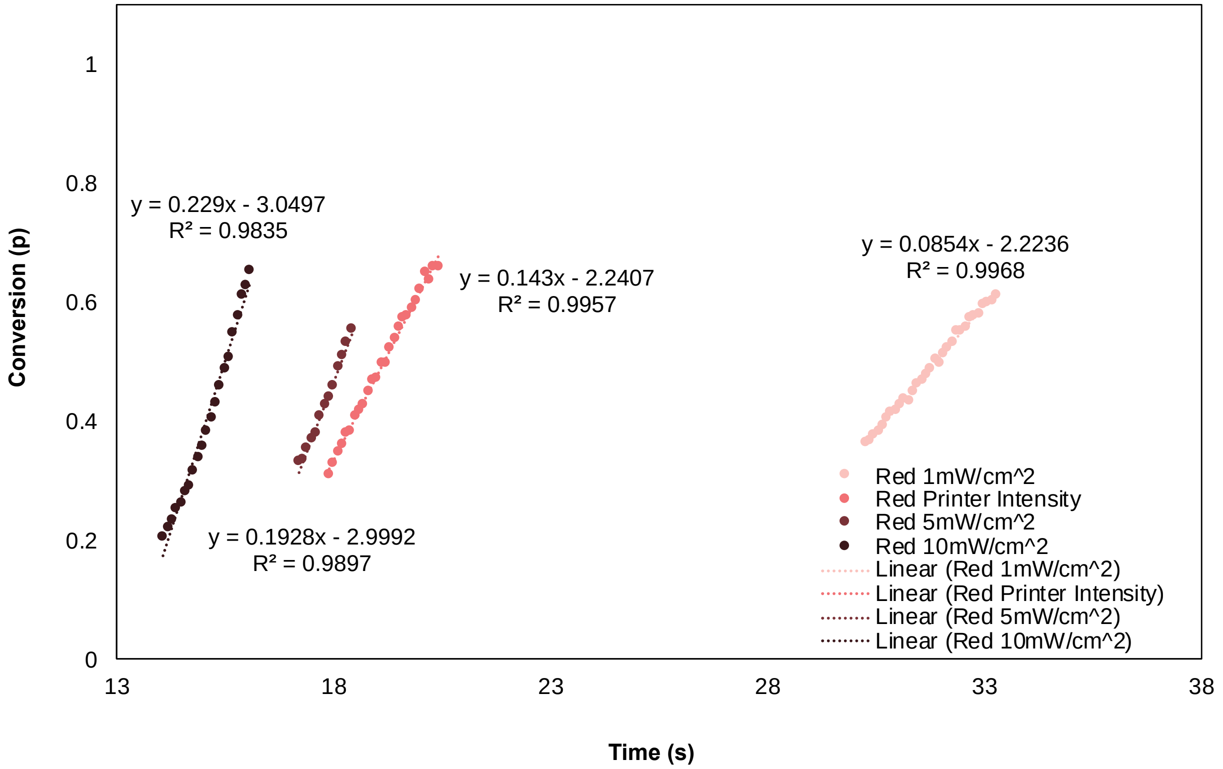

Figure S33. RT-FTIR rates of red resin at various light intensities

Photorheology

Photorheology experiments were completed using a Discovery Hybrid Rheometer manufactured by TA Instruments (TA Instruments, DE, USA). The rheometer was equipped with a "UV Light Guide" accessory, a disposable 20 mm diameter acrylic bottom plate, and a 20mm diameter geometry upper aluminum parallel plate. A liquid light guide was used to illuminate the samples with the corresponding visible light using a 405, 460, 530, or 617 nm LED connected to a driver from which light intensity could be controlled remotely through software. Each sample was tested in triplicate at the printer light intensity (3.3 mW/cm^2 for 405 nm, 3.4 mW/cm^2 for 460 nm, 1.8 mW/cm^2 for 530 nm, and 2.1 mW/cm^2 for 617 nm). The rheometer was set to run for two data acquisition cycles with the following experimental parameters: 1. Conditioning (Axial Force = 0 N), 2. Dynamic Time Sweep at 1% strain (60 s), 3. Fast Oscillation Step at 1% strain (50 s), 4. Dynamic Time Sweep at 1% strain (60 s). The gap height was set to 100 µm for each experiment. The resin samples were degassed with argon prior to each experiment and argon was passed over each sample during the duration of the experiment to best match 3D printing conditions. The light was not turned on until 10 s into the fast oscillation step. Storage modulus (G') and loss modulus (G") were monitored in real time and the light was turned off following inflection of the data, as noted by eye. To determine the gel point (where storage and loss modulus cross), first G' was normalized by taking the average from the first dynamic time sweep and subtracting this number from the G' values recorded in the fast oscillation step. Next, the fast oscillation step G' and G" were plotted as a function of time and the observed time point at which the moduli crossed or changed in concavity was taken to be the point of gelation from when the light was turned.

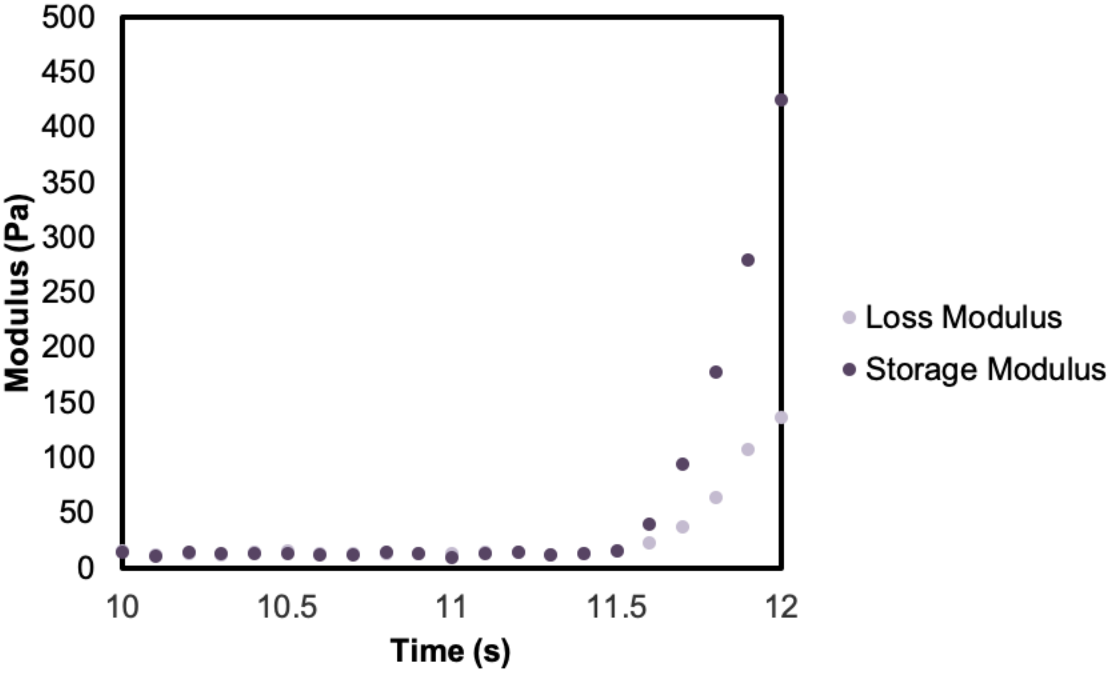

Figure S34. Photorheology study of violet resin with optimized opaquing agent at printer light intensity

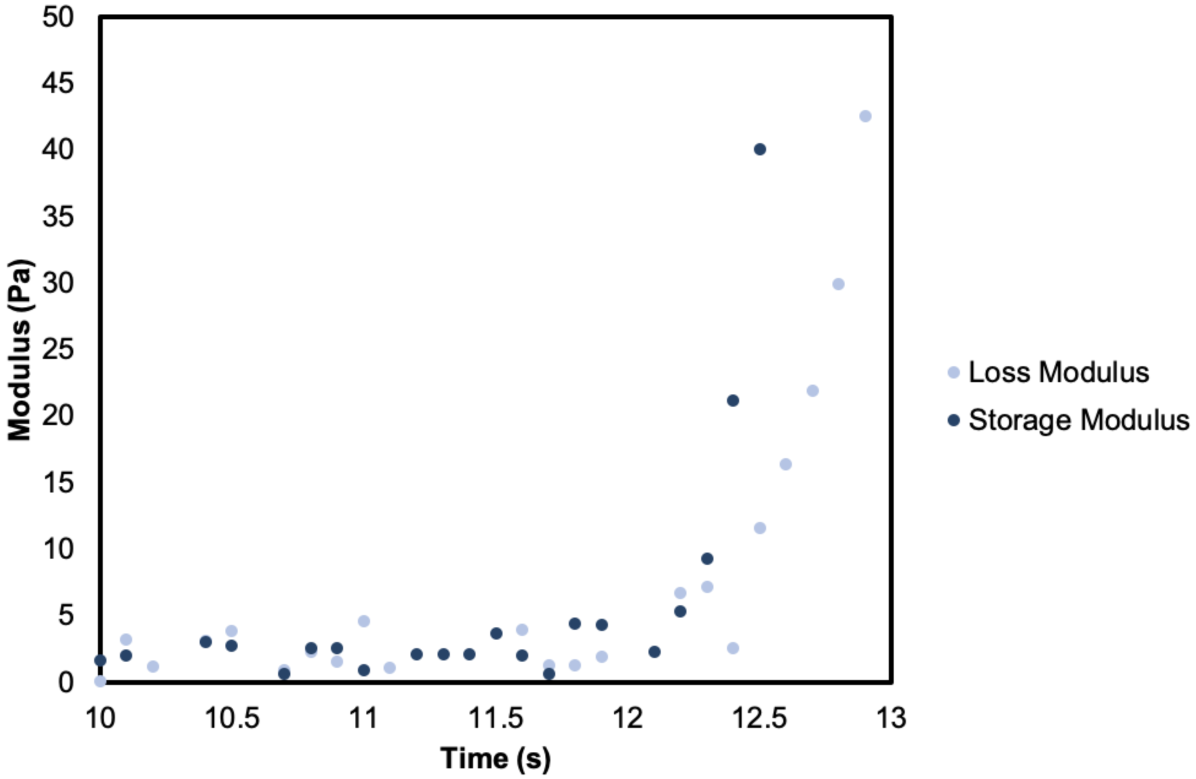

Figure S35. Photorheology study of blue resin (H-Nu 470) at printer light intensity

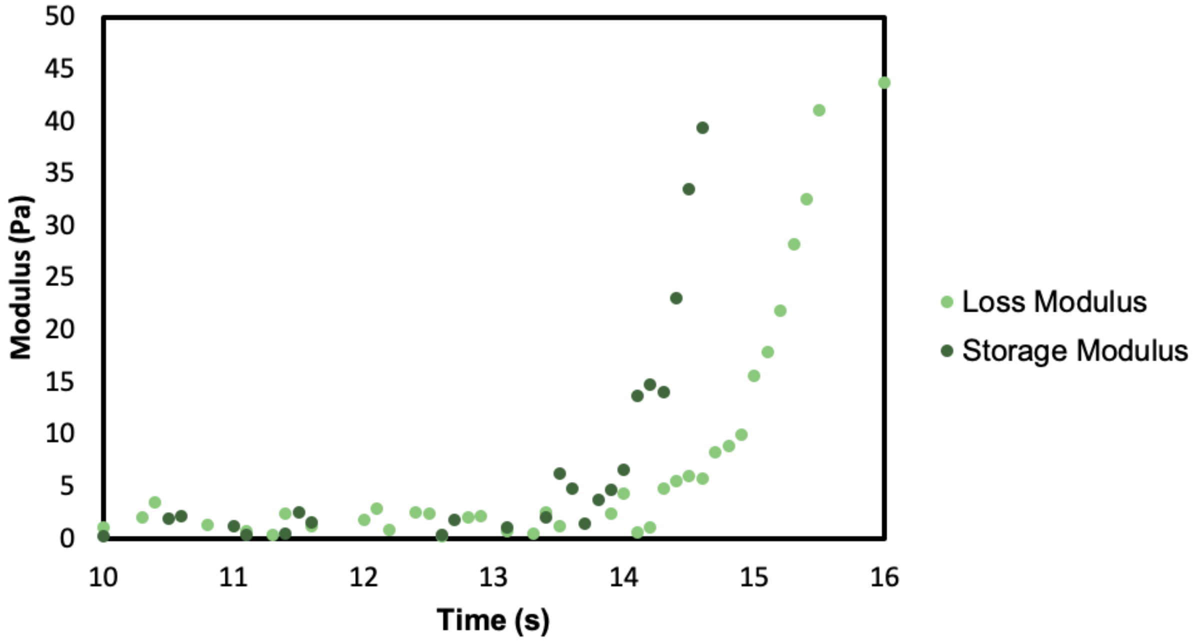

Figure S36. Photorheology study of green resin with optimized opaquing agent at printer light intensity

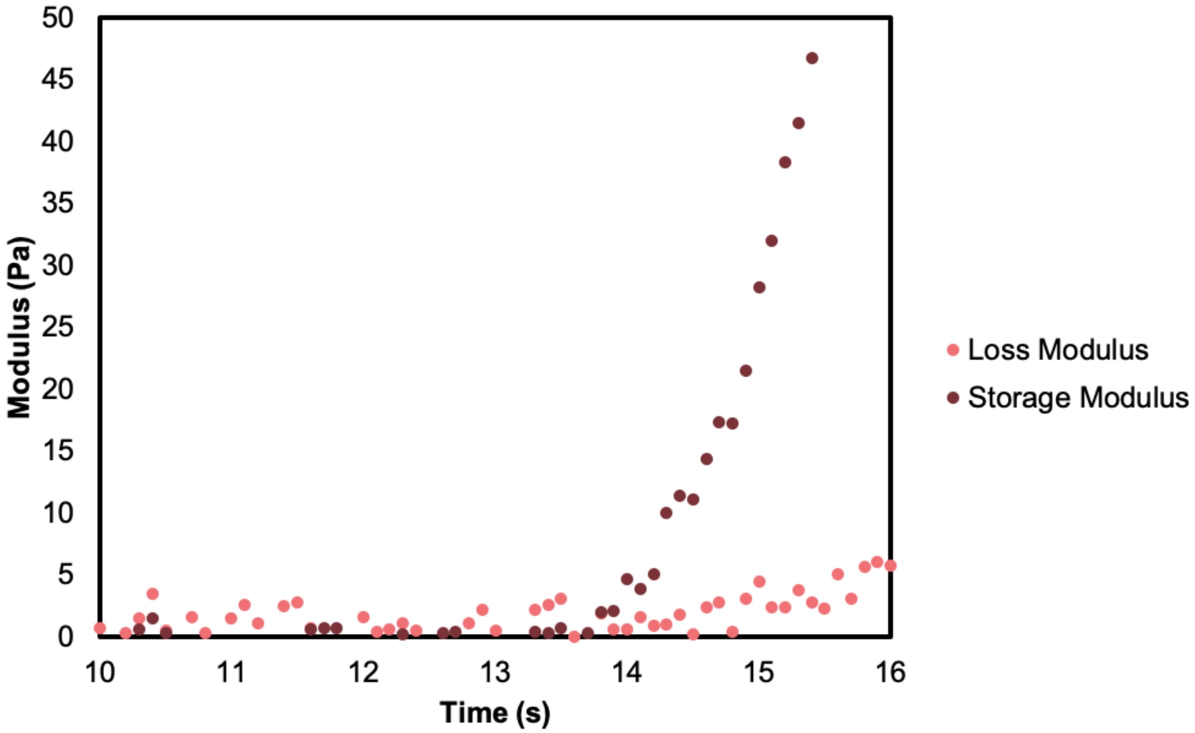

Figure S37. Photorheology study of red resin with optimized opaquing agent at printer light intensity

Table S8. Gel points measured using photorheology and corresponding percent double bond conversion at the gel point determined using the FTIR data

	Gel Point (s)	*Conversion at Gel Point (%)*
Violet	1.8 ± 0.2	4.5
Blue	1.9 ± 0.1	5.0
Green	3.4 ± 0.2	5.5
Red	4.2 ± 0.2	8.0

Tensile testing

3D printed dogbones were post-cured with UV light for 20 min. (unless otherwise noted). Uniaxial tension was applied to each sample under ambient conditions using a tensile tester (AGS-500NXD, SHIMADZU) equipped with a load cell (500 N load cell capacity) at a crosshead speed of 0.05 mm/sec. ASTM standards were used for the 3D printed dogbones, with dimensions of 1.11 mm (thickness), 1.76 mm (gauge width), and 22.8 mm (gauge length). Experiments were repeated more than 5 times for each sample and all of displayed results represent an average of all runs.

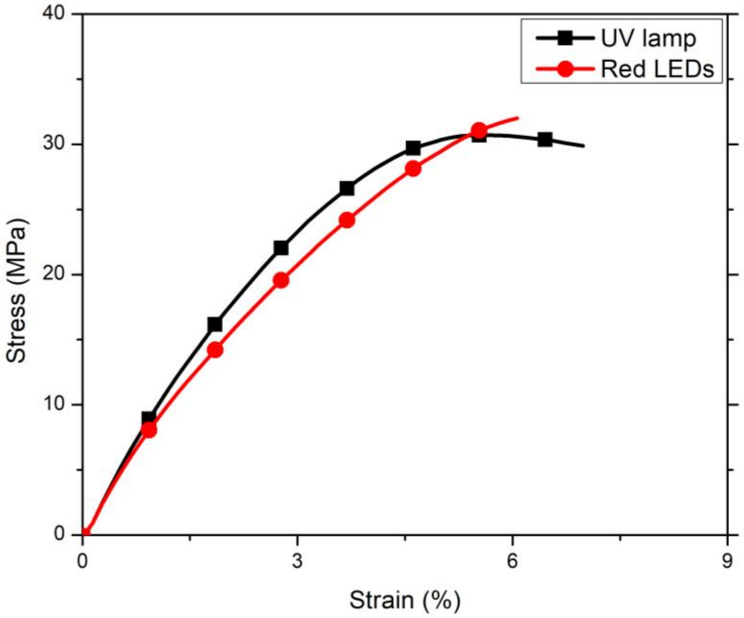

Figure S38. Mechanical testing of 3D printed dogbones comprising cured red resin, post-cured with (a) UV light and (b) red light for 20 min.

Table S9. Mechanical properties of 3D printed dogbones from violet, blue, green, and red resins.

	Violet	Blue	Green	Red
σ_y (MPa)	28.3 ± 0.8	29.7 ± 1.2	30.5 ± 1.4	30.7 ± 1.8
ε_f (%)	8.2 ± 0.7	6.8 ± 0.6	8.3 ± 1.8	7.0 ± 0.3
E (MPa)	997.1 ± 61.9	1022.1 ± 62.8	985.6 ± 102.2	1043.2 ± 94.0

Table S10. Mechanical properties of dogbones from optimized red resin, printed at three different edge-on angles.

Red Stiff Resin	Horizontal	Diagonal	Vertical
σ_y (MPa)	30.7 ± 1.8	30.6 ± 1.6	28.8 ± 1.6
ε_f (%)	7.0 ± 0.3	6.5 ± 0.8	10.8 ± 1.3
E (MPa)	1043.2 ± 94.0	1148.0 ± 69.5	1057.2 ± 98.8

Versatility. To examine the monomer scope of the present photosystems, 3D horizontal dogbones and their mechanical properties were examined for resins comprising 100% TEGDA crosslinker. Prints were performed with 100 µm slice thickness and exposure times of 15 s for the first layer and 12 s for all subsequent layers.

Table S11. Formulation for red-light sensitive TEGDA resin

PI/PS (wt%)[a]	Donor (wt%)[a]	Acceptor (wt%)[a]	Resin (wt%)
ZnTPP (0.3)	Borate V (0.2)	H-Nu 254 (2)	TEGDA (100)

[a]Percent by weight of total resins

Table S12. Mechanical properties of 3D printed dogbones from red-light sensitive TEGDA resin

	TEGDA resin
$\boldsymbol{\sigma_y}$ (MPa)	15.9 ± 0.6
$\boldsymbol{\varepsilon_f}$ (%)	5.6 ± 0.7
E (MPa)	468.3 ± 16.8

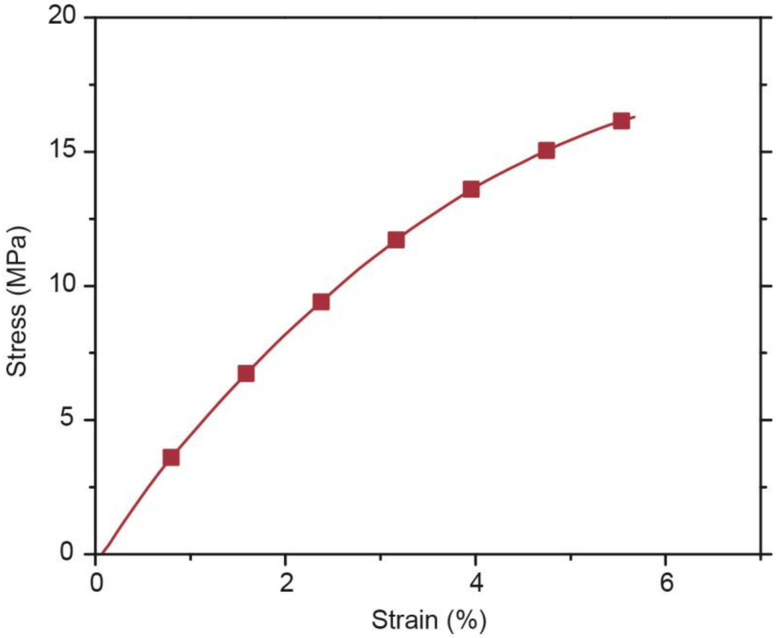

Figure S39. Mechanical testing of 3D printed dogbones from red-light sensitive TEGDA resin

Water swelling tests

Stiff and soft red resins (see **Table S1** for details) were used to print cube arrays. 6 cubes were printed at once and the dimension of each cube was 5 mm × 5 mm × 5 mm. Slice thickness of 3D printed cube was 100 µm. An exposure time of 15 s for the base layer and 11 s for all subsequent layers was used. Acrylic housing was purged with argon gas over the course of printing. Samples were post-cured with UV light for 20 min.

Each individual hard or soft cube was first weighed (dry weight) and then added to an individual scintillation vial filled with 20 mL of deionized water. The vials were sealed and left to sit on the benchtop for 72 hours undisturbed. At the end of the 72 hours, each cube was removed from its respective vial, gently dried with a clean paper towel until it was no longer wet to the touch, and finally weighed (swelled weight).

Table S13. Swelling ratio of two disparate, 3D printed objects

	Soft				**Hard**			
Sample	*Soft (Dry) (g)*	*Soft (Swelled) (g)*	*Water Uptake (g)*	*Increase (%)*	*Hard (dry) (g)*	*Hard (Swelled) (g)*	*Water Uptake (g)*	*Increase (%)*
1	0.1676	0.466	0.2984	178.04	0.1384	0.2155	0.0771	55.71
2	0.1684	0.468	0.2996	177.91	0.1376	0.2107	0.0731	53.13
3	0.1663	0.4606	0.2943	176.97	0.1376	0.2115	0.0739	53.71
4	0.1719	0.4768	0.3049	177.37	0.1383	0.2068	0.0685	49.53
5	0.1719	0.4774	0.3055	177.72	0.1418	0.2203	0.0785	55.36
6	0.1667	0.4614	0.2947	176.78	0.141	0.2181	0.0771	54.68
avg	**0.1688**	**0.4684**	**0.2996**	**177.47**	**0.1391**	**0.2138**	**0.0747**	**53.70**

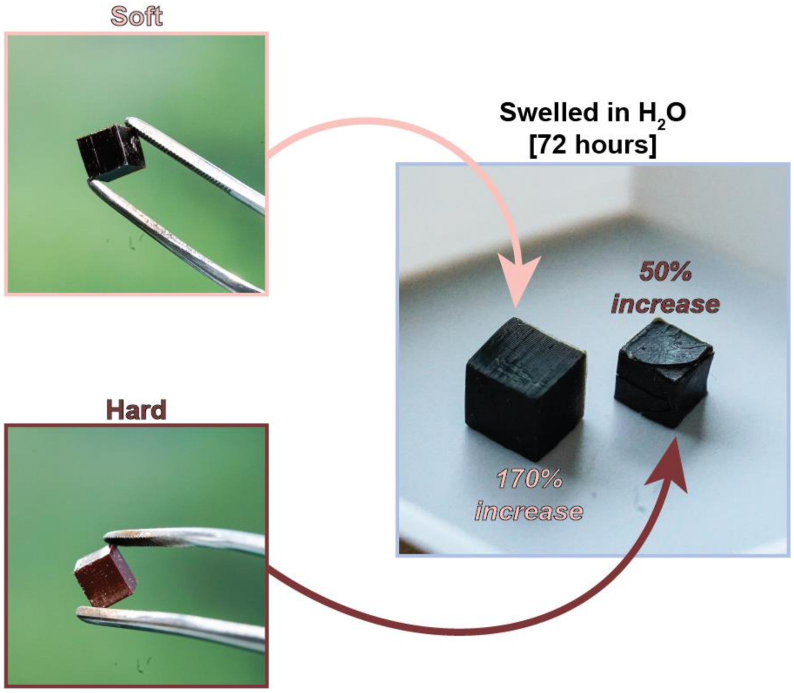

Figure S40. Swelling of two disparate, 3D printed objects.

3D printing

High resolution complex structures (i.e., octet truss lattice) were printed using the stiff red resin. Slice thickness of 25 µm and 100 µm was used. For the 25 µm layer thickness, an exposure time of 12 s for the first layer and 8 s for all subsequent layers was used. For the 100 µm layer thickness, an exposure time of 15 s for the first layer and 11 s for all subsequent layers. Acrylic housing was purged with argon gas over the course of printing.

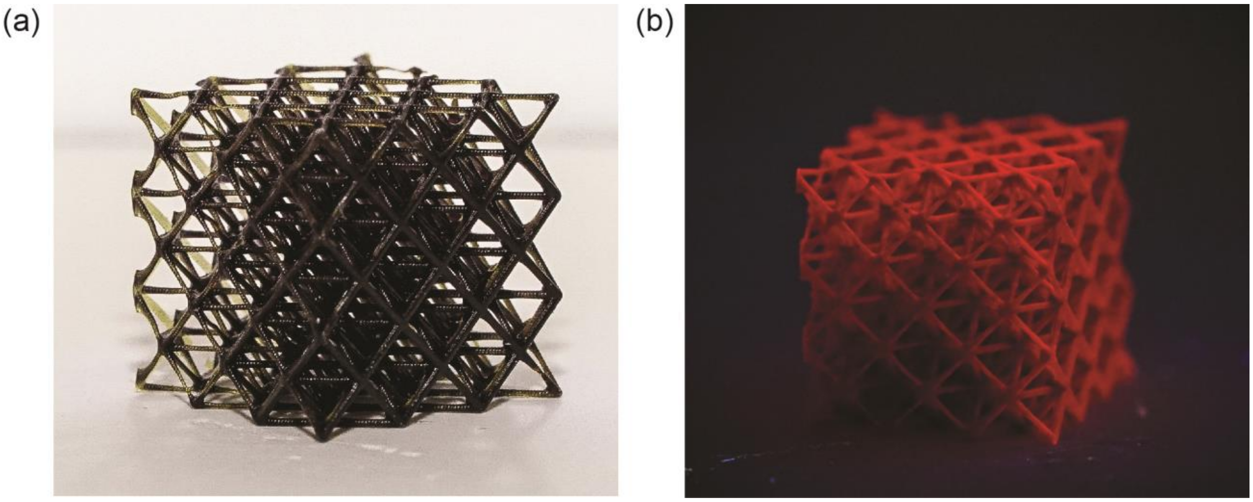

Figure S41. Optical images of 3D printed octet truss lattice using 100 µm layer thickness. Photographs under (a) room light and (b) handheld UV light centered at 365 nm.

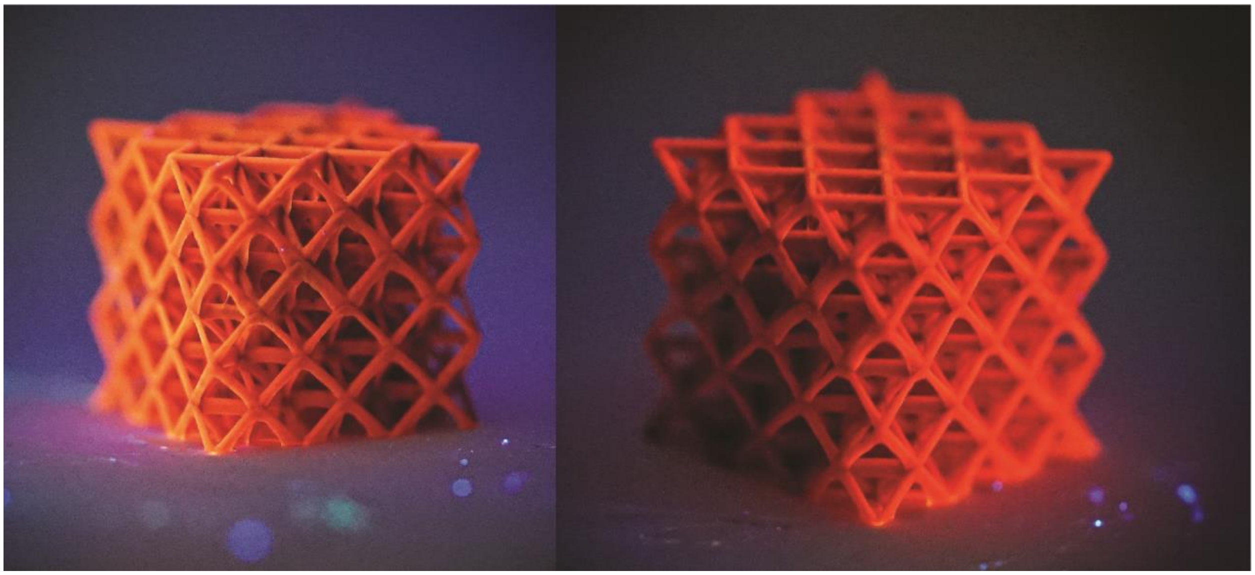

Figure S42. Optical images of 3D printed octet truss lattice using 25 µm layer thickness under handheld UV light centered at 365 nm.

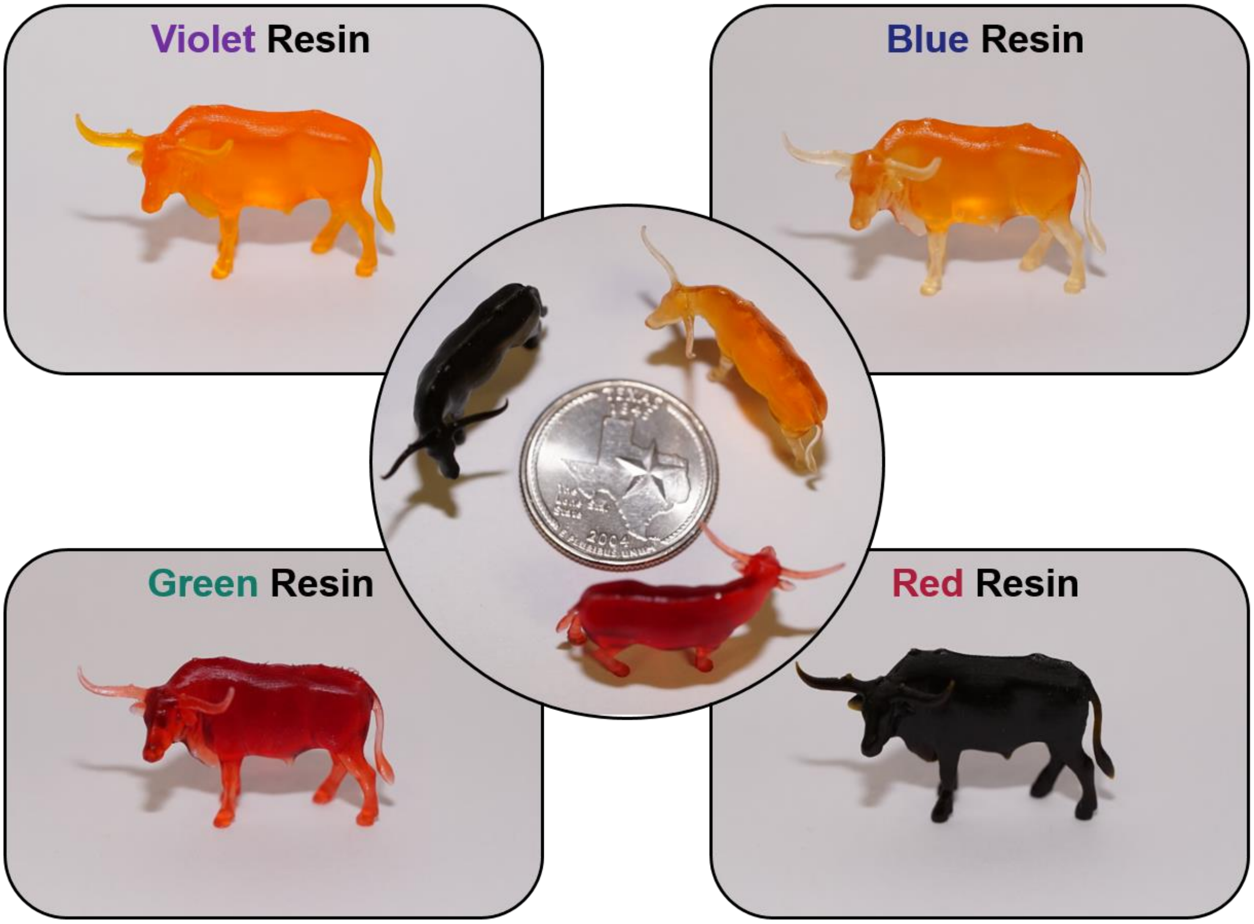

Figure S43. Optical images of 3D printed longhorns with corresponding resin indicated. A quarter is placed in the middle image for reference.

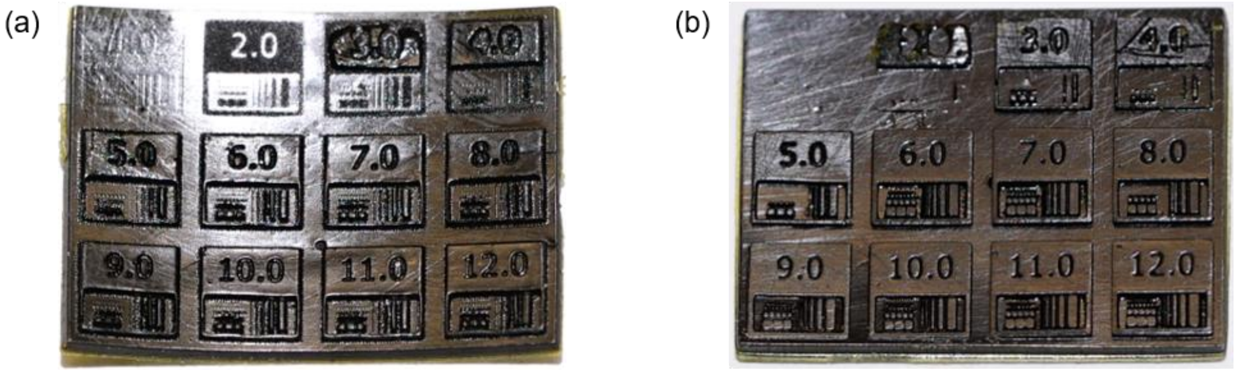

Figure S44. Optical images of resolution prints for (a) soft red resin and (b) pure TEGDA red resin.

Scanning electron microscope (SEM)

SEM (Fei Quanta 650, ThermoFisher) was used to examine the surface characteristics of the 3D printed octet truss and measure the average layer thickness. For improved imaging, the sample was sputtered with Au using an EMS sputter coater (Electron Microscopy Science). Sputtering was conducted for 1.5 min at 40 mA.

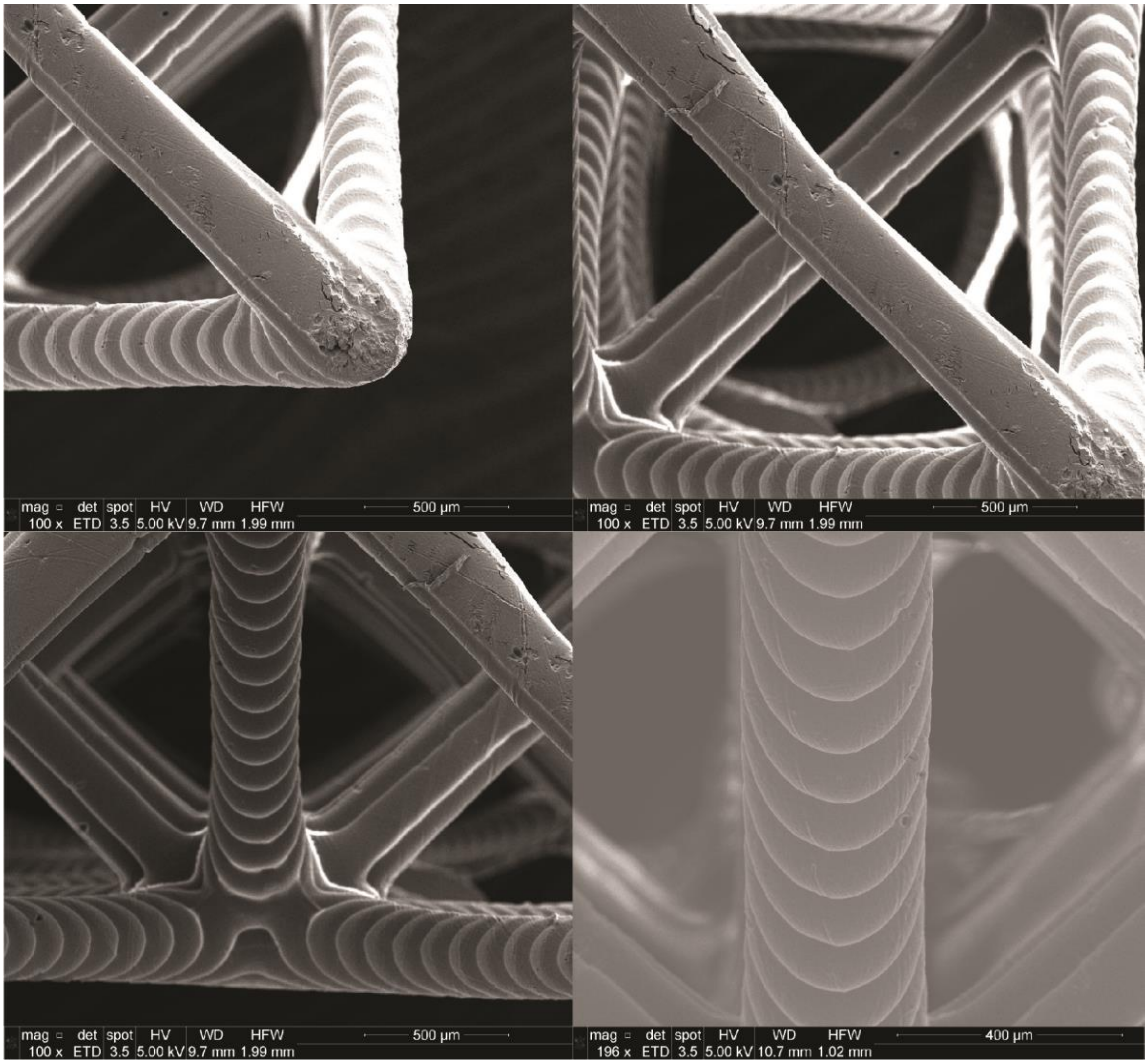

Figure S45. SEM images at different magnifications of a 3D printed octet truss lattice having a 100 µm layer thickness.